Astronomy Reports, Vol. 48, No. 3, 2004, pp. 171–184. Translated from Astronomicheskiĭ Zhurnal, Vol. 81, No. 3, 2004, pp. 195–208.

H_2O Maser Emission in the Direction of Sagittarius B2: Results of Monitoring for 1982–1992

E. E. Lekht[1], O. Ramirez Hernandes[2], A. M. Tolmachev[3], and I. I. Berulis[4]

[1] *Instituto Nacional de Astrofísica, Óptica y Electrónica, Luis Enrique Erro No. 1, Apdo Postal 51 y 216, 72840 Tonantzintla, Puebla, México*

[2] *Sternberg Astronomical Institute, Universitetskiĭ pr. 13, Moscow, 119992 Russia*

[3] *Pushchino Radio Astronomy Observatory, Astro Space Center, Lebedev Physical Institute, Russian Academy of Sciences, Pushchino, Moscow oblast, 142290 Russia*

[4] *Technological University, Kaunas, Lithuania*

Received June 15, 2003; in final form, September 18, 2003

Abstract—The results of monitoring the water-vapor maser at $\lambda = 1.35$ cm in Sgr B2 are presented. The observations were carried out on the 22-m radio telescope of the Pushchino Radio Astronomy Observatory (Russia) in 1982–1992. A strong flare of the maser radiation associated with Sgr B2(N) was detected in this period. The absolute strength of this flare is comparable to the megamaser emission observed in Orion in 1979–1987. The flare is probably due to a strengthening of the flow of material from the rotating accretion disk, in which are embedded the three ultracompact HII regions K1, K2, and K3. A subsequent excitation of emission features at increasingly higher radial velocities was observed, associated with a gradient of V_{LSR} along the direction of the outflow. The large width of the lines (>0.86 km/s) could reflect a complex structure for the maser spots, such as a chain or filamentary structure, as has been observed in Orion and S140. © *2004 MAIK "Nauka/Interperiodica".*

1. INTRODUCTION

Sagittarius B2 is a complex located about 200 pc from the Galactic center. This region is associated primarily with a giant molecular cloud with a mass of $\sim 3 \times 10^6 M_\odot$ and a diameter of 45 pc [1]. The cloud is made up of an envelope and a core ~6 pc in size with a density of $\sim 10^5$ cm^{-3} [2].

Sgr B2 is one of the most active regions in which massive stars are forming in our Galaxy, as is demonstrated by the presence of the main signs of star formation: very dense molecular material [3], a bipolar molecular outflow from the dense core of the cloud [4], complex molecules and supercompact HII regions [5], a hot core [6], and H_2O, OH, H_2CO, CH_3OH, and SiO maser emission, which is known to accompany the formation of protostellar structures.

The radio continuum observations of Benson and Johnston [7] showed that there are at least 12 individual HII regions in the cloud core located in three main clumps, in the northern part of the complex Sgr B2(N), the main part Sgr B2(M), and the southern part Sgr B2(S), with the distance between Sgr B2(N) and Sgr B2(M) being ~45″. Subsequently, it was shown that the structures of each of these clumps are rather complex. Detailed images of 49 continuum components in this region were obtained at 1.3 cm [5], for 29 of which emission in the H66α line was detected [8].

The H_2O maser emission in Sgr B2 originates in compact ($\sim 10^{13}$ cm) and dense ($n(H_2) \sim 10^9$–10^{11} cm^{-3}) clumps of gas [9, 10] that are concentrated in four separate regions. Three of these regions are associated with Sgr B(N), Sgr B(M), and Sgr B(S), while the fourth is located between Sgr B(N) and Sgr B(M). In all, they contain at least 39 maser spots [11].

The 22.2 GHz H_2O line can be used to investigate manifestations of protostellar activity that are hidden from us by dense gas–dust envelopes. The H_2O maser emission is a sensitive indicator of the phenomena occurring in active regions. Long-term monitoring provides information about the time variations of the maser emission both as a whole and for individual spectral components.

We present here an analysis of spectra taken in this line obtained during monitoring of the H_2O maser in Sgr B2 in 1982–1992. Results of a second monitoring interval (1993–2003) and results for individual emission features will be presented in subsequent papers.

1063-7729/04/4803-0171$26.00

2. OBSERVATIONS AND ANALYSIS

We have monitored the H_2O maser in Sgr B2 ($\alpha_{1950} = 17^h44^m10^s$, $\delta_{1950} = -28°22'00''$) from 1982 to the present using the 22-m radio telescope of the Pushchino Radio Astronomy Observatory. Due to the large volume of data obtained, we consider here only the results for the observations acquired in 1982–1992. The mean interval between observations is 1.2 months.

A 22-GHz traveling-wave maser amplifier cooled by liquid helium was used for the 1982–1992 observations. Symmetrical beam modulation was employed to weaken the influence of atmospheric emission; the source was first observed with the left, then with the right horn. A noise generator for calibration purposes was turned on during the first phase. The system noise temperatures for observations within a narrow range of angles were 250–300 K. The antenna beam width at 1.35-cm is 2.6′. For a point source of unpolarized radiation, an antenna temperature of 1 K corresponds to a flux density of 25 Jy.

Analysis of the received signals was carried out using a 96-channel filter spectral analyzer with a resolution of 7.5 kHz (0.101 km/s in radial velocity for a 1.35-cm line). The necessary frequency stability of the first heterodyne was provided by a high-stability Ch6–31 frequency synthesizer and a phase self-tuning frequency system. The tuning of the receiver to the corresponding spectral range was done by varying the frequency of the first heterodyne.

Because the elevation of Sgr B2 above the horizon was only 6°–7°, corrections for absorption in the Earth's atmosphere were substantial. The difference in the amount of absorption in summer and winter (including the effects of temperature, humidity, and pressure) reached a factor of two to three. Some of the summer spectra have high noise levels even after correction.

The H_2O spectra of Sgr B2 corrected for absorption in the Earth's atmosphere are presented in Fig. 1. The radial velocity relative to the local standard of rest (LSR) in km/s is laid out along the horizontal axis, while the vertical axis plots the flux density in Jy. Because of the large variations of the signal level, the graphs are given using different scales. However, we have restricted the difference in the scales to a factor of two to avoid losing information about relatively weak emission. The vertical arrow shows the scale in Jy, and the horizontal lines show the zero levels for the spectra.

The analysis of the monitoring data showed the presence of strong variations of the structure of the spectra. We separated the data into intervals based on the variations for 1982–1992, for each of which we produced a superposition of spectra, shown in Fig. 2. The time intervals are indicated in the corresponding plots. For ease of comparison, all the plots, including the last (Fig. 2g), have been made using the same scale. The maximum flux for the strong flare during 1986–1987 at $V_{LSR} = 65.4$ km/s is indicated (3800 Jy).

As is noted above, the 22-m antenna received the total intensity of the H_2O emission of Sgr B2. Kobayashi *et al.* [11] reported the presence of four main groups of maser spots, three of which are identified with the sources Sgr B2(N), Sgr B2(M), and Sgr B2(S). The fourth group is located between Sgr B2(N) and Sgr B2(M). Our analysis showed that only two of these groups of maser spots can provide the most intense emission at radial velocities of 40–80 km/s. One of these is associated with Sgr B2(N), and the other, with Sgr B2(M). The observing epoch of Kobayashi *et al.* [11] (December 19, 1985) falls in the interval shown in Fig 2b. The arrows in this figure show the positions of the strongest emission features of the spectra for Sgr B2(N) and Sgr B2(M); all these features are present in our spectra for 1985. Figure 2g shows a synthesized spectrum for the 1986–1987 flare, constructed from individual components that our analysis indicate belong to Sgr B2(N). The spectra of these components were taken at the epochs of their maxima. The main parameters for this analysis are presented in the table.

The emission at 49 km/s with a maximum flux density of 800 Jy remained unidentified. We observed this emission from December 1984 through April 1985. It is probably associated with the group of maser spots in Sgr B2(N), since Kobayashi *et al.* [11] did not detect any emission at 44–51 km/s in the direction of Sgr B2(M).

Figure 3 presents plots of the variability of the fluxes and radial velocities of some emission features. The hollow triangles and squares show values taken from Kobayashi *et al.* [11] and the catalog of Comoretto *et al.* [12]. There was a sequence of flares in emission features at V_{LSR} values of 49, 56.2, 64.8, ≈66, and ≈66.4 km/s (see also Figs. 1a, 1b). In the last two cases, we have indicated approximate values for the velocities because there was a significant drift in the V_{LSR} of the emission by up to 1 km/s.

We constructed a schematic of the region of Sgr B2(N) based on the 1.3-cm radio continuum observations of star-forming regions of [5], the H66α hydrogen recombination-line data of [8], the water-vapor maser data of [11], and the data on the bipolar outflow of [13] (Fig. 4).

An important parameter for estimating the overall maser activity is the total flux, whose variations are shown in Fig. 5. The dotted smooth curve represents the slow variations of the total flux. The dashed

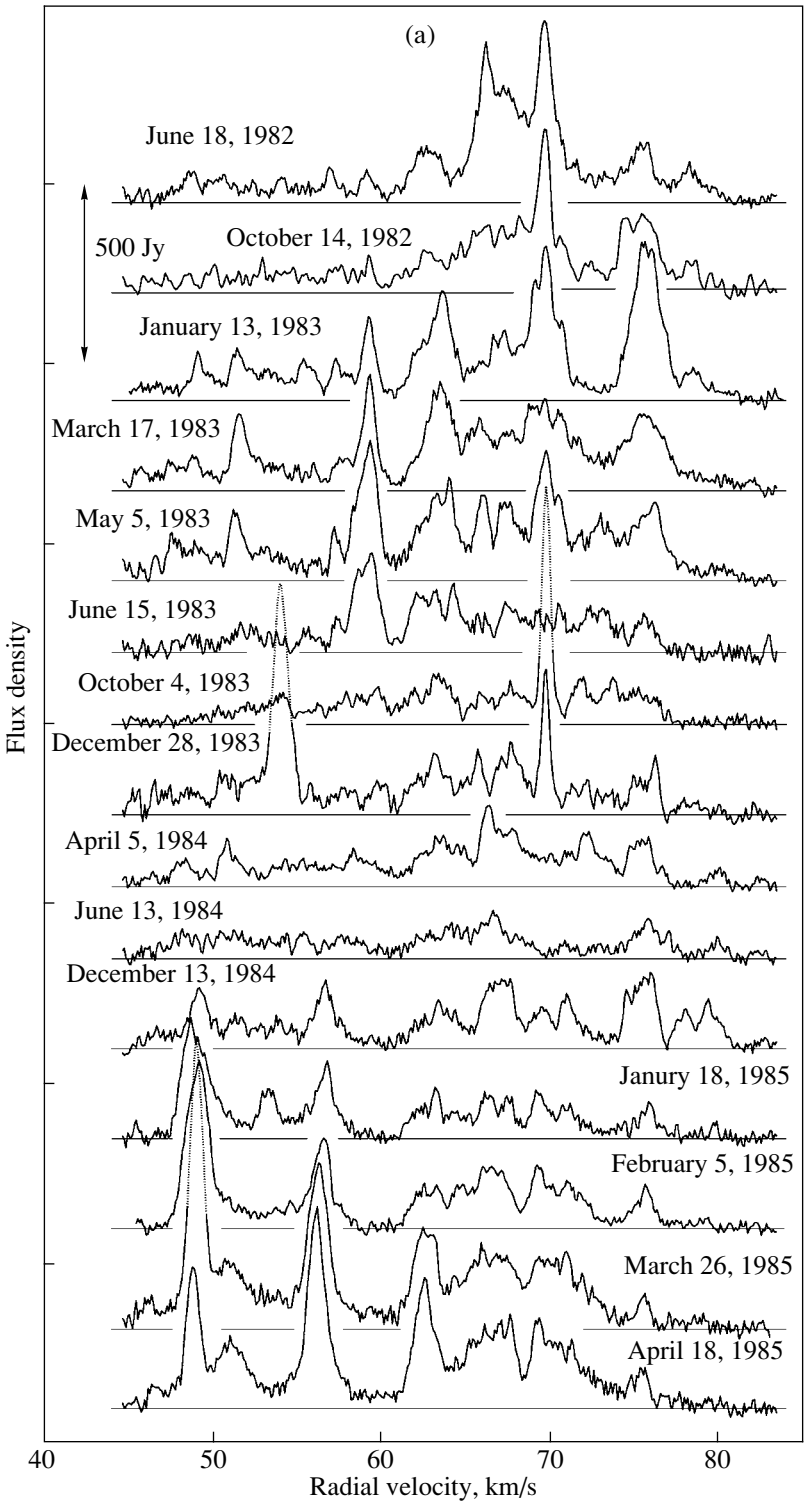

Fig. 1. Spectra of the H_2O maser source in Sgr B2 obtained in 1982–1992. The vertical arrows show the scale in Jy.

curve shows a representation of the slow variations for which there is a minimum influence from the strong flare of 1986–1987 and the subsequent decrease in emission. The arrows mark the most important flares and the deep minimum at the beginning of 1988. The variability of the velocity centroid is shown in Fig. 5b. The numbers correspond to the velocities of emission features that led to strong variations of the total flux (Fig. 5a) and velocity jumps (Fig. 5b). Since there

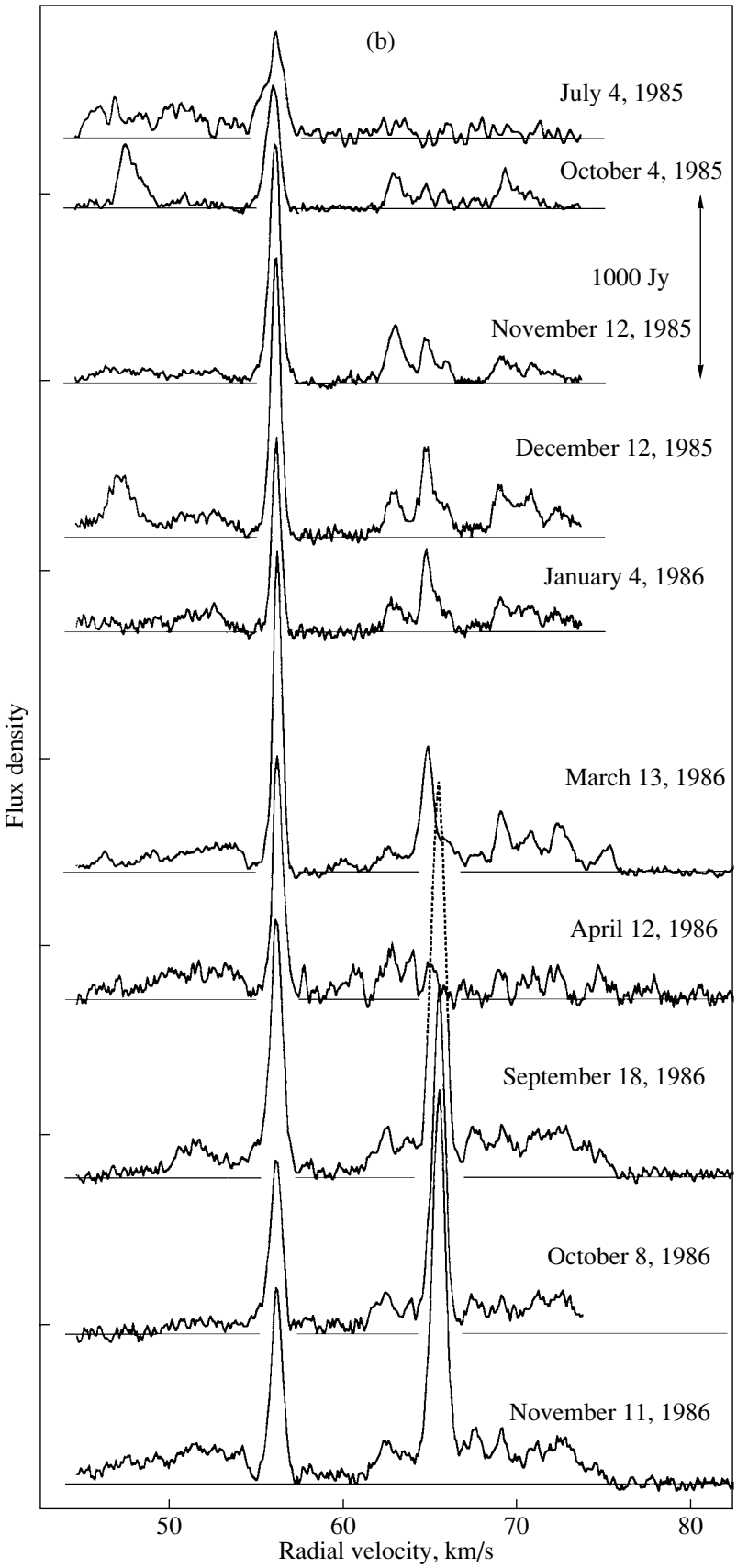
(b)
July 4, 1985
October 4, 1985
1000 Jy
November 12, 1985
December 12, 1985
January 4, 1986
March 13, 1986
April 12, 1986
September 18, 1986
October 8, 1986
November 11, 1986
Flux density
50
60
70
80
Radial velocity, km/s

Fig. 1. (Contd.)

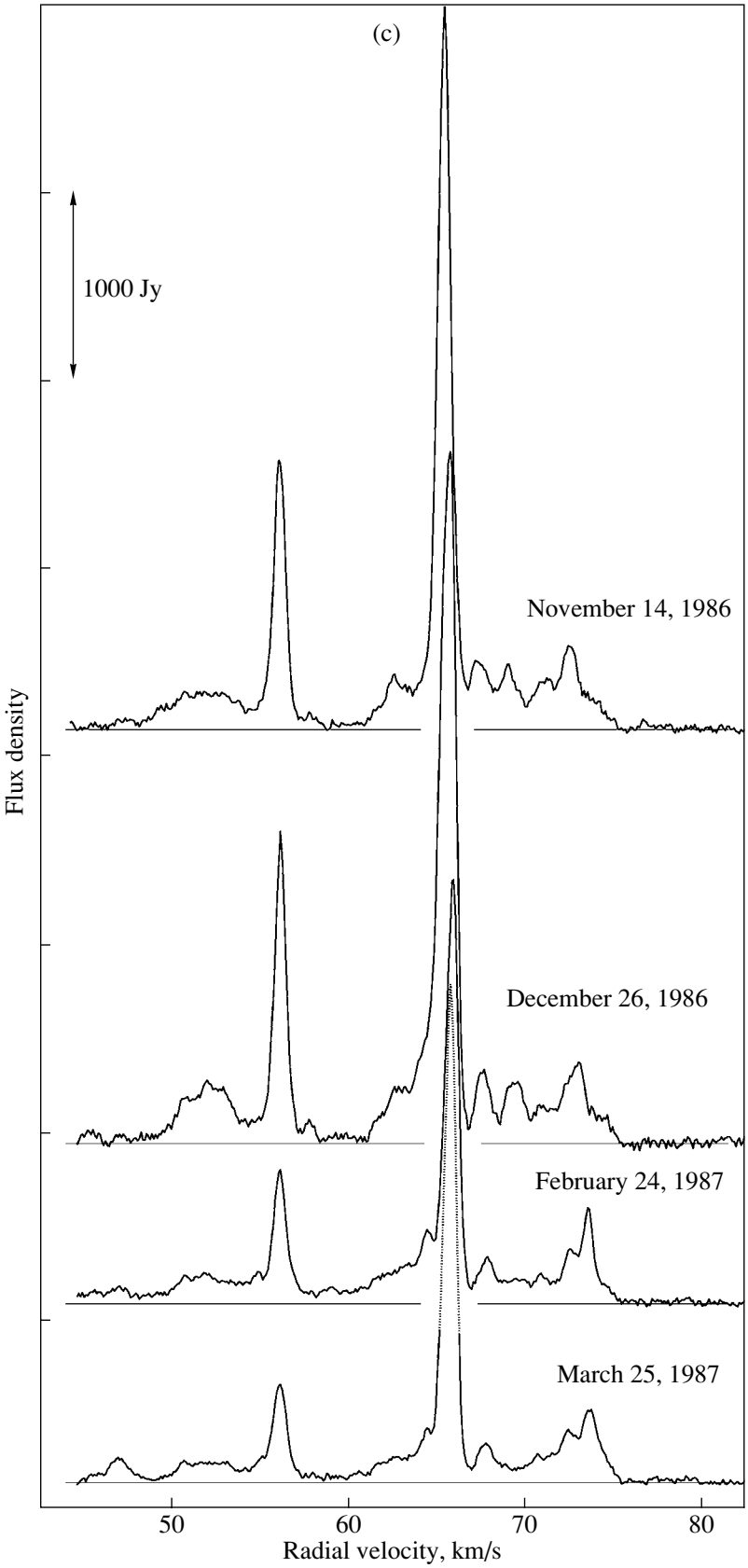
(c)
1000 Jy
November 14, 1986
December 26, 1986
February 24, 1987
March 25, 1987
Flux density
50
60
70
80
Radial velocity, km/s

Fig. 1. (Contd.)

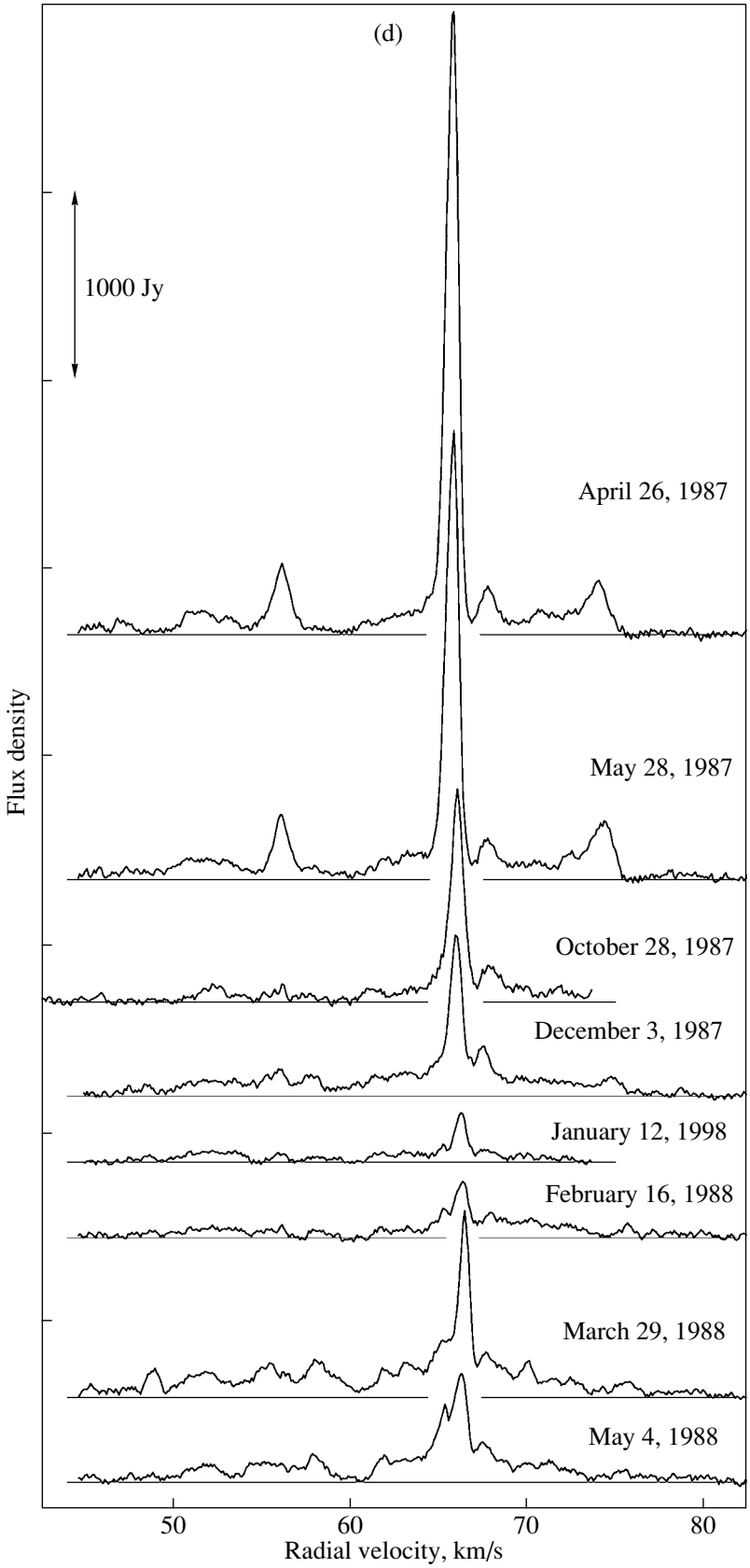
(d)
1000 Jy
April 26, 1987
May 28, 1987
October 28, 1987
December 3, 1987
January 12, 1998
February 16, 1988
March 29, 1988
May 4, 1988
Flux density
50
60
70
80
Radial velocity, km/s

Fig. 1. (Contd.)

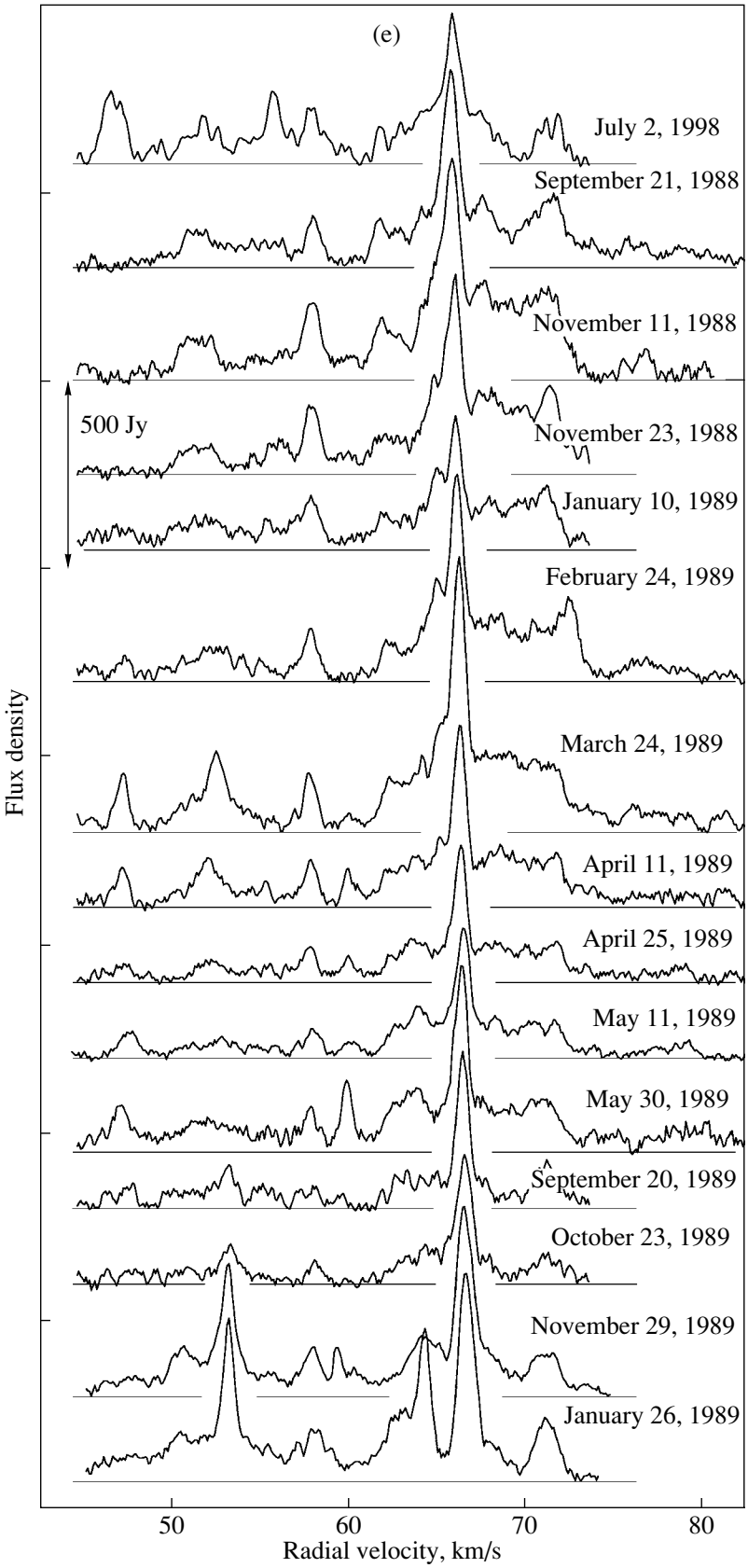
(e)
July 2, 1998
September 21, 1988
November 11, 1988
500 Jy
November 23, 1988
January 10, 1989
February 24, 1989
March 24, 1989
April 11, 1989
April 25, 1989
May 11, 1989
May 30, 1989
September 20, 1989
October 23, 1989
November 29, 1989
January 26, 1989
Flux density
50
60
70
80
Radial velocity, km/s

Fig. 1. (Contd.)

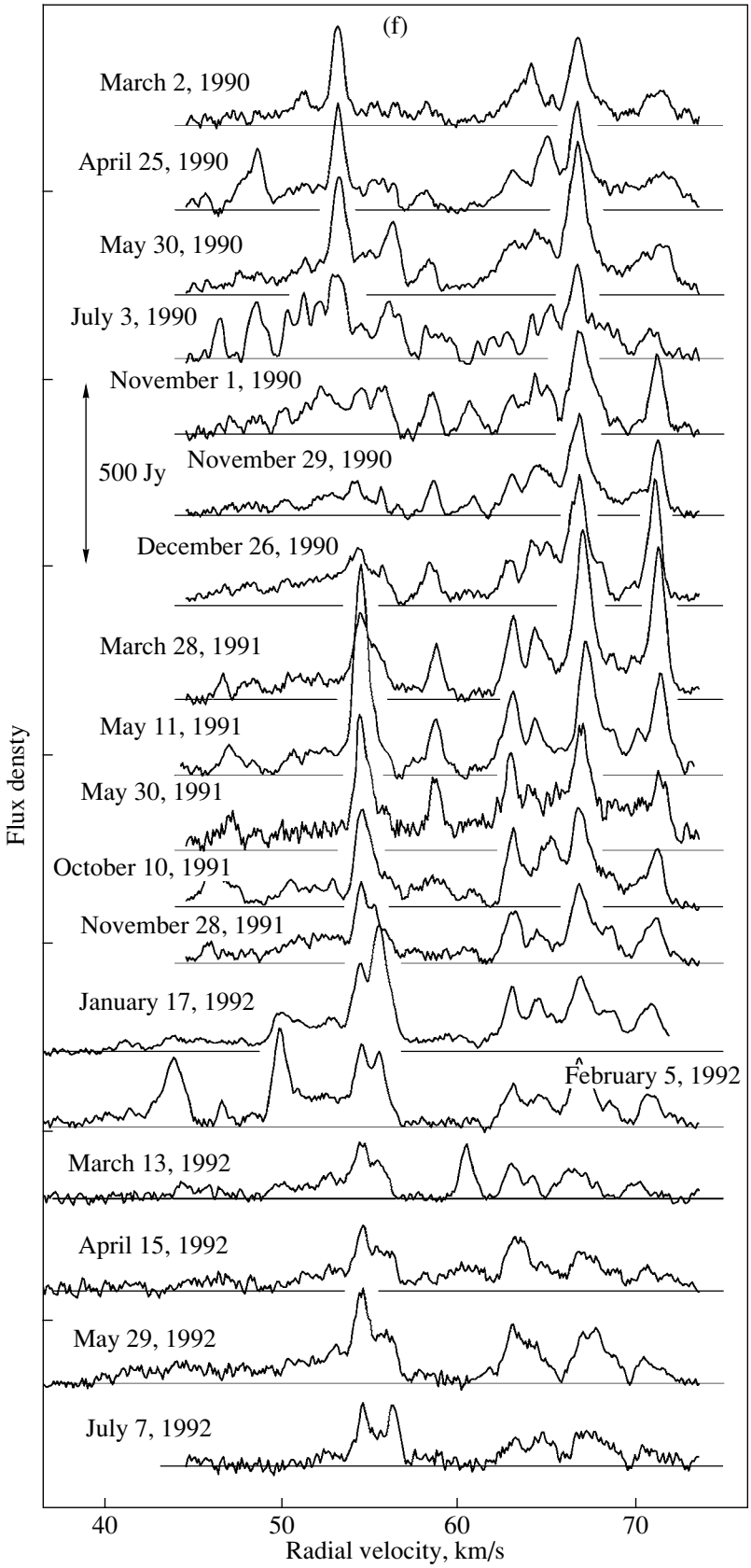
(f)
March 2, 1990
April 25, 1990
May 30, 1990
July 3, 1990
November 1, 1990
500 Jy
November 29, 1990
December 26, 1990
March 28, 1991
May 11, 1991
May 30, 1991
October 10, 1991
November 28, 1991
January 17, 1992
February 5, 1992
March 13, 1992
April 15, 1992
May 29, 1992
July 7, 1992
Flux densty
40
50
60
70
Radial velocity, km/s

Fig. 1. (Contd.)

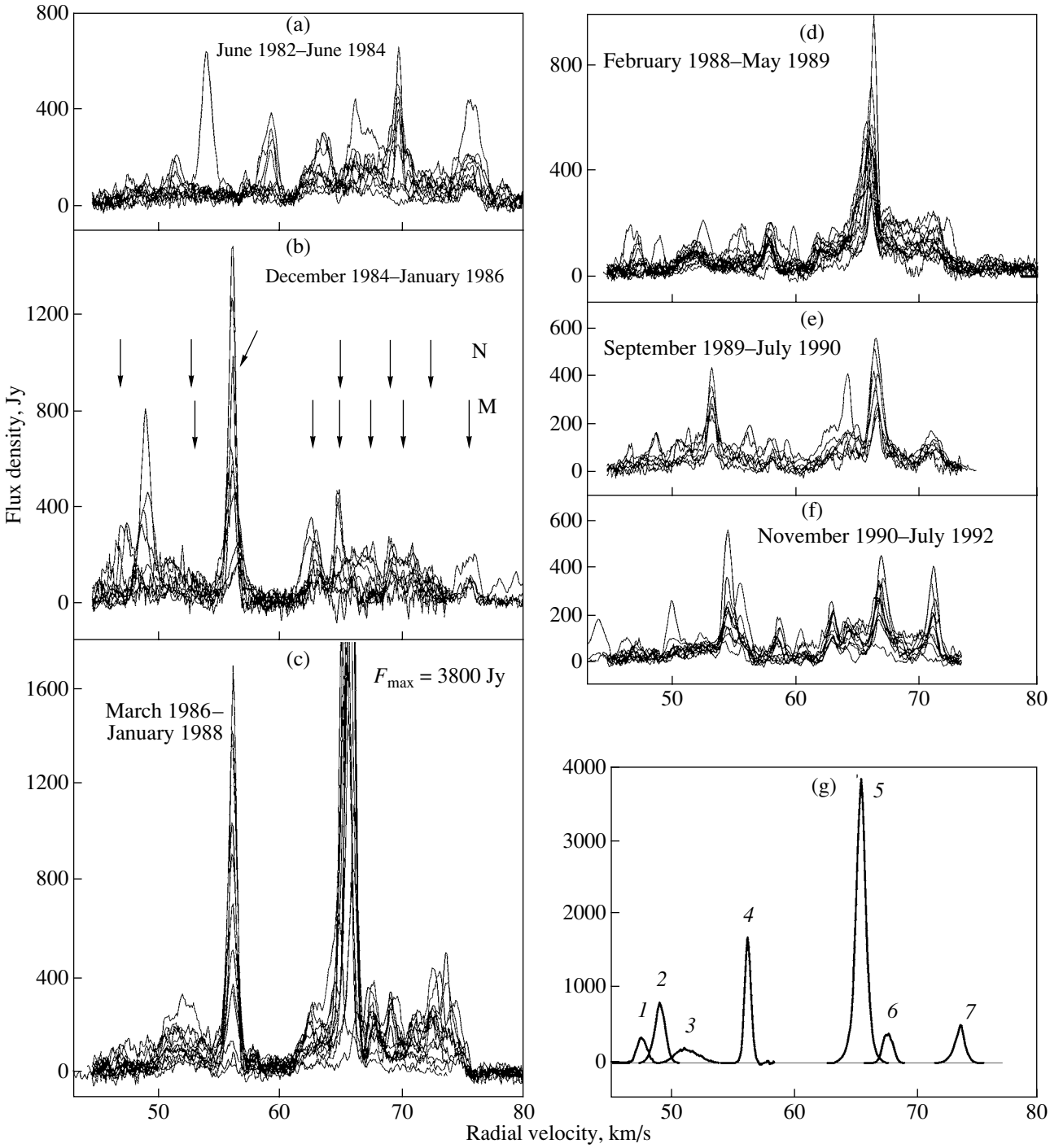

Fig. 2. (a)–(f) Superposition of H_2O maser spectra for Sgr B2 for various time intervals and (g) a synthesized spectrum for the flare of 1986–1987. See text for details.

was a drift of the emission in the spectrum, the values of V_{LSR} for the corresponding epochs are presented.

3. DISCUSSION

Searches for regular behavior in the variability of the Sgr B2 maser emission are made difficult by the fact that there are two main clusters of maser spots, in Sgr B2(N) and Sgr B2(*M*), as well as by the complexity of the Sgr B2(N) region itself. The total extent of this region is $4'' \times 4''$, within which there are a number of individual maser spots and groups of spots [11]. The maser spots of interest to us form an

Main characteristics of individual H_2O flare components in Sgr B2

Feature number	V_{LSR}, km/s	ΔV, km/s	Flux density, Jy	Integrated flux, Jy km/s	Epoch of maximum
1	47.5	0.94	340	334	Oct. 1985
2	49.0	0.98	800	850	March 1985
3	51.2	2.2	185	408	Apr. 1985
4	56.2	0.61	1680	1090	March 1986
5	65.5	0.86	3800	3890	Nov. 1986
6	67.6	1.0	390	400	Dec. 1986
7	73.5	0.86	506	500	Feb. 1987

elongated structure $4'' \times 2''$ in size. For a distance to Sgr B2 of 10 kpc, this corresponds to $(6 \times 3)\ 10^{17}$ cm or (0.2×0.1) pc. This configuration could reflect a connection with the bipolar outflow [13]. This region of maser emission is located at the edge of the compact HII region K [7] and is likely associated with intense infrared sources embedded in the molecular cloud [14] and the system of supercompact HII regions K1 and K2, which are located to the southwest of K [5].

3.1. The Flare of 1986–1987

As we can see from our monitoring of the H_2O maser (Fig. 1), the most important event was a strong flare of the maser emission that lasted two years, from the end of 1985 until the end of 1987. This flare was characterized first and foremost by strong variations of two features, at 55.5 and 65.4 km/s. According to Kobayashi *et al.* [11], the former feature belongs to Sgr B2(N). The latter feature, which is the strongest, appeared after the observations of [11], so that we have no direct answer to the question of whether it was associated with Sgr B2(N) or Sgr B2(*M*). The maser emission in Sgr B2 (*M*) forms a compact group (0.05×0.08) pc in size (in α and δ) located $45''$ to the south of Sgr B2(N). The Pushchino 22-m antenna does not resolve these two sources.

Analysis of the flux and radial velocity of the emission near 65 km/s (Fig. 3) showed that there was probably a strong flare at $V_{LSR} = 65.4$ km/s in May–August 1986. There is good reason to think that this flare, like flares of other features during this period, occurred in Sgr B2(N). Evidence in support of this possibility is the following.

1. The flare emission at 55.5 km/s is associated with Sgr B2(N) [11].

2. The character of the flux variations at 55.5 and 65.4 km/s is similar but with a time delay between them of 8–10 months (Fig. 3).

3. Emission at 71–74.5 km/s was observed during the period of the flare, in 1986–1987. According to Kobayashi *et al.* [11], this emission is associated with Sgr B2(N).

4. Strong emission (800 Jy at its maximum) was observed at 49 km/s, while no emission at 44–51 km/s was observed in the direction of Sgr B2(*M*) [11].

5. The velocity of the most intense feature is close to the central velocity of the NH_3 emission in the direction of Sgr B2(N), equal to 64 km/s [13].

Since the distance to Sgr B2 is 10 kpc, we conclude that the strength of the 1986–1987 flare was comparable to that of the megamaser emission in Orion in 1979–1987. If the Sgr B2(N) maser were located at the same distance as Orion, the flux from the feature at 65.4 km/s would have reached 1.5×10^6 Jy, and that from the feature at 55.4 km/s, about 0.7×10^6 Jy. This is only a modest factor lower than the maximum flux of the flare in Orion. Matveenko *et al.* [15] explain the megamaser emission in Orion by invoking the presence of a maser cloud with a kinetic temperature of 100 K and a radial velocity (7.8 km/s) close to the velocity of some components in the H_2O spectrum. There is selective amplification of the emission of a group of components with velocities near 7.8 km/s in the cloud [15].

The case of Sgr B2(N) is different, since two components are separated by 10 km/s in radial velocity. The components themselves display complex structures, and the line profiles were only occasionally simple Gaussians. We can see from the table that all the components of the 1986–1987 flare were fairly broad during the maximum emission. One exception is the second most intense flare feature, whose radial velocity was 56.2 km/s in March 1987, with the width of the line being 0.61 km/s. Complex line profiles are formed when maser spots with very similar V_{LSR}

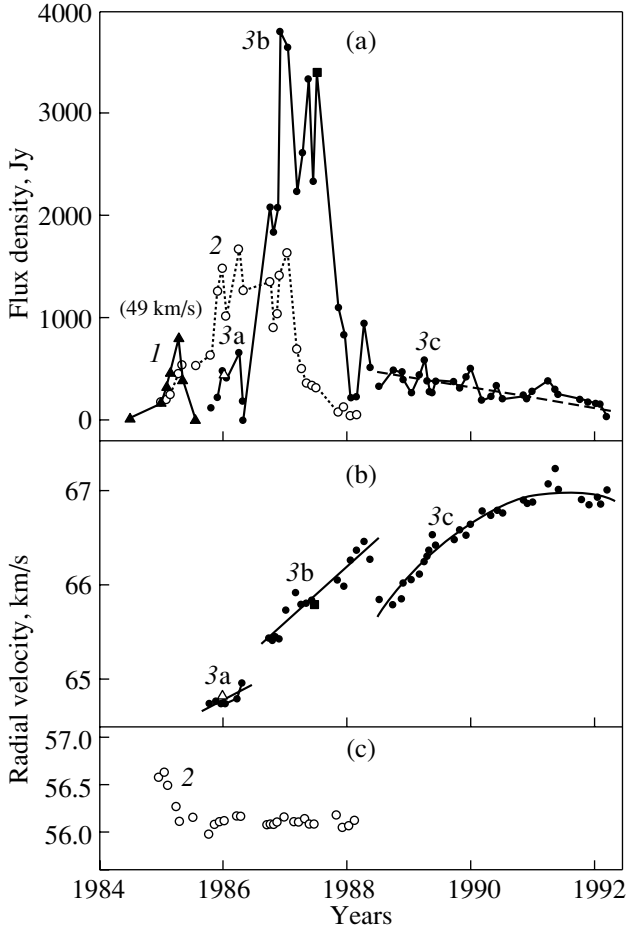

Fig. 3. Variability of the fluxes and radial velocities of the main emission features. The hollow triangles show values taken from Kobayashi *et al.* [11], and the hollow squares, values from the catalog of Comoretto *et al.* [12].

values have a complex spatial structure. As in the case of the Orion [15] and S140 [16, 17] masers, such components may form a chain of maser spots extending up to ~1 AU. The maser spots may also form a filamentary structure.

Our results for the 1986–1987 flare can be understood in the framework of the schematic of the Sgr B2(N) region from which the H_2O maser emission originates, shown in Fig. 4. There is a rotating accretion disk of molecular gas observed edge-on [4], in which the supercompact HII regions K1 and K3 are embedded. The region K3 moves toward the Earth, while K1 moves away from the Earth [8]. The numbers near these regions in the figure indicate the radial velocities derived from observations in the H66α line. The still more compact HII region K2 is located between K1 and K3, closer to K3.

The NH_3 line observations of Sgr B2(N) of Vogel *et al.* [13] led them to conclude that the emission along the direction from the northwest to the southeast divides the molecular outflow into two regions, with red and blue shifts. The outflow is perpendicular to the axis of the K1–K3 system and shifted toward the center by 0.7″ relative to the continuum source

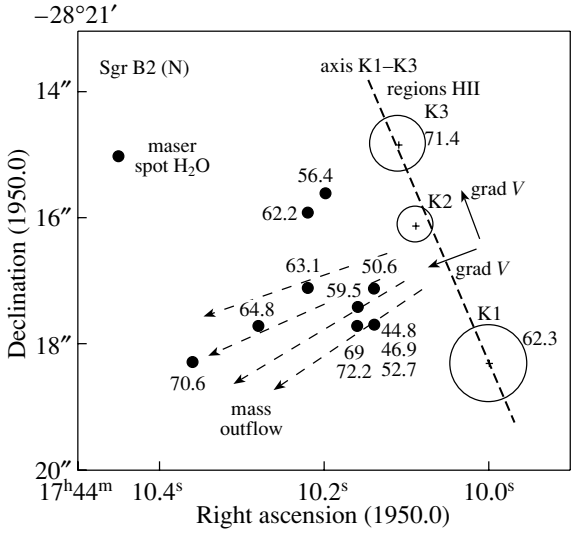

Fig. 4. Schematic of the region Sgr B2(N) (see text).

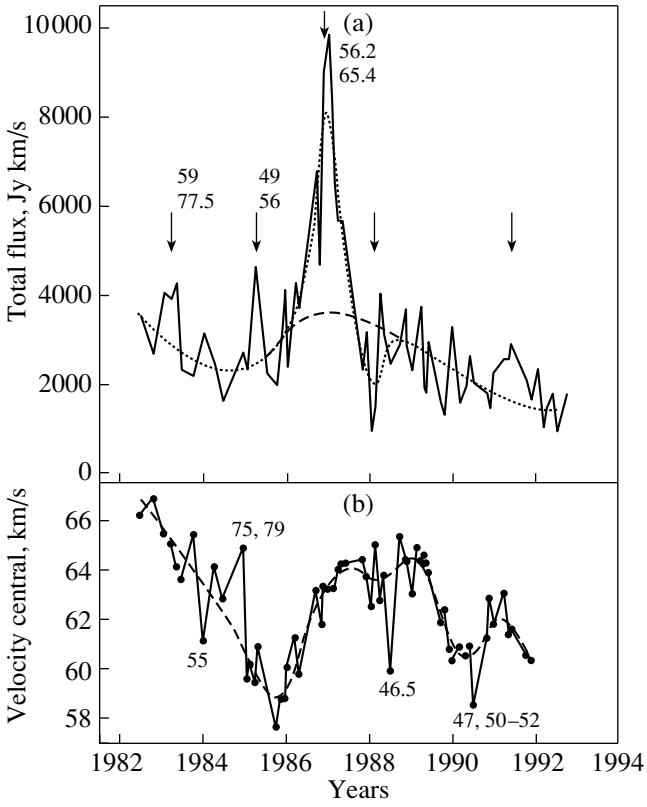

Fig. 5. Variability of the total flux and velocity centroid of the H_2O maser emission of Sgr B2. The arrows in the upper plot show the positions of maxima and the deep minimum (see text).

K2. A large velocity gradient, shown by the arrows on the right, is also observed along the direction of the outflow, as along the K1–K3 axis. We also show in Fig. 4 the maser spots providing appreciable emission at velocities of 40–80 km/s (black circles) [11]. The velocity of each maser spot is indicated.

The region of maser emission is acted on by the material flowing from the rotating accretion disk. The 1986–1987 maser flare could be associated with a strengthening of this outflow. The flares of the components (see the synthesized spectrum in Fig. 2g and the table) followed one after the other at increasingly higher velocities, with the only exception being the short-lived emission of component 1 at $V_{LSR} = 47.5$ km/s. This is qualitatively consistent with the existence of a radial-velocity gradient in the direction of the outflow. It is difficult for us to make quantitative estimates, since we do not know the positions of all the flare components.

3.2. The Main Emission Feature

The most intense emission in Sgr B2 (N) was observed at $V_{LSR} \approx 66$ km/s, close to the central velocity derived from the integrated emission in the H66α line from K1 and K3 [8]. The radial-velocity variability is complex (Fig. 3b) and can be divided into three separate intervals. The flux-variability curve (Fig. 3a) can also be divided into three intervals: curves *3*a, *3*b, and *3*c. The characters of the flux and radial-velocity variability in these intervals are different. Most importantly, we note the existence of two jumps in the radial velocity, by about 0.5 km/s in both cases. There is no doubt of the reality of these jumps. The velocities for curves *3*a and *3*b taken from Kobayashi *et al.* [11] and Comoretto *et al.* [12] are in agreement with our own data. In addition, the fluxes measured by us and by Kobayashi *et al.* [11] in December 1985 coincide (curve *3*a).

This suggests that emission appeared successively in three different features with similar radial velocities. This is supported by the lines fit for curves *3*a and *3*b and the polynomial fit for curve *3*c (Fig. 3b), which do not join one another. The drift of features *3*a and *3*b reaches 1 km/s per year. Such a drift can appear in the spectrum for two reasons: due to a real acceleration of the maser spots by the outflowing material from the disk or due to the successive excitation by the outflow of distinct maser regions with different but similar radial velocities. In both cases, we will observe a spatial shift of the maser spots.

This result is supported by the proper motions of the H_2O maser spots detected by Reid *et al.* [18], who suggested that these proper motions could be understood as a combination of rotation and outflow.

3.3. Variability of the Total Flux

The strong flare of 1986–1987 in Sgr B2(N) determined the appearance of the total-flux variability for the entire Sgr B2 region (Fig. 5a). The total flux variations primarily repeat those for the flux of the main emission feature at 65.4 km/s and, to some extent, the feature at 55.5 km/s.

The variability of the velocity centroid is regular rather than chaotic. The slow variations of this centroid within an interval of nearly 7 km/s can be clearly traced (dashed curve in Fig. 5b). Short-term velocity jumps of from 2 to 4 km/s due to flares of individual emission features are superposed on these variations. There is no correlation between the variations of the total flux and of the velocity centroid.

The activity of the H_2O maser emission in Sgr B2(N) is not related to any supercompact HII regions (K1, K2, or K3) and is instead associated with outflow from the rotating accretion disk. Previous studies of the long-term variability of masers have been carried out only for sources associated directly with specific supercompact HII regions. In those cases, it was possible to detect components of the long-term variability with periods from 4 to 18 yrs (see, for example, [19]).

We were not able to detect such a variability component for Sgr B2(N), even when we included the results of our monitoring of Sgr B2 for 1993–2003. This suggests that the time scales associated with the manifestation of accretion-disk activity differ from those for individual HII regions. The detection of the flare following the 1986–1987 flare would provide information about the period of the accretion-disk activity, which would be of considerable interest for studies of the evolution of such disks.

It seems quite natural to us to suggest that a multiple, to all appearances triple, star system is forming in this accretion disk.

4. CONCLUSIONS

(1) We have presented H_2O spectra for Sgr B2 obtained in 1982–1992.

(2) A strong flare associated with Sgr B2(N) was detected. The absolute power of this flare was close to that of the megamaser emission in Orion observed at 7.8 km/s in 1979–1987.

(3) This strong flare could be due to an enhancement of the outflow of material from a rotating accretion disk, which led to the successive excitation of maser spots with increasing radial velocities due to the presence of a gradient in V_{LSR} along the direction of the outflow.

(4) The widths of most of the emission features, especially those observed during the 1986–1987 flare in Sgr B2(N), were 0.86–2 km/s. Such emission features could be associated with a chainlike or filamentary structure, such as those observed in Orion and S140.

(5) We did not detect any long-period component of the total-flux variability for the Sgr B2(N) maser emission. This could indicate that the Sgr B2(N) maser spots are primarily associated with the outflow of material from a rotating accretion disk, and that the variability time scales for such a structure are longer than those for individual supercompact HII regions. Another possibility is that we have detected a superposition of the emission from the two independent sources Sgr B2(N) and Sgr B2(S), which could lead to a loss of information about the long-period variability of each of these sources individually.

ACKNOWLEDGMENTS

The 22-m radio telescope is supported by the Ministry of Industry and Science of the Russian Federation (registration number 01-10). The authors thank the staff of the Pushchino Radio Astronomy Observatory for their extensive help with the observations.

REFERENCES

1. N. Z. Scoville, P. M. Solomon, and A. A. Penzias, Astrophys. J. **201**, 352 (1975).
2. S. R. Cummins, R. A. Linke, and P. Thaddeus, Astrophys. J., Suppl. **60**, 819 (1986).
3. S. Hüttemeister, T. L. Wilson, C. Henkel, and R. Mauersberger, Astron. Astrophys. **276**, 445 (1993).
4. D. C. Lis and P. F. Goldsmith, Astrophys. J. **356**, 195 (1990).
5. R. A. Gaume, M. J. Claussen, C. G. De Pree, *et al.*, Astrophys. J. **449**, 663 (1995).
6. P. de Vicente, J. Martin-Pintado, and T. L. Wilson, Astron. Astrophys. **320**, 957 (1997).
7. J. M. Benson and K. J. Johnston, Astrophys. J. **277**, 181 (1984).
8. C. G. De Pree, R. A. Gaume, W. M. Goss, and M. J. Claussen, Astrophys. J. **451**, 284 (1995).
9. M. J. Reid and J. M. Moran, Ann. Rev. Astron. Astrophys. **19**, 231 (1981).
10. D. Downes, in *Birth and Infancy of Stars*, Ed. by R. Lucas, A. Omont, and R. Stora (North-Holland, Amsterdam, 1985), p. 557.
11. H. Kobayashi, M. Ishiguro, Y. Chikada, *et al.*, Publ. Astron. Soc. Jpn. **41**, 141 (1989).
12. G. Comoretto, F. Palagi, R. Cesaroni, *et al.*, Astron. Astrophys., Suppl. Ser. **84**, 179 (1990).

13. S. N. Vogel, R. Genzel, and P. Palmer, Astrophys. J. **316**, 243 (1987).
14. P. F. Goldsmith, R. L. Snell, and D. C. Lis, Astrophys. J. Lett. **313**, L5 (1987).
15. L. I. Matveenko, P. J. Diamond, and D. A. Graham, Astron. Zh. **77**, 669 (2000) [Astron. Rep. **44**, 592 (2000)].
16. A. M. S. Richards, E. E. Lekht, V. Samodourov, *et al.*, Astron. Soc. Pac. Conf. Ser. (in press).
17. E. E. Lekht and A. M. S. Richards, Astron. Zh. **80**, 357 (2003) [Astron. Rep. **47**, 326 (2003)].
18. M. J. Reid, M. H. Schneps, J. M. Moran, *et al.*, Astrophys. J. **330**, 809 (1988).
19. E. E. Lekht, Astron. Zh. **73**, 695 (1996) [Astron. Rep. **40**, 632 (1996)].

Translated by D. Gabuzda

Astronomy Reports, Vol. 48, No. 3, 2004, pp. 185–199. Translated from Astronomicheskiĭ Zhurnal, Vol. 81, No. 3, 2004, pp. 209–223.

Neutron-Capture Elements in Halo, Thick-Disk, and Thin-Disk Stars: Neodymium[1]

L. I. Mashonkina, L. A. Kamaeva, V. A. Samotoev, and N. A. Sakhibullin

Department of Astronomy, Kazan State University, ul. Kremlevskaya 18, 420008 Kazan 8, Russia

Received June 10, 2003; in final form, August 8, 2003

Abstract—We have derived the LTE neodymium abundances in 60 cool stars with metallicities [Fe/H] from 0.25 to −1.71 by applying a synthetic-spectrum analysis to spectroscopic observations of NdII lines with a resolution of $\lambda/\Delta\lambda \simeq 60\,000$ and signal-to-noise ratios of 100–200. We have improved the atomic parameters of NdII and blending lines by analyzing the corresponding line profiles in the solar spectrum. Neodymium is overabundant with respect to iron in halo stars, $[\mathrm{Nd/Fe}] = 0.33 \pm 0.09$, with the [Nd/Fe] ratio decreasing systematically with metallicity when $[\mathrm{Fe/H}] > -1$. This reflects an onset of efficient iron production in type I supernovae during the formation of the thick disk. The [Nd/Ba] and [Nd/Eu] abundance ratios behave differently in halo, thick-disk, and thin-disk stars. The observed abundance ratios in halo stars, $[\mathrm{Nd/Ba}] = 0.34 \pm 0.08$ and $[\mathrm{Nd/Eu}] = -0.27 \pm 0.05$, agree within the errors with the ratios of the elemental yields for the r-process. These results support the conclusion of other authors based on analyses of other elements that the r-process played the dominant role in the synthesis of heavy elements during the formation of the halo. The [Nd/Ba] and [Nd/Eu] ratios for thick-disk stars are almost independent of metallicity ($[\mathrm{Nd/Ba}] = 0.28(\pm0.03) - 0.01(\pm0.04)\,[\mathrm{Fe/H}]$ and $[\mathrm{Nd/Eu}] = -0.13(\pm0.03) + 0.05(\pm0.04)\,[\mathrm{Fe/H}]$) but are smaller in absolute value than the corresponding ratios for halo stars, suggesting that the synthesis of s-process nuclei started during the formation of the thick disk. The s-process is estimated to have contributed $\simeq 30\%$ of the neodymium produced during this stage of the evolution of the Galaxy. The [Nd/Ba] ratio decreases abruptly by 0.17 dex in the transition from the thick to the thin disk. The systematic decrease of [Nd/Ba] and increase of [Nd/Eu] with increasing metallicity of thin-disk stars point toward a dominant role of the s-process in the synthesis of heavy elements during this epoch. © *2004 MAIK "Nauka/Interperiodica"*.

1. INTRODUCTION

Neutron-capture processes in which elements heavier than iron are synthesized can be subdivided into slow (s) and rapid (r) processes. r-process reactions occur when the neutron density is high and are associated with type II supernovae. s-process reactions can occur in the cores of massive stars ($M \geq 20M_\odot$) during the hydrostatic burning of the helium core and in intermediate-mass stars (2–$4M_\odot$) during nonstationary double-shell burning (asymptotic giant branch stars). According to theoretical concepts [1], the s-process in massive stars is responsible for the lightest of the heavy elements (those with atomic masses $A \leq 85$). The atomic masses of the elements that we discuss here are much higher: $A_{\mathrm{Ba}} = 134$–138, $A_{\mathrm{Nd}} = 142$–148, and $A_{\mathrm{Eu}} = 151, 153$, and the s-process nuclei of these elements are synthesized in intermediate-mass stars; here and below, we will always be referring to this component of the s-process.

Heavy elements in the solar system were synthesized in both s- and r-process reactions, but the proportions differ from element to element. According to Arlandini *et al.* [2], the contributions of the s and r-processes are $s : r = 81 : 19$ for barium, $56 : 44$ for neodymium, and $6 : 94$ for europium. The time scales for the synthesis of s- and r-process nuclei differ substantially, and the $s : r$ ratio for each element and the abundance ratios for various elements have varied over the lifetime of the Galaxy. The data of Arlandini *et al.* [2] can be used to calculate the abundance ratios during the epoch when nucleosynthesis was dominated by the r-process; the corresponding ratios (relative to the solar values) are $[\mathrm{Eu/Ba}]_r = \log(\mathrm{Eu/Ba})_r/(\mathrm{Eu/Ba})_\odot = 0.70$; $[\mathrm{Eu/Nd}]_r = 0.33$, and $[\mathrm{Nd/Ba}]_r = 0.36$. After the first intermediate-mass stars completed their evolution and s-process nuclei began to enrich the interstellar medium, the production rate of barium became higher than the

[1] Based on observations made at the European Southern Observatory (Chile) in the framework of the project 67.D-0086A and at the German–Spanish Astronomical Center (Calar Alto, Spain).

1063-7729/04/4803-0185$26.00

production rates of neodymium and europium, and the [Eu/Ba], [Eu/Nd], and [Nd/Ba] ratios began to decrease, reaching the solar values by the epoch of formation of the solar system. Thus, an analysis of the elemental abundance ratios observed in stars can be used to identify the dominant nucleosynthesis mechanisms during various stages in the life of the Galaxy and to estimate the time scales for the corresponding epochs by comparing the results with theoretical models of chemical evolution of the Galaxy.

Starting from the pioneering work of Spite and Spite [3], numerous studies have yielded theoretical and observational evidence suggesting that the heavy elements in halo stars were synthesized via the r-process ([4–6] are the most important works in this field). Gratton *et al.* [7, 8], Fuhrmann [9], Prochaska *et al.* [10], and Feltzing *et al.* [11] analyzed the abundances of α-process elements, found evidence for different chemical evolution of the thick and thin disks, and concluded that the formation of the stellar population of the thick disk dates back to the early Galaxy. Bernkopf *et al.* [12] used evolutionary tracks to determine the ages of three thick-disk subgiants with an accuracy of ± 1 Gyr and found them to be from 12.5 to 13.8 Gyr. To understand the evolution of the Galaxy, it is important to find evidence confirming the differences in the chemical evolution of the thick and thin disks based on elements synthesized in other types of nuclear reactions besides the α-process elements and in other types of stars. It would also be of considerable interest to determine how much the chemical evolution of the thick disk differs from that of the halo. Analyses of abundances of α-process elements cannot provide an answer to the latter question.

In our earlier papers [13–15], we determined the abundances of barium and europium in 78 stars belonging to the thin-disk, thick-disk, and halo populations. Our abundance analyses yielded evidence that these three populations displayed different chemical evolution. We were the first to demonstrate that the r-process played the dominant role in the synthesis of heavy elements not only during the formation of the halo but also during the formation of the thick disk, in contrast to the situation in the thin disk, where the s-process was dominant. This result independently supports the conclusion based on the analysis of abundances of α-process elements that the stellar population of the thick disk is much older than that of the thin disk. We also found that the abundance ratios behaved differently for halo and thick-disk stars: unlike halo stars, thick-disk stars exhibit signs of the onset of iron synthesis in type I supernovae and of barium synthesis in asymptotic giant branch stars.

To improve the reliability of earlier conclusions based on abundance analyses for barium and europium, we have determined the neodymium abundances for the same sample of stars and analyze the [Nd/Fe], [Nd/Eu], and [Nd/Ba] abundance ratios from the viewpoint of the chemical evolution of the Milky Way.

We determined the neodymium abundances from five NdII lines, which are fairly weak even in stars with normal, i.e., solar, metallicities. We took the following measures to increase the accuracy of the results.

(1) We use observations with high spectral resolution $\lambda/\Delta\lambda \simeq 60\,000$ and high signal-to-noise ratios (>200 in most cases). We describe the observational material in Section 2.

(2) Our list of program stars consists of stars on or near the main sequence. We imposed this restriction to reduce methodological errors associated with modeling of the stellar atmospheres and theoretical spectra and determination of the atmospheres' parameters. We included several metal-deficient subgiants in our list, but $\log g \geq 3.12$ for all the stars in the sample. We excluded known spectral binaries and stars with relatively fast rotational velocities ($V \sin i > 4$ km/s).

(3) For all the stars, including the Sun, which is our comparison star, we used atmospheric parameters (effective temperature $T_{\rm eff}$, surface gravity $\log g$, iron abundance [Fe/H], and microturbulence velocity $V_{\rm mic}$) obtained using the same methods. We report the parameters and their uncertainties in Section 2.

(4) We used a differential approach to determine the neodymium abundances. We first analyzed the NdII in the solar spectrum (Section 3) to empirically improve the oscillator strengths, which we then used in our analysis of the stellar spectra. This approach minimizes the effect of uncertainties in the atomic-line parameters on the results obtained.

(5) We computed the abundances using synthetic spectra, i.e., by analyzing the line profiles rather than their equivalent widths.

Section 4 presents the results of our neodymium abundance estimates and discusses the behavior of the [Nd/Fe], [Nd/Eu], and [Nd/Ba] abundance ratios in stars of the thin disk, thick disk, and halo. We summarize our results in the Conclusions.

2. OBSERVATIONAL MATERIAL, STELLAR PARAMETERS, AND MODEL ATMOSPHERES

We determined the neodymium abundances for 60 of the 78 stars studied by Mashonkina *et al.* [15]. We obtained spectroscopic observations of seven stars in April 2001 with the UVES echelle spectrometer

Table 1. List of program stars, their parameters, and neodymium abundances [Nd/Fe] averaged over various lines

HD/BD	$T_{\rm eff}$, K	$\log g$	$V_{\rm mic}$, km/s	[Fe/H]	[Nd/Fe]		Code
1	2	3	4	5	6		7
400	6150	4.06	1.3	−0.25	-0.01 ± 0.04	(2)	0
3795	5370	3.82	1.0	−0.64	0.44 ± 0.06	(5)	1
4614	5940	4.33	1.0	−0.30	0.08 ± 0.03	(4)	0
9407	5660	4.42	0.9	0.03	-0.01 ± 0.04	(3)	0
10519	5710	4.00	1.1	−0.64	0.19 ± 0.03	(3)	1
10697	5610	3.96	1.0	0.10	-0.01 ± 0.01	(2)	0
18757	5710	4.34	1.0	−0.28	0.11 ± 0.05	(4)	1
22879	5870	4.27	1.2	−0.86	0.24 ± 0.02	(3)	1
29907	5500	4.64	0.6	−1.55	0.40 ± 0.06	(4)	2
30649	5820	4.28	1.2	−0.47	0.20 ± 0.02	(5)	1
30743	6300	4.03	1.6	−0.45	0.03 ± 0.11	(2)	0
31128	5980	4.49	1.2	−1.49	0.28 ± 0.01	(2)	1
37124	5610	4.44	0.9	−0.44	0.13 ± 0.04	(2)	1
43042	6440	4.23	1.5	0.04	-0.07 ± 0.04	(4)	0
45282	5280	3.12	1.4	−1.52	0.30	(1)	2
52711	5890	4.31	1.0	−0.16	0.03 ± 0.03	(3)	0
55575	5890	4.25	1.0	−0.36	0.06 ± 0.04	(2)	0
59392	6010	4.02	1.4	−1.59	0.45 ± 0.03	(4)	2
61421	6470	4.00	1.9	−0.01	-0.18 ± 0.02	(2)	0
62301	5940	4.18	1.2	−0.69	0.21 ± 0.03	(5)	1
64606	5320	4.54	1.0	−0.89	0.27 ± 0.02	(3)	1
65583	5320	4.55	0.8	−0.73	0.27 ± 0.06	(3)	1
67228	5850	3.93	1.2	0.12	-0.14 ± 0.07	(4)	0
68017	5630	4.45	0.9	−0.40	0.13 ± 0.05	(4)	1
69611	5820	4.18	1.2	−0.60	0.16 ± 0.08	(4)	1
90508	5800	4.35	1.0	−0.33	0.17 ± 0.04	(4)	01
97320	6110	4.27	1.4	−1.18	0.23 ± 0.06	(4)	1
102158	5760	4.24	1.1	−0.46	0.16 ± 0.03	(5)	1
102200	6115	4.20	1.4	−1.24	0.26 ± 0.02	(4)	1
103095	5110	4.66	0.8	−1.35	0.35 ± 0.05	(3)	2
109358	5860	4.36	1.1	−0.21	0.04 ± 0.03	(2)	0
112758	5240	4.62	0.7	−0.43	0.20 ± 0.01	(3)	1
114710	6000	4.30	1.1	−0.03	0.08 ± 0.03	(2)	0
117176	5480	3.83	1.0	−0.11	0.07 ± 0.03	(4)	0
121560	6140	4.27	1.2	−0.43	0.14 ± 0.01	(3)	0

Table 1. (Contd.)

1	2	3	4	5	6		7
122196	6000	3.99	1.5	−1.71	0.23 ± 0.03	(2)	2
126053	5690	4.45	1.0	−0.35	0.10 ± 0.02	(3)	0
130322	5390	4.55	0.8	0.04	0.08 ± 0.04	(2)	0
132142	5240	4.58	0.7	−0.39	0.20 ± 0.01	(3)	1
134987	5740	4.25	1.0	0.25	−0.13	(1)	0
142373	5840	3.84	1.2	−0.57	0.13 ± 0.01	(5)	0
144579	5330	4.59	0.8	−0.69	0.27 ± 0.02	(2)	1
148816	5880	4.07	1.2	−0.78	0.15 ± 0.04	(4)	1
157214	5735	4.24	1.0	−0.34	0.09 ± 0.04	(4)	1
168009	5785	4.23	1.0	−0.03	−0.04 ± 0.06	(2)	0
176377	5860	4.43	0.9	−0.27	0.17 ± 0.05	(2)	0
179957	5740	4.38	0.9	−0.01	−0.01 ± 0.04	(4)	0
179958	5760	4.32	0.9	0.02	0.01 ± 0.02	(4)	0
186408	5800	4.26	1.0	0.06	0.07	(1)	0
187923	5730	4.01	1.1	−0.17	0.10 ± 0.02	(2)	01
188512	5110	3.60	0.9	−0.17	0.20 ± 0.04	(4)	0
194598	6060	4.27	1.4	−1.12	0.25	(1)	2
195019	5800	4.16	1.0	0.04	0.00 ± 0.07	(4)	0
198149	4990	3.40	1.0	−0.14	0.20 ± 0.01	(3)	0
201891	5940	4.24	1.2	−1.05	0.35	(1)	1
209458	6080	4.33	1.1	−0.06	0.12 ± 0.00	(2)	0
222794	5620	3.94	1.2	−0.69	0.21 ± 0.07	(4)	1
298986	6130	4.30	1.4	−1.34	0.23 ± 0.03	(2)	2
18°3423	6070	4.28	1.4	−0.90	0.45	(1)	2
0°2245	5630	3.85	1.2	−1.13	0.44 ± 0.05	(5)	1

Note: In column 6, the number of lines used is given in parentheses. Column 7 gives a code indicating the Galactic population: thin disk (0), thick disk (1), halo (2), or the transition between the thin and thick disks (01).

mounted on the 8-m VLT2 telescope of the European Southern Observatory in Chile (project 67.D-0086A). These observations cover 3800–4500 Å and 4750–6650 Å and have a resolution of $\lambda/\Delta\lambda \simeq 60\,000$ and signal-to-noise ratios >200. Spectroscopic observations of 53 stars at 4100–6700 Å were obtained in 1995–2001 by K. Fuhrmann (51 stars), T. Gehren (one star), and A. Korn (one star) with the FOCES echelle spectrometer mounted on the 2.2-m telescope of the German–Spanish Astronomical Center in Calar Alto, Spain. The resolution was $\lambda/\Delta\lambda \simeq 40\,000$ for the 1995 4 stars observations

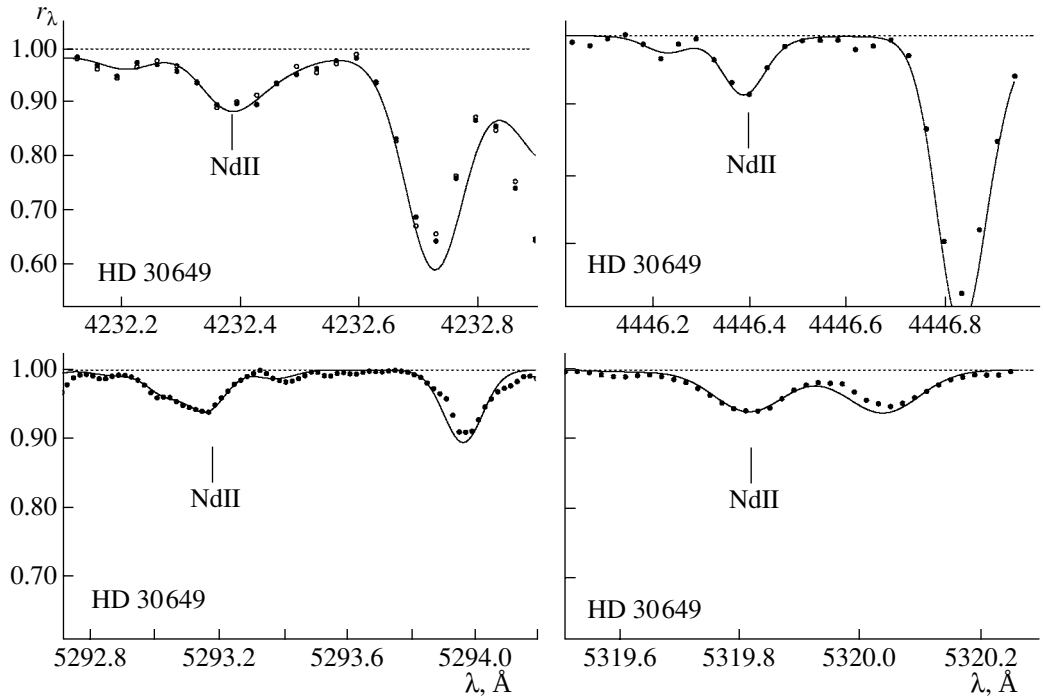

Fig. 1. Comparison of observed (dashed) and theoretical (solid) profiles of NdII lines in the spectrum of HD 29907 obtained using the 8-m VLT2 telescope. The neodymium abundances derived using various lines are [Nd/Fe](λ4232) = 0.48, [Nd/Fe](λ4446) = 0.33, [Nd/Fe](λ5293) = 0.38, and [Nd/Fe](λ5320) = 0.41.

and $\lambda/\Delta\lambda \simeq 60\,000$ for the remaining spectra. The signal-to-noise ratio increases from 100 to 200 as the wavelength increases from 4400 to 5400 Å and is $\sim$30 only in the vicinity of 4200 Å. Each star was observed at least twice.

Table 1 gives a list of the stars studied. Figures 1 and 2 show portions of the spectra containing NdII lines for the stars HD 29907 and HD 30649, observed using the 8-m and 2.2-m telescopes, respectively.

When determining the parameters of the stellar atmospheres, we applied the same methods to all the stars. These analyses were performed by Fuhrmann [9, 16] (51 stars) and Mashonkina *et al.* [15] (all remaining stars). The effective temperatures were derived from the profiles of the H_α and H_β lines; the surface gravities $\log g$ were determined using two methods—by analyzing the wings of strong MgI lines at λ5172 and λ5183 affected by van der Waals broadening, and from the HIPPARCOS trigonometric parallaxes. The relative iron abundance [Fe/H] and microturbulence velocity $V_{\rm mic}$ were derived from FeII lines by assuming local thermodynamic equilibrium (LTE), since published non-LTE computations for FeII lines have revealed no appreciable non-LTE effects. We estimated the accuracy of the derived effective temperatures to be $\Delta T_{\rm eff} = 80$ K by comparing the results obtained for two lines and also by comparing our results with those obtained in other studies using various photometric indices. We estimated the accuracy of $\log g$ to be $\Delta \log g = 0.1$ by comparing the spectroscopic and trigonometric-parallax results. Estimating the errors in [Fe/H] and $V_{\rm mic}$ as the combined effects of the scatter of the data for different FeII lines and the uncertainties in the stellar parameters yielded Δ[Fe/H] = 0.1 dex and $\Delta V_{\rm mic} = 0.1$ km/s. All the stars are located in a narrow interval of effective temperatures (from 5110 to 6470 K) and surface gravities $\log g$ (from 3.12 to 4.66); the iron abundances [Fe/H] range from 0.25 to -1.71. The resulting parameters are listed in Table 1.

We used plane-parallel, homogeneous, blanketed model atmospheres computed using the MAFAGS program developed at Munich University [17] for both the Sun and the stars. Allowance for the effects of convection was based on mixing-length theory with the mixing-length l to the pressure scale height H_p ratio being $l/H_p = 0.5$. We took into account the opacity due to $\sim$58 million atomic and molecular lines using the opacity distribution functions of Kurucz [18], which we scaled by -0.16 dex (on a logarithmic scale) to bring the abundance of iron, whose lines are the main contributors to the opacity distribution functions, into agreement with the standard values: $\log \varepsilon_{\rm Fe} = 7.51$ for the Sun [19]. Here and below, we use an abundance scale for which $\log \varepsilon_{\rm H} =$

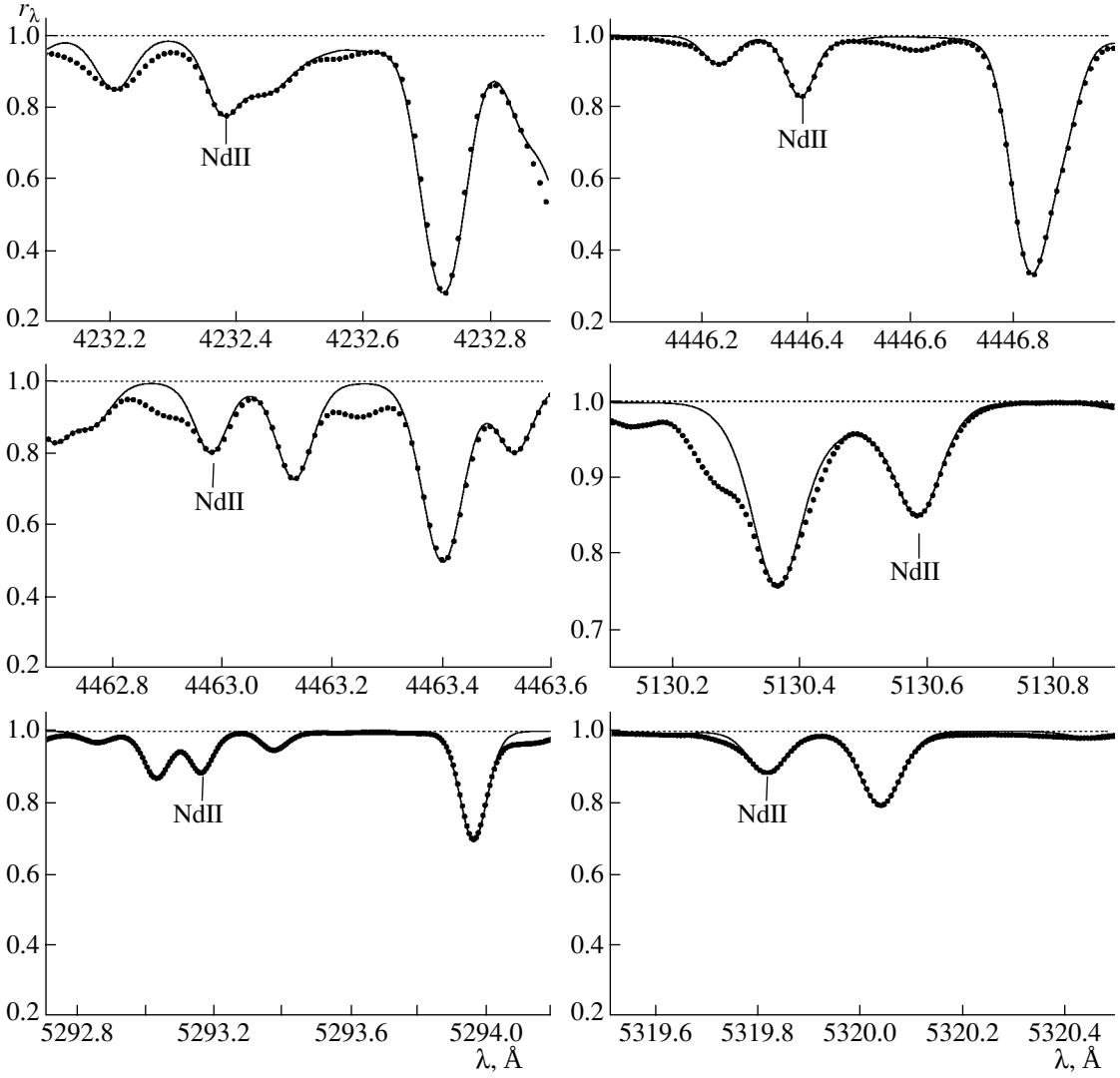

Fig. 2. Comparison of the observed (dashed) and theoretical (solid) profiles of NdII lines in the spectrum of HD 30649 obtained using the 2.2-m telescope. The neodymium abundances inferred from various lines are [Nd/Fe](λ4232) = 0.21, [Nd/Fe] (λ4446) = 0.18, [Nd/Fe](λ5293) = 0.20, and [Nd/Fe](λ5320) = 0.20.

12. In the case of metal-deficient stars, one of the model-atmosphere parameters is the abundance of elements that are donors of free electrons (Mg, Si, Ca). We assumed that [Si/Fe] = [Ca/Fe] = [Mg/Fe] when computing the model atmospheres for each star, adopting the magnesium abundances from [9, 15, 16].

Our analysis of the abundance ratios took into consideration the Galactic population to which each star belongs: thin disk, thick disk, or halo. The population type for each star was identified using four criteria: the space velocity of the star V_{pec} and its components, the [Mg/Fe] ratio, the iron abundance, and the estimated age of the star. Thick-disk stars can be confidently distinguished from thin-disk stars despite the small overlap of the metallicity intervals covered by these two populations: thick-disk stars are characterized by higher V_{pec}, 100–200 km/s, an overabundance of magnesium relative to iron, [Mg/Fe] $\simeq$ 0.4, and ages exceeding 9 Gyr. We estimated the ages of the stars using evolutionary tracks. Halo and thick-disk stars were distinguished on essentially one criterion—their space velocities. In the sample studied, stars of these populations have partially overlapping metallicity intervals (from -0.9 to -1.5) and similar magnesium overabundances ([Mg/Fe] $\sim$0.4) and ages. We classified stars with $V_{pec} > 200$ km/s as halo objects. We adopted the population identifications of Fuhrmann [9, 16] and Mashonkina *et al.* [15].

Table 2. Parameters of the NdII lines analyzed

NdII lines				Blending lines			
λ, Å	E_{low}, eV	$\log gf$		λ, Å; Ion		E_{low}, eV	$\log gf\varepsilon$
		emp	VALD [20]				
4232.380	0.060	−0.60	−0.30	4232.435	CrII	4.988	3.41
				4232.450	VI	1.950	3.89
				4232.488	CaI	4.769	5.61
				4232.541	VI	1.849	3.21
4446.390	0.200	−0.54	−0.59	4446.287	FeII	5.930	5.43
4462.982	0.560	−0.03	0.07	4463.133	FeI	3.060	4.57
				4462.9	?		
5130.589	1.300	0.53	0.57	5130.366	NiI	3.820	4.98
				5130.452	CrI	3.435	4.08
				5130.529	VI	2.616	4.01
5293.165	0.820	−0.08	−0.06	5293.035	FeI	4.370	5.44
5319.817	0.550	−0.32	−0.21	5319.72	?		

Note: The quantities $\log gf$(emp) for NdII lines and $\log gf\varepsilon$ for blending lines were derived from an analysis of line profiles in the solar spectrum. We assumed that the solar abundance of neodymium is equal to the meteoritic abundance, $\log \varepsilon_{\rm Nd} = 1.49$ [19].

3. ANALYSIS OF NdII LINES IN THE SOLAR SPECTRUM

The choice of NdII lines for determining the neodymium abundances in the program stars was dictated by the following:

(a) the spectral interval observed, 4100–6600 Å;

(b) the detectability of these lines in metal-deficient stars;

(c) the absence of strong blending lines.

After a preliminary analysis of ten NdII lines in the solar spectrum and the spectrum of a star with [Fe/H] = −0.64, we chose the six lines listed in Table 2.

We used the observed spectrum of the Sun as a star from the atlas of Kurucz *et al.* [21]. The model atmosphere for the Sun was computed using the MAFAGS program with $T_{\rm eff} = 5780$ K, $\log g = 4.44$, and [M/H] = 0. All the synthetic spectra were computed assuming LTE using the SIU code developed by T. Gehren and J. Reetz (Munich University); A. Korn kindly presented by us his Windows version of this code. The list of spectral lines included all atomic and molecular lines from the tables of Kurucz [18].

We searched for possible non-LTE effects in the NdII absorption lines. The NIST atomic database (http://aeldata.phy.nist.gov/archive/) contains experimental data for the energies of 706 NdII levels with excitation energies below 6 eV. Both low-excitation and high-excitation NdII terms are characterized by an appreciable energy separation of the fine-splitting sublevels ($\Delta E \sim 0.1$–0.2 eV). Combined with the fact that each electronic configuration with one ($4f^4nl$) or two ($4f^35dnl$) excited electrons has several terms with similar energies, this results in diffrent terms overlapping in energy. In this case, collisional processes should play the dominant role in populating the levels, at least in the atmospheres of solar-type stars, so that deviations from LTE should not be important.

To our knowledge, no data about the hyperfine

structure of NdII lines are available. In the solar system, 21.6% of neodymium isotopes have odd mass number [2], and NdII lines should not exhibit strong hyperfine-structure effects. The measured isotopic shifts for the λ5130 and λ5320 lines can be found in [22]. The maximum component separations are 7 and 23 mÅ for the first and second lines, respectively, and the isotopic shift for the λ5320 NdII line is 14.6 mÅ for the components of the most abundant isotopes with $A = 142-146$. Analysis of the solar spectrum showed that such small component separations cannot appreciably broaden the observed line profiles. Each of the components, and even all of them together, are weak enough to be located in the linear portion of the curve of growth, and we treated each line as a single line. The error in the derived neodymium abundance due to neglect of isotopic components does not exceed 0.01 dex.

Confident identification of the NdII lines in the stellar spectra requires accurate fitting of not only the observed profiles of the NdII lines in the solar spectrum but also of stronger neighboring lines of iron-group elements, which can be identified with certainty in the stellar spectra. In all cases, such lines are located within 1 Å of the NdII lines. All the NdII lines studied are fairly weak, and we varied only one parameter, $\log gf\varepsilon$, when obtaining the best fit to the observed profile. The microturbulence velocity was fixed, $V_{\rm mic} = 0.8$ km/s. We took into account natural damping by setting the damping constant equal to its classical value and allowing for van der Waals broadening using the algorithm employed by Kurucz in his ATLAS6 and ATLAS9 programs [18]. The theoretical profiles were also broadened to allow for rotation with a velocity of $V \sin i = 1.8$ km/s and radial–tangential macroturbulence, assuming that the radial and tangential motions have Gaussian velocity distributions with the most probable velocity $V_{\rm mac}$. We varied $V_{\rm mac}$ to fit the profile shapes. This yielded the final macroturbulence velocities $V_{\rm mac} = 3.2$ km/s and $V_{\rm mac} = 3.6-3.8$ km/s for lines in the blue and green parts of the spectrum, respectively. Figure 3 shows the best fits.

We took the solar neodymium abundance to be equal to the meteoritic abundance, $\log \varepsilon_{\rm Nd} = 1.49$ [19], and computed the solar oscillator strengths for the NdII lines based on the derived $\log gf\varepsilon$ values. The resulting oscillator strengths are listed in Table 2 in the column $\log gf$—(emp). These values are obviously model dependent, and we cannot claim that they are completely accurate. However, if the model atmosphere correctly reflects the distribution of physical parameters, at least in the region of formation of the spectral lines, the empirically improved $\log gf$ values may be of more general use, beyond differential analyses of elemental abundances for stars and the Sun. For comparison, Table 2 lists the oscillator strengths $\log gf$ for NdII lines listed in the Vienna Atomic Line Database (VALD) [20]. It is clear that the $\log gf$ (emp) values agree with the VALD $\log gf$ values for the λ4446, λ5130, and λ5293 lines within 0.05 dex. Our oscillator strengths are 0.1 dex lower for the λ4462 and λ5320 lines and 0.3 dex lower for the λ4232 line. Table 2 also lists the empirically improved parameters of blending lines.

Figure 3 shows that only the λ4446 and λ5320 lines are free of blends. The worst blending occurs for the λ4462 line, whose blue wing contains an unidentified, possibly molecular, line. We accordingly excluded the λ4462 line from our analyses of the stellar spectra, except for the ten hottest stars of the 60 in our sample.

4. STELLAR NEODYMIUM ABUNDANCES

We used the atomic-line parameters derived from our analysis of the solar spectrum to analyze the stellar spectra. All the stars are slow rotators with $V \sin i < 4$ km/s, and the broadening of the theoretical profiles included only instrumental broadening and the effect of radial–tangential macroturbulence. According to Pfeifer *et al.* [23], the instrumental profile of the FOCES echelle spectrometer can be described by a Gaussian curve, with its half-width changing from season to season due to the use of different instrumental setups. Therefore, the halfwidth is measured each night by recording the spectrum of solar light reflected from the Moon. In our analyses of the NdII lines, we used the instrumental-profile halfwidths obtained in our previous analyses of BaII and EuII lines [13]; the halfwidth in velocity units ranges from 3.2 to 4.9 km/s for various observing seasons. All spectra observed with the 8-m telescope were taken on the same night, and our analysis of the BaII and EuII lines [15] showed that the instrumental profile of the UVES echelle spectrometer can be described satisfactorily by a Gaussian with a halfwidth of 3 km/s. The macroturbulence velocities $V_{\rm mac}$ for each of the stars were determined by Fuhrmann [9, 16] (the FOCES spectra) and Mashonkina *et al.* [15] (the UVES spectra). When analyzing the NdII lines, instrumental profile halfwidth and $V_{\rm mac}$ were allowed to vary within 0.2 km/s of their nominal values to allow for additional broadening of line profiles due to rotation.

The neodymium abundance was the only free parameter in the fitting of the observed and theoretical spectra, while the abundances of all other elements responsible for blending lines were fixed. The accuracy of the derived neodymium abundance depends,

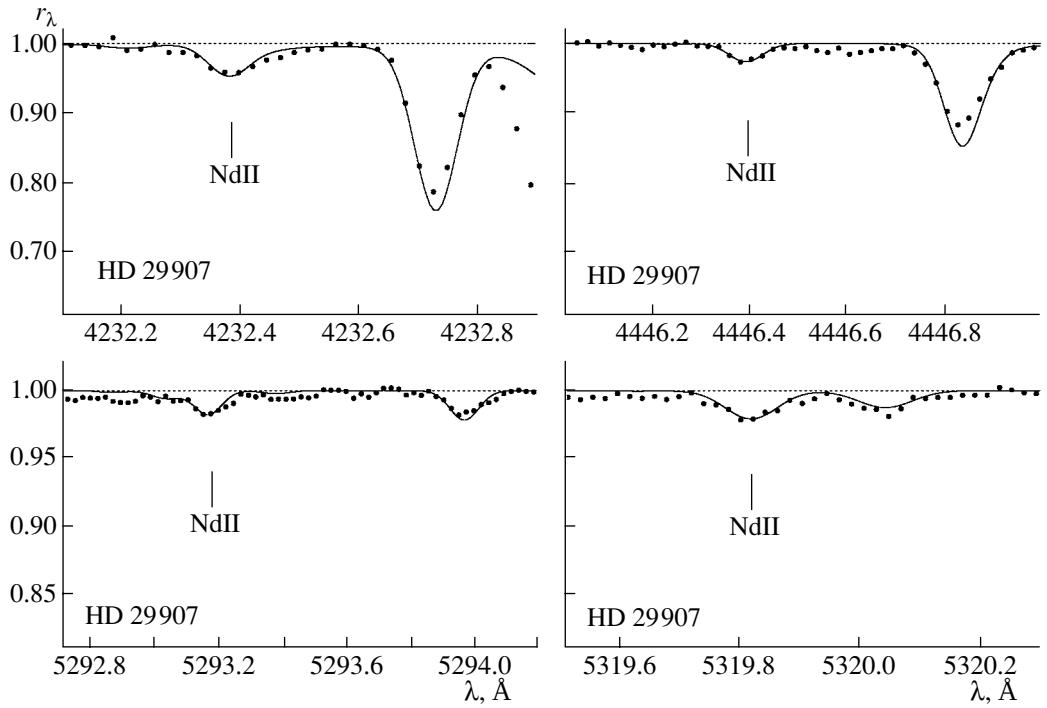

Fig. 3. Comparison of observed (dashed) and theoretical (solid) profiles of NdII lines in the solar spectrum. Parameters of the lines are listed in Table 2.

among other things, on the uncertainty in the continuum level, since the lines considered here are shallow (their depths are often of the order of a few percent) and blended with lines of other elements.

The error due to uncertainty in the continuum level can be estimated by comparing abundances derived from the same line in different spectra of a given star. As we noted above, we have at least two spectra for each of the stars observed with the 2.2-m telescope; each spectrum was usually analyzed separately. The only exception is the λ4232 line: due to the lower signal-to-noise ratio in this region ($\sim$30–50), the observed spectra were coadded (Fig. 2). The mean difference in the abundances derived from two spectra of the same star is 0.05 ± 0.04 dex.

Blending influences most strongly the λ4462 NdII line. Due to the presence of an unidentified line in its blue wing, we could determine abundances from this line for only the ten hottest stars in the sample, whose spectra displayed symmetrical λ4462 profiles. In spite of the fact that the λ5293.165 NdII and λ5293.035 FeI lines formed a single feature in the stellar spectra due to the instrumental broadening, we were able to obtain satisfactory fits between the observed and theoretical profiles and derive neodymium abundances from this line for 47 stars (Figs. 1 and 2). While the NdII line is weaker than the FeI line in stars with normal metallicities (Fig. 3), the contribution of the NdII line increases with decreasing [Fe/H], facilitating the derivation of the neodymium abundance. When analyzing the blend of the λ4232 line and the CaI λ4232.488, we assumed that the calcium and magnesium abundances were correlated: [Ca/Fe] = [Mg/Fe].

We determined the neodymium abundances in 60 stars based on one to six lines listed in Table 2; the results for only five stars are based on a single line. The λ5130 line yielded abundances that were systematically lower than those inferred from the five remaining lines, by, on average, 0.1 dex. The origin of this discrepancy is not clear, and we excluded the results for this line when deriving the final mean abundances. Figures 1 and 2 illustrate the fits of the observed NdII line profiles for HD 29907 and HD 30649. The mean neodymium abundances for several lines, their errors σ, and the number of lines used are listed in Table 1. The quoted errors include the errors associated with setting the continuum level, errors in fitting the observed profiles, and errors associated with our allowance for blending lines. The abundance errors σ for the six stars whose abundances were based on five lines do not exceed 0.06 dex; the abundance errors for the 19 stars whose abundances were based on four lines were $\sigma \leq 0.08$ dex. The abundance errors for the sample as a whole do not exceed 0.11 dex.

All the stars have narrow ranges of $T_{\rm eff}$ and $\log g$ values, and the NdII lines remain on the lin-

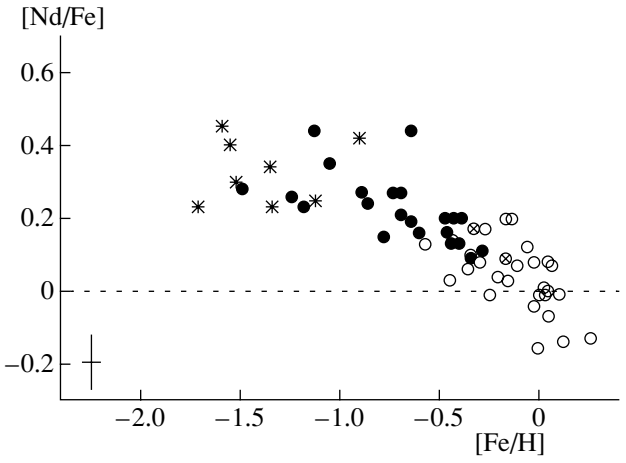

Fig. 4. Dependence of the [Nd/Fe] ratio on metallicity. The symbols show stars of the thin disk (open circles), thick disk (filled circles), and halo (asterisks); stars identified by Fuhrmann [9] as belonging to a population intermediate between the thick and thin disk populations are shown by the circled crosses. An error bar is shown in the lower left corner.

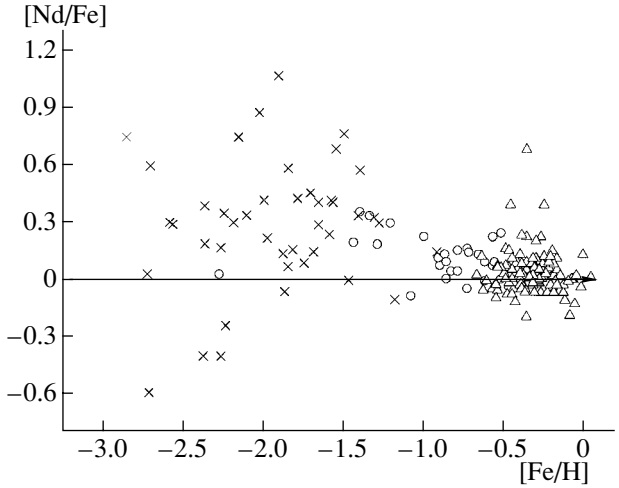

Fig. 5. [Nd/Fe] abundance ratios from various studies: Mishenina and Kovtyukh [24] (circles), Burris *et al.* [25] (crosses), and Reddy *et al.* [26] (triangles).

ear portion of the curve of growth throughout the relevant metallicity range. We therefore estimated the influence of uncertainties in the stellar parameters by performing test computations for one star, HD 97320 ($T_{\rm eff} = 6110$ K, $\log g = 4.27$, [Fe/H] $= -1.18$, $V_{\rm mic} = 1.4$ km/s). A temperature error of $\Delta T_{\rm eff} = 100$ K results in an abundance error of $\Delta \log \varepsilon_{\rm Nd} = 0.05$ dex, an error of $\Delta \log g = 0.1$ results in an error of $\Delta \log \varepsilon_{\rm Nd} = 0.04$ dex, and the effect of errors in $V_{\rm mic}$ is negligible (<0.01 dex). Note that we always analyzed the relative abundances [Nd/Fe], [Nd/Eu], and [Nd/Ba], and the abundances of all elements were determined using lines of the dominant ionization state, FeII, BaII, NdII, and EuII. In this case, the errors in the temperature and $\log g$ result in approximately equal errors in the abundances, while errors in $V_{\rm mic}$ affect the abundances of iron, neodymium, and europium comparably weakly due to the weakness of the lines studied. Thus, the errors of [Nd/Fe] and [Nd/Eu] due to uncertainty in the stellar parameters do not exceed 0.02–0.03 dex and are $\simeq 0.06$ dex for [Nd/Ba], since the errors in $V_{\rm mic}$ have a stronger effect on the stronger BaII lines.

Given the error in the iron abundances reported in [9, 15, 16], $\Delta \log \varepsilon_{\rm Fe} = 0.1$ dex, we estimate the total errors of the [Nd/Fe] abundance ratios (observational errors, uncertainties in the stellar parameters, and errors introduced by the analysis method) to be 0.15 dex.

As in our previous studies [13–15], our analysis takes into consideration the Galactic population to which each star belongs. Figure 4 shows the [Nd/Fe] ratios for the stars. When [Fe/H] < -1, neodymium is overabundant relative to iron, with the [Nd/Fe] ratios being between 0.23 and 0.45; stars of the thick disk and halo do not show different behavior in the interval of overlapping metallicities. When [Fe/H] > -1, this overabundance decreases with metallicity, and the corresponding metallicity-overabundance dependence is virtually the same for stars of the thick disk ([Nd/Fe] $= 0.08(\pm0.04) - 0.22(\pm0.05)$ [Fe/H]) and thin disk ([Nd/Fe] $= 0.01(\pm0.02) - 0.25(\pm0.07)$ [Fe/H]). The errors in the coefficients characterize the scatter for stars with similar metallicities. We can see in Fig. 4 that the scatter for [Fe/H] > -1 does not exceed the errors in the [Nd/Fe] ratios estimated above. The thick-disk star HD 3795 ([Fe/H] $= -0.64$) shows an anomalously high neodymium overabundance [Nd/Fe] $= 0.44$ compared to other stars of similar metallicity, as was found earlier for europium and barium [14]. We show below that the abundance ratios [Nd/Eu] and [Nd/Ba] for HD 3795 are typical of thick-disk stars, so that this strong overabundance relative to iron is most likely due to local inhomogeneity of the chemical composition of the interstellar gas.

Neodymium abundances have also been determined by other authors. We chose for comparison three recent papers whose authors analyzed extensive samples of cool stars with various metallicities based on high-resolution spectra. Figure 5 shows the results reported in [24–26]. When [Fe/H] < -1, the data of Mishenina and Kovtyukh [24] and Burris *et al.* [25] show, on average, an overabundance of neodymium relative to iron, but the scatter exceeds

an order of magnitude. When [Fe/H] > -1, no correlation is observed between [Nd/Fe] and metallicity due to the large scatter in the data, ~ 0.3 dex.

5. ANALYSIS OF RESULTS

We now analyze our neodymium abundances from the viewpoint of the chemical evolution of the Galaxy. Beginning with the work of Tinsley [27], it has been supposed that most iron in the Galaxy formed in type I supernova explosions (SN Ia), whose progenitors are stars with masses of $4-8M_\odot$. The overabundances of neoodymium relative to iron in halo and thick-disk stars conclusively demonstrate that the synthesis of neodymium in stars more massive than SN Ia progenitors during the epoch considered; i.e., the r-process in type II supernovae. The slope of the [Nd/Fe]–[Fe/H] relation when [Fe/H] > -1 indicates a higher production rate of iron compared to neodymium during the thick- and thin-disk epochs due to the onset of iron synthesis in type I supernovae.

The [Nd/Ba] and [Nd/Eu] ratios are sensitive to the relative contributions of the s and r-processes to the synthesis of these elements. Recall that, according to [2], $s : r = 56 : 44$ for solar neodymium, whereas this ratio is 81 : 19 and 6 : 94 for barium and europium, respectively. We adopted the barium and europium abundances from [13–15]. Given the errors in these abundances, $\Delta \log \varepsilon_{\rm Eu} = 0.1$ dex and $\Delta \log \varepsilon_{\rm Ba} = 0.1$ dex [13], the total error in the [Nd/Eu] and [Nd/Ba] abundance ratios can be estimated to be 0.15 dex, as in the case of [Nd/Fe]. Figures 6 and 7 show the observed abundance ratios.

Like [Nd/Fe], the [Nd/Ba] and [Nd/Eu] ratios show regular behavior as functions of metallicity. In halo and thick-disk stars, neodymium is overabundant relative to barium, with [Nd/Ba] being almost constant. The mean abundance ratio for eight halo stars is 0.34 ± 0.08 and coincides with the yield ratio of these elements for the r-process within the errors, $[\mathrm{Nd/Ba}]_r = 0.36$. The data for the thick-disk stars can be approximated by the dependence $[\mathrm{Nd/Ba}] = 0.28(\pm 0.03) - 0.01(\pm 0.04)\ [\mathrm{Fe/H}]$; i.e., they also indicate a virtually constant [Nd/Ba] abundance ratio, which is, however, 0.08 dex lower than the corresponding ratio for the r-process. In these same stars, neodymium is underabundant relative to europium. The mean abundance ratio for six halo stars is $[\mathrm{Nd/Eu}] = -0.27 \pm 0.05$, close to the yield ratio of these elements for the r-process, $[\mathrm{Nd/Eu}]_r = -0.33$ [2]. However, $[\mathrm{Nd/Eu}] \simeq 0$ for two stars, whereas their [Nd/Ba] ratios do not differ from those of the other halo stars. The neodymium abundance of one of these stars, HD 122196 ([Fe/H] $= -1.71$), can

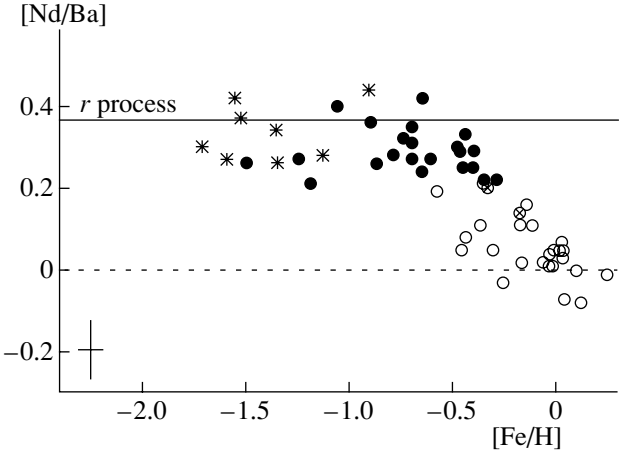

Fig. 6. Dependence of [Nd/Ba] on metallicity. The solid curve shows the ratio of element yields in the r-process, $[\mathrm{Nd/Ba}]_r = 0.36$. Notation is the same as in Fig. 4.

be confidently determined from two unblended lines: $[\mathrm{Nd/Fe}] = 0.20(\lambda 4446)$ and $0.25(\lambda 5320)$. However, this abundance is lower than the corresponding abundances in other stars with similar metallicities. This same star has already been reported to have an anomalously low europium abundance, with [Eu/Fe] $= 0.24$ [15]. It is necessary to determine the abundances of other elements in this star to understand whether the high [Nd/Eu] ratio is due to an error in the europium abundance or whether HD 122196 exhibits some peculiarities associated with its origin. The observed spectra of the second star, BD 18°3423 ([Fe/H] $= -0.90$), had a resolution of $\sim 40\,000$, and the abundance was determined from only one line at $\lambda 4232$. The anomalous [Nd/Eu] abundance ratio may be due to uncertainty in the abundances of both neodymium and europium. The same is true of the thick-disk star HD 201891 ([Fe/H] $= -1.05$); the only difference is that its Nd abundance was derived from the $\lambda 5320$ line. The [Nd/Eu] abundance ratio is higher for thick-disk stars than for halo stars and shows a weak trend: $[\mathrm{Nd/Eu}] = -0.13(\pm 0.03) + 0.05(\pm 0.04)\ [\mathrm{Fe/H}]$.

Both the [Nd/Ba] and [Nd/Eu] ratios in halo and thick-disk stars reflect the dominant contribution of the r-process in the synthesis of heavy elements during the formation of these stars and also indicate that the enrichment of the interstellar medium in nuclei synthesized in the s-process started prior to the onset of the formation of the thick disk: the [Nd/Eu] ratios in thick-disk stars are 0.15 ± 0.03 dex (when [Fe/H] ~ -1) and 0.18 ± 0.04 dex ([Fe/H] ~ -0.4) higher than predicted for the r-process, and the [Nd/Ba] ratio is, on average, lower by 0.08 ± 0.03 dex. The derived [Nd/Eu] ratios suggest that the s-process con-

Table 3. Elemental abundance ratios for stars rich in r-process elements

Star	[Fe/H]	[Ba/Fe]	[Nd/Fe]	[Eu/Fe]	[Eu/Ba]	[Nd/Eu]	[Nd/Ba]	Reference
CS 22892−52	−3.1	0.41?	−	1.70	1.29?	−	−	[29]
	−3.1	0.88	1.27	1.64	0.76	−0.37	0.39	[34]
	−3.04	0.93	1.19	1.44	0.51	−0.25	0.26	[6, 35]
average					0.64	−0.31	0.32	
CS 31082−01	−2.9	1.17	−	1.63	0.46	−	−	[29]
BD 17°3248	−2.1	0.40	−	0.91	0.51	−	−	[29]
	−2.02	0.97	0.88	0.96	−0.01	−0.08	−0.09	[25]
	−2.11	0.49	0.55	0.80	0.39	−0.25	0.06	[33]
	−2.0	0.25	0.43	0.78	0.53	−0.35	0.18	[32]
average					0.36	−0.23	0.05	
HD 126587	−2.85	−0.06	−	0.75	0.81	−	−	[29]
	−2.85	−0.06	0.75	0.75	0.81	−0.06	0.00	[25]
	−2.85	−0.27	−	0.37	0.64	−	−	[6]
	−3.08	−0.13	0.21	0.42	0.55	−0.21	0.34	[33]
average					0.67	−0.14	0.17	
HD 115444	−3.0	0.18	−	0.85	0.67	−	−	[29]
	−2.99	0.18	0.56	0.85	0.67	−0.29	0.38	[36]
	−2.77	−0.05	−	0.65	0.70	−	−	[25]
	−3.16	−0.07	0.30	0.83	0.90	−0.53	0.37	[33]
average					0.76	−0.41	0.38	
HD 20	−1.39	0.58	−	0.77	0.19	−	−	[29]
	−1.39	0.58	0.58	0.77	0.19	−0.22	0.00	[25]
average over five stars (without HD 20)					0.58	−0.27	0.23	
r-process					0.70	−0.33	0.36	[2]

tributed ∼30% of the synthesized neodymium during the formation of the thick disk. We reached a similar conclusion in [13–15] based on our analysis of [Eu/Ba] ratios and isotopic ratios for barium and estimated the contribution of the s-process to barium in thick-disk stars to be 30–50%.

All our conclusions about the relative contributions of the s- and r-processes are based on comparisons of the observed elemental abundances and theoretical predictions for the r process. Modeling of the chemical evolution of the Galaxy is a multiparameter problem, raising the question of how accurate the predictions are. Ratios of elemental yields for the r-process can be estimated by analyzing the abundances of these elements in stars that are rich in r-process elements. The first such star, CS 22892–052, was discovered by Sneden *et al.* [28] in 1994. In this star, the overabundances of europium, samarium, hadolinium, and other heavy elements relative to iron exceed one and a half orders of magnitude. In their review, Truran *et al.* [29] present a list of six such stars. Sneden *et al.* [30] and then others (see [29] for

references) were the first to establish that the relative abundances of elements with $Z \geq 56$ (but with $Z < 70$, as was later found by Hill *et al.* [31]) in these stars correspond to the distribution of the contributions of the r-process to the solar abundances of these elements. Each of these stars probably formed near a type II supernova that enriched the interstellar gas in r-process elements. If there is also some contribution of the s-process in such stars, it is small compared to the contribution of the r process, and the heavy-element abundance ratios should reflect the elemental yield ratios for the r-process.

We collected published abundances of the elements studied here in six stars from the list of Truran *et al.* [29], listed in Table 3. For each star, we calculated the mean abundance ratios [Eu/Ba], [Nd/Eu], and [Nd/Ba] based on the data of various authors and the values averaged over all the stars. The [Ba/Fe] ratio for CS 22892–052 reported in [29] appears to be a typographical error, since it is inconsistent with the figure shown in that same paper. In Table 3, this value is presented with a question mark, as is the [Eu/Ba] value derived from it. We did not include the data from [29] when determining the mean abundance ratios for CS22892–052. Truran *et al.* [29] appear to have adopted the results of Burris *et al.* [25] for HD 20 and HD 126587 and the results of Westin *et al.* [36] for HD 115444, since the data are identical. We did not use these additional identical values when computing the means. The results of different authors differ by more than 0.5 dex; e.g., the ratios [Ba/Fe] = 0.97 and [Ba/Fe] = 0.25 are reported for BD 17°3248 in [25] and [32], respectively. This is due to the weakness of the lines studied; all the stars except HD 20 have [Fe/H] < -2. We did not include the results for HD 20 when determining the values averaged over all the stars, since the only available data for this star are those published in [25], but, as is evident from Table 3, these results differ strongly from those for other studies, making the very classification of this star as being rich in r-process elements open to question. The accuracy of the mean abundance ratios is fairly low: the [Eu/Ba], [Nd/Eu], and [Nd/Ba] ratios vary between 0.36 and 0.76, -0.14 and -0.41, and 0.05 and 0.38, respectively, for different stars. Therefore, we can conclude only that the theoretical abundance ratios for r-process elements do not contradict the results for stars rich in r-process elements.

Although we have analyzed here only halo stars with moderate metal deficiencies ([Fe/H] between -1.71 and -0.90), our results can be used to impose additional observational constraints on the elemental yield ratios for the r-process: theoretical ratios for the r-process based on the data of Arlandini *et al.* [2] agree with the mean observed values of [Nd/Ba] = 0.34 ± 0.08 and [Nd/Eu] = -0.27 ± 0.05 within the errors.

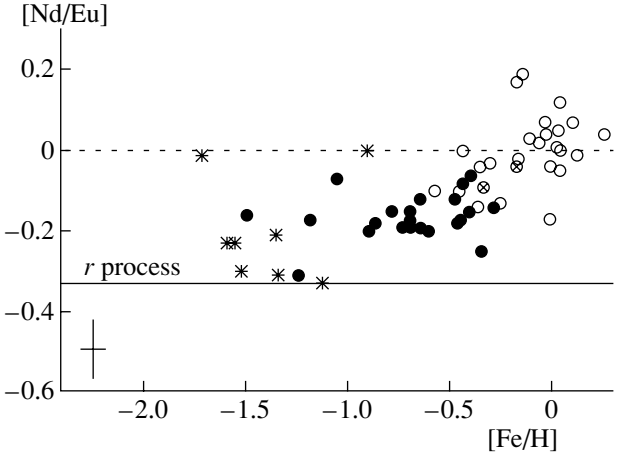

Fig. 7. Dependence of [Nd/Eu] on metallicity. The solid curve shows the ratio of element yields in the r-process, $[\mathrm{Nd/Eu}]_r = -0.33$. Notation is the same as in Fig. 4.

The behavior of [Nd/Ba] changes in the transition from the thick to the thin disk. Thick-disk stars display the trend [Nd/Ba] = $0.03(\pm 0.01) - 0.19(\pm 0.06)$ [Fe/H]. In the interval of overlapping metallicities (from -0.57 to -0.28), the [Nd/Ba] ratio is, on average, 0.17 dex lower for thin-disk stars than for thick-disk stars. Although the difference is within 2σ, we discovered earlier [13–15] a similar jumplike variation (by 0.25 dex) for the [Eu/Ba] ratio in the transition from the thick to the thin disk.

The [Nd/Eu] ratio in thin-disk stars increases with metallicity: [Nd/Eu] = $0.03(\pm 0.02) + 0.19(\pm 0.08)$ [Fe/H]. Thick- and thin-disk stars do not show any appreciable differences in the interval of overlapping metallicities. The decrease in [Nd/Ba] and increase in [Nd/Eu] are due to the higher s-process synthesis rate of barium compared to neodymium and of neodymium compared to europium.

6. CONCLUSIONS

The neodymium abundances that we have derived for a representative sample of cool stars with metallicities [Fe/H] ranging from 0.25 to -1.71 reflect the different roles played by the r and s processes in the synthesis of heavy elements during the formation of various Galactic populations—the halo, thick disk, and thin disk—and confirm earlier conclusions based on analyses of the [Eu/Ba] abundance ratios and isotopic ratios for barium [15].

(1) During the formation of the halo, the synthesis of barium was dominated by the r-process: the [Nd/Ba] and [Nd/Eu] ratios in halo stars coincide

with the elemental yield ratios for the r-process within the errors.

(2) The enrichment of the interstellar medium in s-process nuclei began before the beginning of the formation of the thick disk. The s-process contributed $\simeq 30\%$ of the neodymium produced during the thick-disk epoch.

(3) The systematic decrease of the [Nd/Fe] ratios for thick-disk stars with increasing metallicity testifies to the onset of the efficient production of iron in type I supernovae.

(4) As in the case of the [Eu/Ba], [Eu/Fe] [14], and [Mg/Fe] ratios [9], the [Nd/Fe], [Nd/Ba], and [Nd/Eu] ratios for the thick disk are characterized by a small scatter for stars with similar metallicities, demonstrating that the mixing of matter was complete during this stage in the evolution of the Galaxy.

(5) We find tentative evidence that the [Nd/Ba] abundance ratio decreases abruptly by 0.17 dex in the transition from the thick to the thin disk. This reflects the existence of an intermediate phase before the onset of the formation of the thin disk, when the production of r-process nuclei of heavy elements (i.e., nucleosynthesis in type II supernovae) had ceased, while evolving stars with masses $2-4M_{\odot}$ continued to enrich the interstellar gas in s-process nuclei, with the enrichment rate being higher for barium than for neodymium. The solar neodymium was produced in approximately equal amounts in the r and s-processes, indicating that the total change in the [Nd/Ba] and [Nd/Eu] ratios over the history of the Galaxy are 0.36 dex and 0.33 dex, respectively—much smaller than the change in the [Eu/Ba] ratio. Therefore, evolutionary patterns are much less prominent in the behavior of the [Nd/Ba] and [Nd/Eu] ratios, and the observed effects are at a marginally detectable level.

(6) The s-process dominated in the synthesis of heavy elements during the thin-disk epoch. Since this process requires seed nuclei of iron-group elements (i.e., it is secondary by nature), the yield of the s-process increases with metallicity. The systematic decrease of [Nd/Ba] and increase of [Nd/Eu] with metallicity in the thin-disk stars confirm our concepts about the synthesis of chemical elements.

ACKNOWLEDGMENTS

We are sincerely grateful to K. Fuhrmann and T. Gehren for sharing their spectroscopic observations made with the 2.2-m telescope at the German–Spanish Astronomical Center in Calar Alto (Spain), to A. Korn for providing his Windows version of the SIU program, to T.A. Ryabchikova for assistance in collecting the atomic data for NdII, and to A. Chernova for assistance with this research. This work was partially supported by the Russian Foundation for Basic Research (project code 02-02-17174) and the President of the Russian Federation Program for the Support of Leading Scientific Schools (grant NSh-1789.2003.02).

REFERENCES

1. F. Käppeler, H. Beer, and K. Wisshak, Rep. Prog. Phys. **52**, 945 (1989).
2. C. Arlandini, F. Käppeler, K. Wisshak, *et al.*, Astrophys. J. **525**, 886 (1999).
3. M. Spite and F. Spite, Astron. Astrophys. **67**, 23 (1978).
4. J. W. Truran, Astron. Astrophys. **97**, 391 (1981).
5. K. K. Gilroy, C. Sneden, C. A. Pilachowski, and J. J. Cowan, Astrophys. J. **327**, 298 (1988).
6. A. McWilliam, Astron. J. **115**, 1640 (1998).
7. R. G. Gratton, E. Carretta, F. Matteucci, and C. Sneden, in *Formation of the Galactic Halo, Inside and Out* (Astron. Soc. Pacific, San Francisco, 1996), ASP Conf. Ser. **92**, 307 (1996).
8. R. G. Gratton, E. Carretta, F. Matteucci, and C. Sneden, Astron. Astrophys. **358**, 671 (2000).
9. K. Fuhrmann, Astron. Astrophys. **338**, 161 (1998).
10. J. X. Prochaska, S. O. Naumov, B. W. Carney, *et al.*, Astron. J. **120**, 2513 (2000).
11. S. Feltzing, T. Bensby, and I. Lundström, Astron. Astrophys. **397**, L1 (2003).
12. J. Bernkopf, A. Fiedler, and K. Fuhrmann, in *Astrophysical Ages and Time Scales* (Astron. Soc. Pacific, San Francisco, 2001), ASP Conf. Ser. **245**, 207 (2001).
13. L. Mashonkina and T. Gehren, Astron. Astrophys. **364**, 249 (2000).
14. L. Mashonkina and T. Gehren, Astron. Astrophys. **376**, 232 (2001).
15. L. Mashonkina, T. Gehren, C. Travaglio, and T. Borkova, Astron. Astrophys. **397**, 275 (2003).
16. K. Fuhrmann, Astron. Nachr. (2003, in press).
17. K. Fuhrmann, M. Pfeiffer, C. Frank, *et al.*, Astron. Astrophys. **323**, 909 (1997).
18. R. L. Kurucz, CD-ROMs Nos. 18, 19 (1994).
19. N. Grevesse, A. Noels, and A. J. Sauval, in *Proc. of the 6th Annual October Astrophysics Conference in College Park, Maryland* (Astron. Soc. Pacific, San Francisco, 1996), ASP Conf. Ser. **99**, 117 (1996).
20. F. Kupka, N. Piskunov, T. A. Ryabchikova, *et al.*, Astron. Astrophys., Suppl. Ser. **138**, 119 (1999).
21. R. L. Kurucz, I. Furenlid, J. Brault, and L. Testerman, *Solar Flux Atlas from 296 to 1300 nm* (Nat. Solar Obs., Sunspot, New Mexico, 1984).
22. W. H. King, A. Steudel, and M. Wilson, Z. Phys. **265**, 207 (1973).
23. M. Pfeiffer, C. Frank, D. Baumüller, *et al.*, Astron. Astrophys., Suppl. Ser. **130**, 381 (1998).
24. T. Mishenina and V. V. Kovtyukh, Astron. Astrophys. **370**, 951 (2001).

25. D. L. Burris, C. A. Pilachowski, T. E. Armandroff, *et al.*, Astrophys. J. **544**, 302 (2000).
26. B. E. Reddy, J. Tomkin, D. L. Lambert, and C. Allende Prieto, Mon. Not. R. Astron. Soc. **340**, 304 (2003).
27. B. M. Tinsley, Astrophys. J. **229**, 1046 (1979).
28. C. Sneden, G. W. Preston, A. McWilliam, and L. Searle, Astrophys. J. **431**, L27 (1994).
29. J. W. Truran, J. J. Cowan, C. A. Pilachowski, and C. Sneden, Publ. Astron. Soc. Pac. **114**, 1293 (2002).
30. C. Sneden, A. McWilliam, G. W. Preston, *et al.*, Astrophys. J. **467**, 819 (1996).
31. V. Hill, B. Plez, R. Cayrel, *et al.*, Astron. Astrophys. **387**, 560 (2002).
32. J. J. Cowan, C. Sneden, S. Burles, *et al.*, Astrophys. J. **572**, 861 (2002).
33. J. A. Johnson and M. Bolte, Astrophys. J. **554**, 888 (2001).
34. C. Sneden, J. Johnson, R. P. Kraft, *et al.*, Astrophys. J. **536**, L85 (2000).
35. A. McWilliam, G. W. Preston, C. Sneden, and L. Searle, Astron. J. **109**, 2757 (1995).
36. J. Westin, C. Sneden, B. Gustafsson, and J. J. Cowan, Astrophys. J. **530**, 783 (2000).

Translated by A. Dambis

Astronomy Reports, Vol. 48, No. 3, 2004, pp. 200–209. Translated from Astronomicheskiĭ Zhurnal, Vol. 81, No. 3, 2004, pp. 224–233.

Long-Term Monitoring of the Water-Vapor Maser in NGC 7538: 1993–2003

E. E. Lekht[1,2], V. A. Munitsyn[3], and A. M. Tolmachev[4]

[1] *Instituto Nacional de Astrofísica, Óptica y Electrónica, Luis Enrique Erro No. 1, Apdo Postal 51 y 216, 72840 Tonantzintla, Puebla, México*

[2] *Sternberg Astronomical Institute, Universitetskiĭ pr. 13, Moscow, 119992 Russia*

[3] *Space Research Institute, Moscow, Russia*

[4] *Pushchino Radio Astronomy Observatory, Astro Space Center, Lebedev Physical Institute, Russian Academy of Sciences, Pushchino, Moscow oblast, 142290 Russia*

Received March 15, 2003; in final form, September 18, 2003

Abstract—The paper presents the results of monitoring the H_2O maser in NGC 7538, which is associated with a star-formation region, in 1993–2003. The observations were carried out on the 22-m radio telescope of the Pushchino Radio Astronomy Observatory (Russia). The variability of the maser emission displays a cyclic character. Two cycles of the long-term variability of the total flux were detected over the entire monitoring period (1981–2003): 1981–1993 and 1994–2003. The period of the variability is about 13 years. An anticorrelation of the emission in lateral sections of the spectra is observed, as is characteristic of protoplanetary disks. A drift in the radial velocity of the central component is observed ($V_{LSR} = -60$ km/s) with a drift rate of about 0.09 km/s per year. The water-vapor maser is most likely associated with a protoplanetary disk. © *2004 MAIK "Nauka/Interperiodica".*

1. INTRODUCTION

NGC 7538 is a complex region in the Perseus arm of the Galaxy. It is associated primarily with a molecular-cloud complex and a visible HII region. NGC 7538 contains 11 infrared sources, three of which—IRS 1, IRS 2, and IRS 3—form a dense cluster [1]. The core of the molecular-hydrogen cloud contains sites of star formation [2], which are associated with high-velocity gas flows and supercompact HII regions.

The region associated with IRS 1 is of considerable interest. It has a peculiar morphology, with a high-velocity flow of molecular CO [3–5] and ionized gas [6] and a disk that is rotating around IRS 1 [6]. VLBI observations of the H_2O maser in NGC 7538 were conducted in May 1987 by Kameya *et al.* [7], who discovered that the maser spots formed two groups. One group is very compact and projected onto a supercompact HII region [8], which is the source of excitation of the maser radiation. The maser spots in the second group are scattered over a region $24'' \times 15''$ in size. The appreciable differences in the distributions of the maser spots in these two groups of spots associated with IRS 1 probably implies different pumping mechanisms for the two groups.

High-spatial-resolution 1.35 cm continuum and H66α radio recombination line observations of IRS 1 show that the core of the HII region contains numerous clumps with brightness temperatures $\approx 1.5 \times 10^4$ K [9]. The continuum core contains a northern and southern component with a region of enhanced electron density between them. It is supposed that the exciting star is located at the center of this region. There is a north–south outflow of ionized gas from the core of the HII region.

Monitoring in the 1.35 cm water-vapor line carried out in 1981–1992 showed the presence of cyclic activity of the IRS 1 maser in NGC 7538 [10] with an estimated period of 13–14 yrs. The emission features display a tendency to form separate groups in the spectrum. The detection of correlations and anticorrelations of the emission of various components testifies that a large number of the emission features (maser spots) have a common center of excitation. Long-term monitoring also enabled the detection of a large number of components that were manifest as maser sources only during some time intervals.

We present here the results of monitoring in 1993–2003, during the second cycle of the water-vapor master activity associated with IRS 1 in the NGC 7538 complex.

2. OBSERVATIONS AND DATA

Our observations of the IRS 1 1.35 cm H_2O maser in the NGC 7538 complex ($\alpha_{1950} = 23^h11^m36.5^s$,

1063-7729/04/4803-0200$26.00

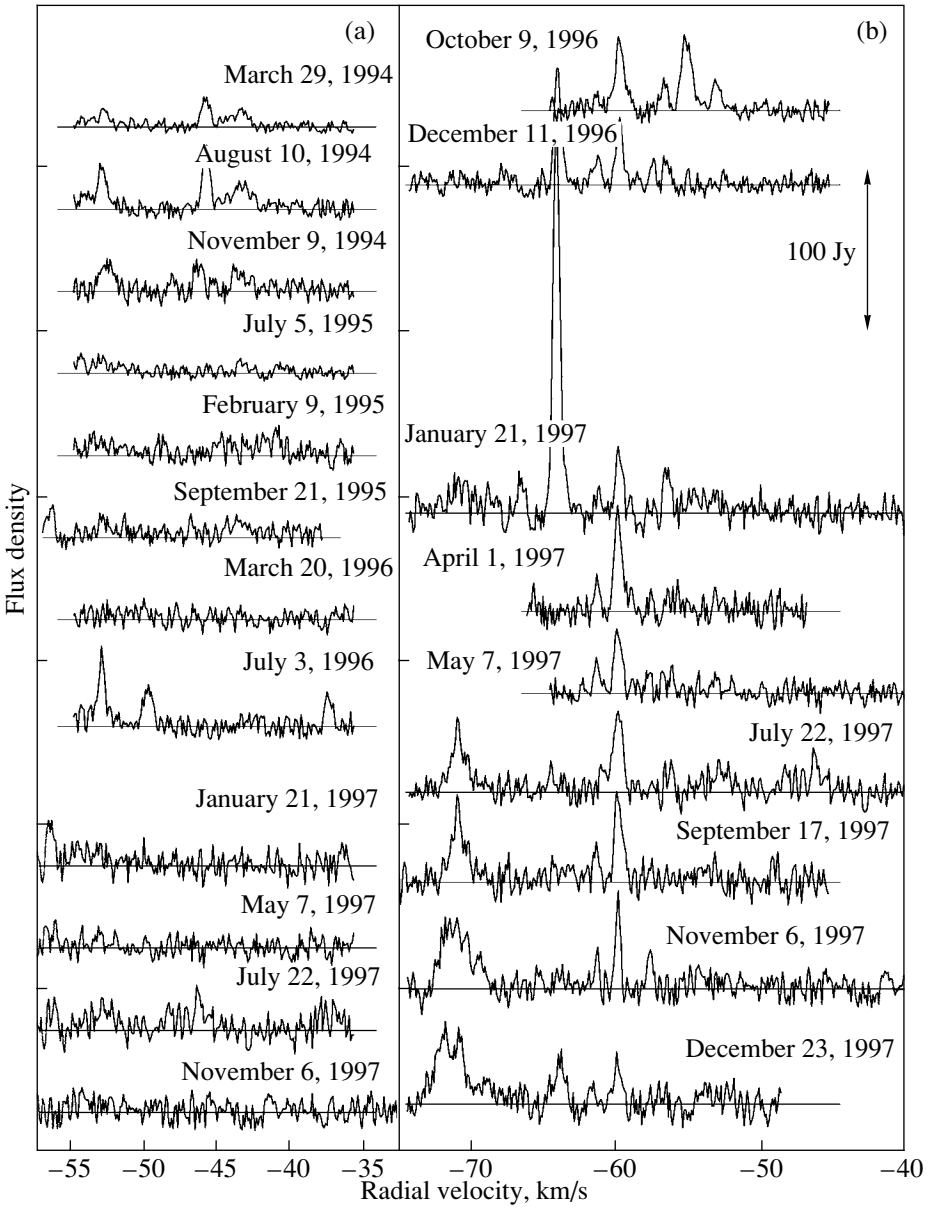

Fig. 1. H_2O maser spectra for NGC 7538 obtained in 1993–2003. The vertical arrow shows the scale for the large divisions.

$\delta_{1950} = 61°11'49''$) were carried out on the fully steerable parabolic 22-m radio telescope of the Pushchino Radio Astronomy Observatory from 1993–2003. The mean interval between observations was about two months. For a point source of unpolarized radiation, an antenna temperature of 1 K corresponds to a flux density of 25 Jy (see, for example, [11]).

The receiver used during the monitoring NGC 7538 included a liquid-helium-cooled 22-GHz transistor amplifier. The system noise temperatures were 150–200 K. A new input amplifier was installed in autumn 2000, which decreased the system noise temperatures to 100–150 K [12]. The antenna beam width at 22 GHz is 2.6′. The signal was analyzed using a 128-channel filter spectrometer with a frequency resolution of 7.5 kHz (0.101 km/s in radial velocity at the 1.35 cm line).

Figure 1 presents the results of our observations of the NGC 7538 water maser in 1993–2003. The vertical arrow shows the scale for the large divisions in Jy. The horizontal axis plots the radial velocity relative to the Local Standard of Rest (LSR). Due to the large variations of the signal, the plots have been made with different vertical scales. The four lower spectra in Fig. 1a represent a continuation of the spectrum toward the more positive velocities corresponding to the spectra of Fig. 1b.

Figure 2a depicts the variability of the total flux of

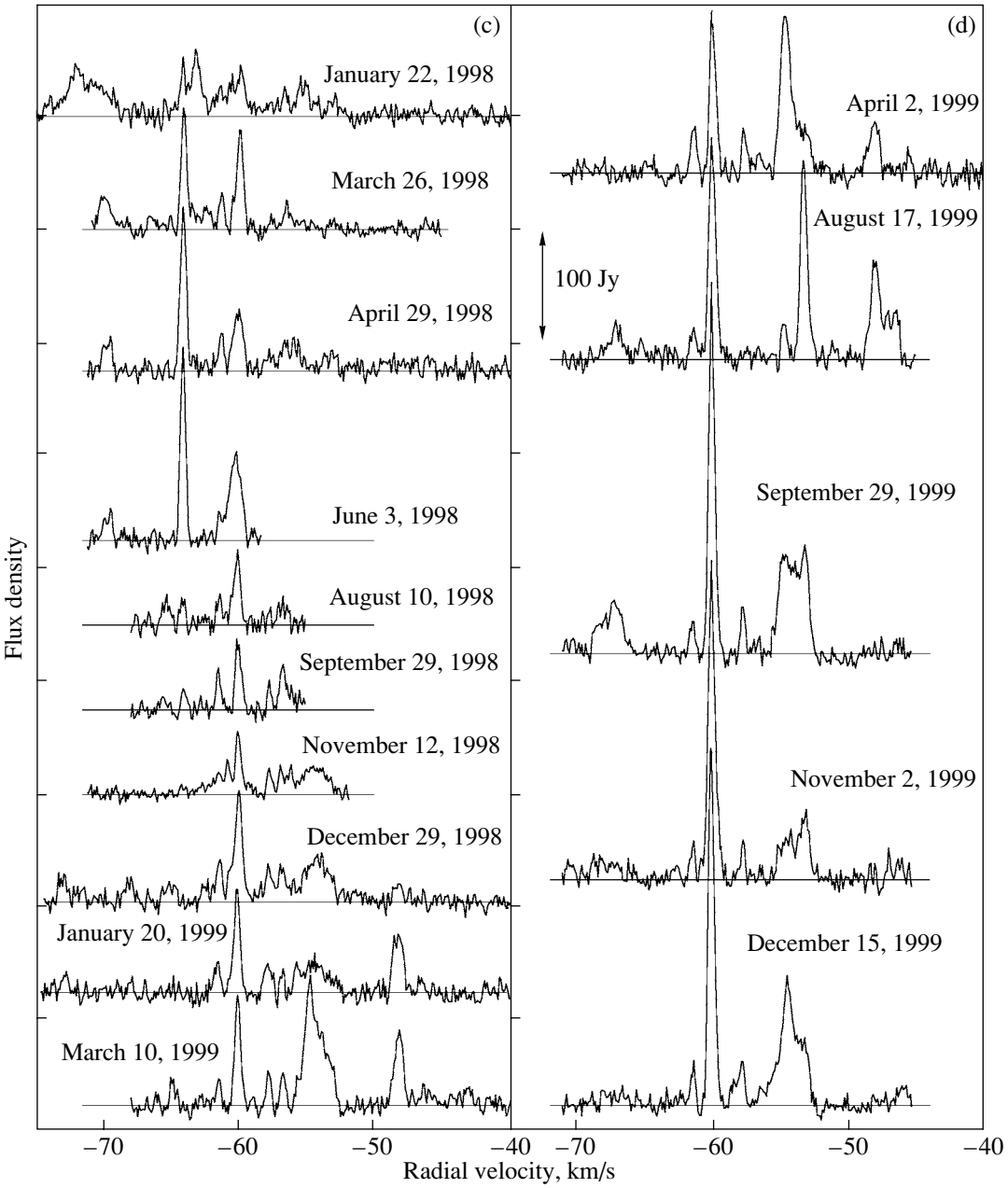

Fig. 1. (Contd.)

the entire spectrum. The numbers above some maxima indicate the velocities of features whose emission was appreciable at the given epoch. In addition, a velocity centroid (mean weighted radial velocity) for the maser emission was calculated for each spectrum (Fig. 2b). We also include the results of our first monitoring interval, 1981–1992. Substantial velocity jumps are observed, which, as earlier (1981–1992), are due to the appearance or disappearance of the emission of individual features or groups of features. The dashed and dot–dashed horizontal lines indicate the most preferred values for the velocity centroid.

Our analysis of the monitoring results shows that the H_2O spectra can undergo appreciable structural variations at some epochs, with individual groups of emission features appearing or disappearing. We accordingly made a superposition of the spectra for various time intervals in 1996–2003, shown in Fig. 3 together with the corresponding mean spectra. The data obtained before 1996 are not included, since the observations made during the period of minimum maser activity were irregular and did not cover the full range of radial velocities. A superposition of spectra

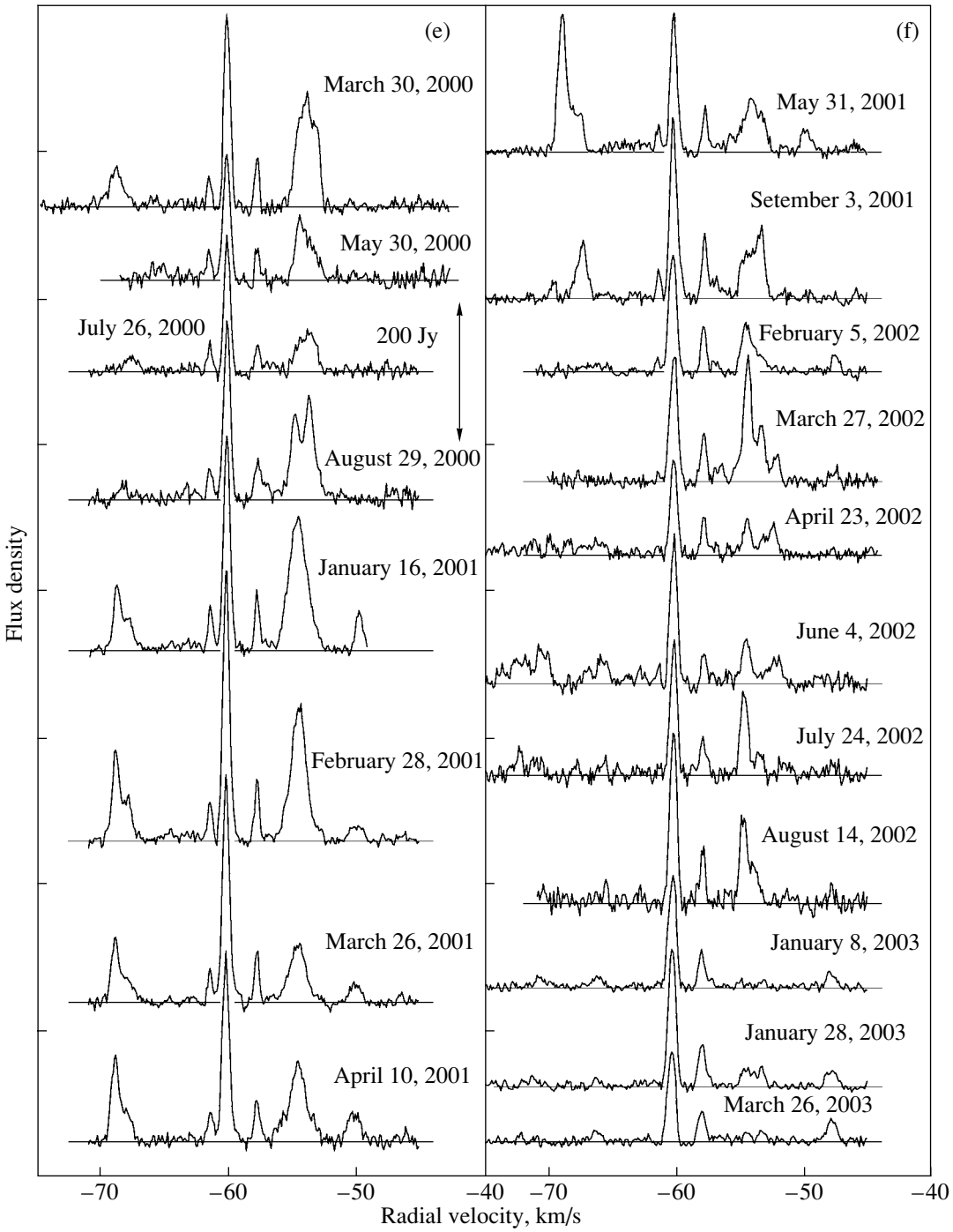

Fig. 1. (Contd.)

for the entire interval 1996–2003 is shown to the upper right.

The presence of deep minima in the superposition of all the spectra (right to zero in seven of nine cases) is striking. This indicates that there was absolutely no emission at certain radial velocities in 1996–2003. We adopted these values of V_{LSR} as boundaries for dividing the spectra into separate intervals, for each of which we calculated integrated fluxes.

Figure 4 presents curves that displayed anticorrelations in their integrated fluxes. Each plot gives flux-variability curves for two spectral intervals. For ease of comparison, these plots, including the last, are presented on different scales. The solid curves correspond to the scales on the left. The numeration

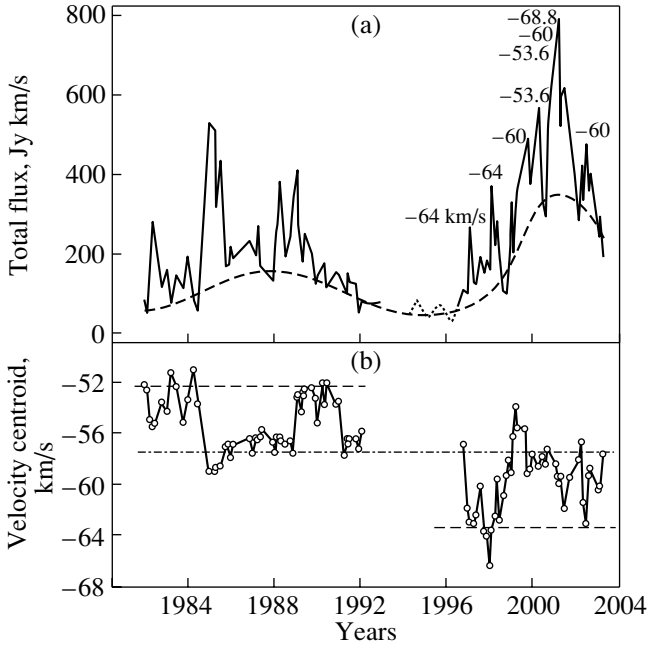

Fig. 2. Variability of the (a) total flux and (b) velocity centroid of the H_2O maser emission. The radial velocities of features during flares are indicated.

of the curves is in accordance with the table. The table also presents the maximum integrated fluxes for 1996–2003 and the maximum flux densities, obtained by dividing the maximum value by the corresponding spectral interval.

3. ANALYSIS OF THE MONITORING RESULTS

We concentrate here on the variability of the total H_2O flux, velocity centroid, and individual groups of features consisting of spectrally close components.

3.1. Long-period and Flare Activity

Our monitoring of the H_2O maser in NGC 7538 showed that the total-flux variability displays a cyclic character (Fig. 2a). Our observations cover two cycles of the long-period variability, which has a period of about 13 yrs: 1981–1993 and 1994–2003. As we noted in our earlier study [10], the influence of the southern source associated with IRS 11 on the total flux is small, as is confirmed by our observations toward both sources in 2003. Consequently, the cyclic variability is associated with the compact group of maser spots near IRS 1 [7].

The interval 1992–1996 (the first half) is a time of relatively low H_2O maser activity. The mean total flux was ~50 Jy km/s. The total flux at the maximum (the beginning of 2001) reached nearly 800 Jy km/s.

There are a number of appreciable differences between the two cycles of the maser activity, as is indicated below.

1. The emission in the second activity cycle was more intense than in the first. This is true not only of the total flux and of the flux of the main component at $V_{LSR} \approx -60$ km/s but also of other components, such as those at −64.5 and −54.5 km/s.

2. The mean values of the velocity centroids for the first and second activity cycles were −55 and −60 km/s, respectively.

The total-flux variability curve displays several deep minima. We took this into account when obtaining a polynomial fit for this curve (dashed curve in Fig. 2a). We also slightly corrected the curve for the first cycle presented in [10] to take into account the variability displayed in the second cycle. The resulting curve reflects the long-period variations of the total flux. All emission above this curve represents the numerous flares that occurred in the period covered by our monitoring, 1981–2003.

The observation of two cycles of maser activity in IRS 1 in NGC 7538 supports the results of theoretical studies indicating that the luminosity of a newly formed star can display variations with a period of about 5–10 yrs during early stages of its evolution (see, for example, [13, 14]).

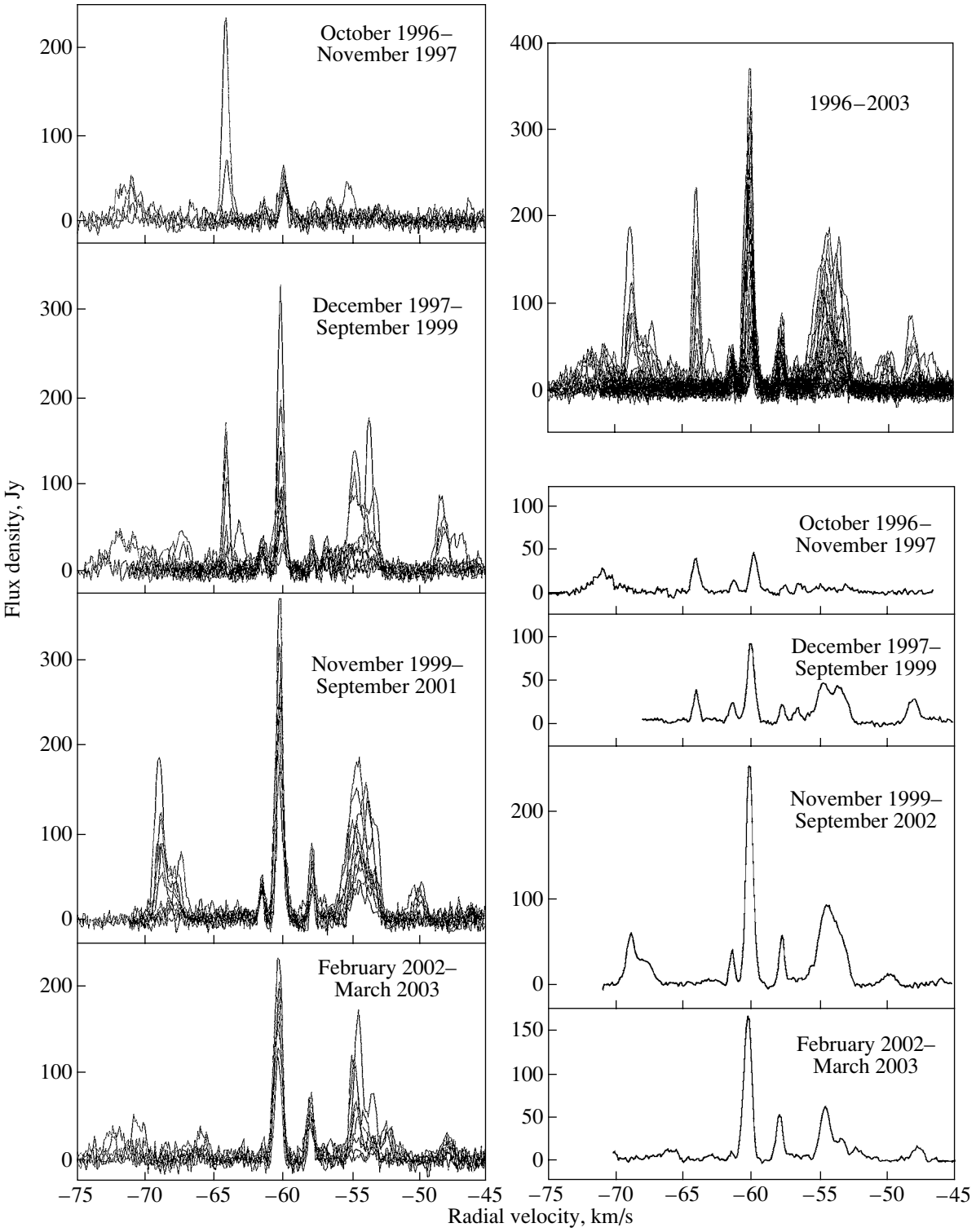

Fig. 3. Superposition of spectra for various time intervals and for the entire interval from 1996–2003. Mean spectra for the corresponding time intervals are shown to the right. All the plots are shown using the same scale.

3.2. Velocity Centroid

The main characteristic feature of the variability of the velocity centroid for the H_2O spectra is the presence of substantial jumps by 4–6 km/s, which were observed throughout the entire monitoring interval, 1981–2003. These velocity jumps were due

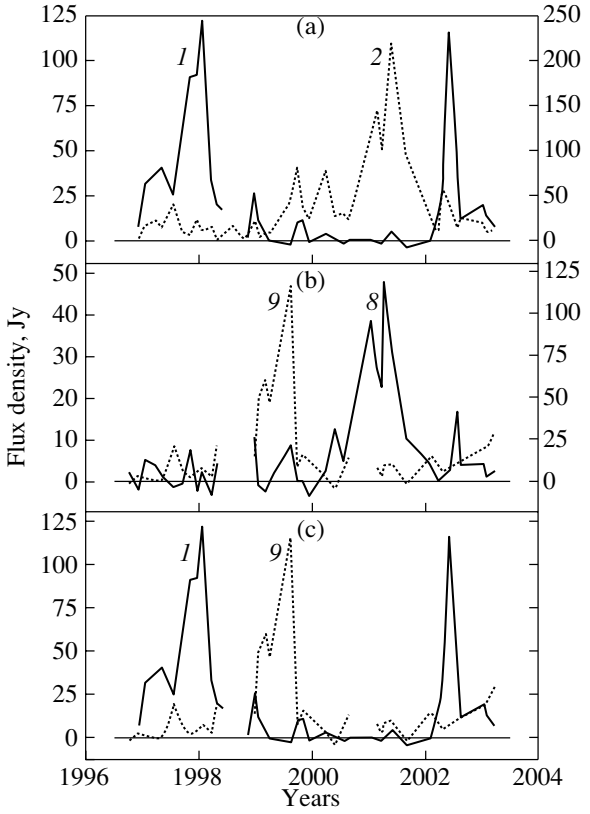

Fig. 4. Variability of the integrated fluxes for various sections of the H_2O spectrum. For ease of comparison, the plots of the flux variability for the two intervals shown in each panel, including the last, are given on different scales. The solid curves correspond to the scales indicated to the left. The numeration of the curves is in accordance with the numbers for the spectral intervals in the table.

primarily to the appearance or disappearance of the emission of individual groups of features with close radial velocities. The integrated fluxes for the spectral intervals $-(74-69.7)$ and $-(49.2-45.9)$ km/s displayed a significant anticorrelation in 1996–2003.

We can distinguish three predominant values for the velocity centroid: -52.3, -57.5, and -63.5 km/s. The first two values dominate in 1981–1992, while the last two values dominate in 1996–2003. This property of the variability indicates that emission at $V_{LSR} < -65$ km/s appeared during the second cycle of maser activity, which shifted the mean value of the velocity centroid (from -55 to -60 km/s).

3.3. Correlations and Anticorrelations of the Fluxes

A superposition of all the H_2O spectra (Fig. 3) shows that, in 1996–2003, emission was observed at radial velocities from -76 to -46 km/s. Another characteristic of the emission is the presence of isolated, long-living features in the central part of

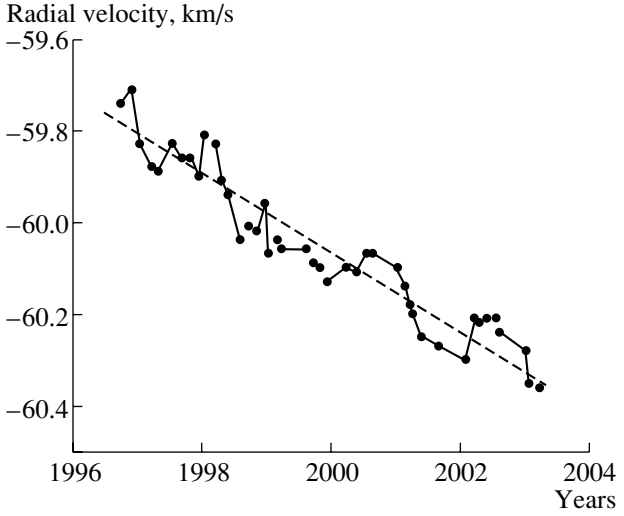

Fig. 5. Variability of the radial velocity of the central component in the H_2O spectrum.

the spectrum. The strongest emission is at $V_{LSR} \approx -60.2$ km/s, which is not precisely at the center of the spectrum. The data presented in the table support this result. As was shown by Lekht *et al.* [15], the variations of the fluxes of the central features at -64.5, -61, -60, and -58 km/s were correlated, with the largest delay between the corresponding maxima being no more than 0.3 yrs.

Groups of spectrally close features are located on either side of the central features. The emission of these lateral features sometimes reached 200 Jy. Analysis of this emission revealed an anticorrelation between the integrated fluxes of the groups of features located at the edges of the spectra. Figure 4 presents comparisons of the variations in spectral intervals 1, 2, 8, and 9 (see the table), which can be seen to be anticorrelated. It is likely that the emission in intervals 1 and 9 was strongly suppressed when emission was present in intervals 2 and 8. The strongest anticorrelation is observed for the fluxes in intervals 1 and 9 (Fig. 4c). Note that there was no emission from intervals 1 and 9 during the absolute maximum of the total flux in 2000–2001.

3.4. Models for the H_2O Maser in IRS 1 in NGC 7538

The observed anticorrelations in the emission of NGC 7538 at close radial velocities (spectral intervals 1 and 2, 8 and 9) could come about if the maser spots are distributed in a compact formation in an expanding shell. We are dealing with another situation with the anticorrelation between the fluxes in spectral intervals 1 and 9. The velocity difference between the centers of these intervals reaches 25 km/s. In order

Main characteristics of individual intervals of the H_2O spectrum of NGC 7538

Interval number	Range of V_{LSR}, km/s		Maximum integrated flux, Jy km/s	Flux density at maximum, Jy
1	−74	−69.7	120	28
2	−69.7	−64.8	220	45
3	−64.8	−62	145	52
4	−62	−61.1	30	33
5	−61.1	−58.8	240	104
6	−58.8	−57.2	52	32
7	−57.4	−52.2	330	66
8	−52.2	−49.2	120	40
9	−49.2	−45.9	47	14

for an anticorrelation to be observed, there must be an absence of relative motion of the molecules in the corresponding maser spots. This is possible for spectral intervals 1 and 9 if the spots are associated with a Keplerian (protoplanetary) disk.

The radial-velocity drift of the central feature at −60 km/s (Fig. 5) may represent important evidence in support of a Keplerian-disk model. The drift rate is modest—$\Delta V/\Delta t = 0.087$ km/s per year. Unfortunately, it is not possible to calculate the main parameters of the Keplerian disk purely on the basis of this information.

As was shown by Lekht *et al.* [16], in the case of a partially saturated maser in an inhomogeneous Keplerian disk, there can be anticorrelations not only between the fluxes of the lateral components of triplet spectra [17] but also between the lateral and central components. An important property of the H_2O maser associated with IRS 1 in NGC 7538 is that it displays anticorrelations both between the fluxes of the lateral components and between the fluxes in the lateral components themselves at similar radial velocities (spectral intervals 1 and 2, 8 and 9).

In a Keplerian-disk model, the maser spots that are responsible for spectral intervals 1 and 2 (the blue component) could be located at one edge of a disk viewed edge-on, while the features in intervals 8 and 9 (the red component) are located at the opposite edge. A simple schematic of such a model is shown in Fig. 6. For simplicity, each group of features in a spectral intervals is represented as a single feature with the corresponding numbers. The position of the protoplanetary disk relative to the northern and southern components of the core of the supercompact HII region [9] are indicated in accordance with the coordinates of the H_2O maser obtained by Migenes *et al.* [18]. The star is located between the northern and southern components of the core of the HII region [9].

In addition, we can also suppose that the maser spots responsible for the emission in intervals 2 and 8 are not located in the plane of the sky but at some angle to this plane. In this case, if they have the same orbital velocities, the radial velocities of features 2 and 8 will be lower than those of features 1 and 9, with an absence of relative motion between the maser spots.

In this type of model, the informational connection between the components could be realized by chord modes of the radiation [16] forming a continuous ring of maser activity, or a maser "ring." There will be a competition between pumping modes in such a maser ring if it is partially saturated. In this case, any variation in the radiation intensity of one of the modes will be transported around the ring and be reflected in the intensities of all the other modes. In principle, this could give rise to either correlations or anticorrelations of the emission of various features [16].

4. MAIN RESULTS

Let us summarize the main results of our monitoring of NGC 7538 using the 22-m radio telescope of the Pushchino Radio Astronomy Observatory.

(1) We have presented a catalog of H_2O maser spectra for the direction of IRS 1 in NGC 7538 obtained in 1993–2003.

(2) The variations of the maser emission display a cyclic character. Two cycles of the long-term variability of the total flux, estimated to have a period of 13 yrs, were observed over the entire monitoring interval (1981–2003): 1981–1993 and 1994–2003. We predict that the next minimum of the H_2O-maser activity will occur in 2005–2006. This cyclicity in the

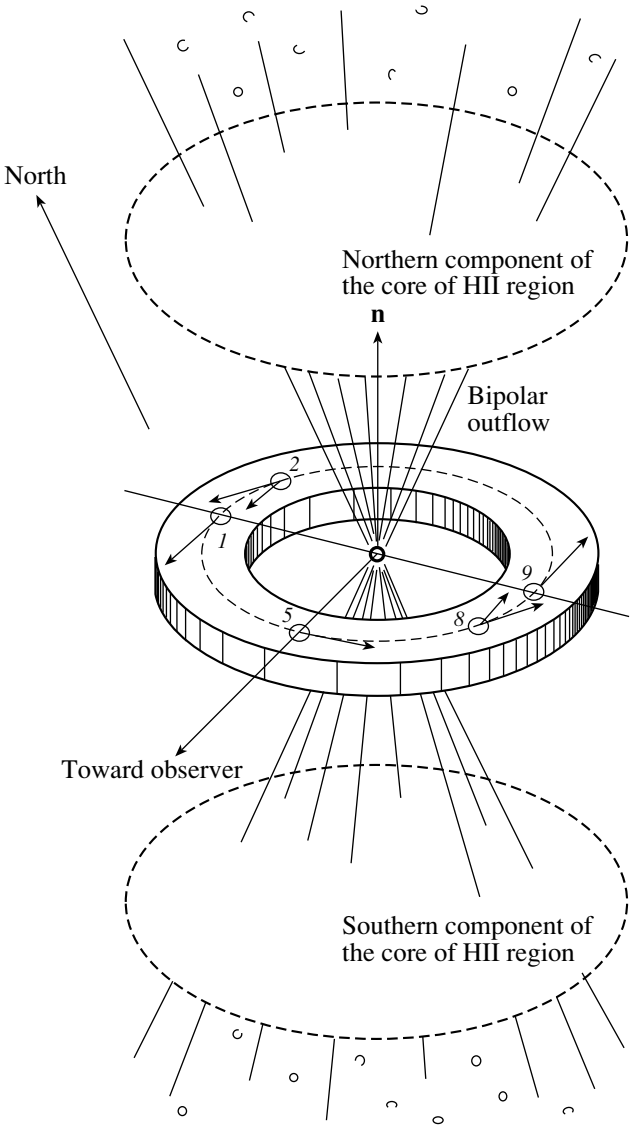

Fig. 6. Simple model for the IRS 1 water maser in NGC 7538. The components of the core of the supercompact HII region and high-velocity bipolar outflow are also shown. The star is located at the center of the disk. The arrow shows the north–south direction.

water-maser variability provides support for theoretical studies suggesting that periodic luminosity variations are possible in the early stages of the evolution of a young star.

(3) We observed jumplike variations in the velocity centroid associated with flares of individual emission features or groups of features. The appearance and disappearance of emission at the edges of the H_2O spectrum were associated with an anticorrelation of the fluxes in these spectral intervals.

(4) We detected a drift in the radial velocity of the central feature in the H_2O spectrum with $V_{LSR} = -60$ km/s. The total magnitude of the drift was about 0.6 km/s, with a drift rate of ≈ 0.09 km/s per year.

(5) We consider a very inhomogeneous protoplanetary disk to be the most promising model for the IRS 1 water maser in NGC 7538.

ACKNOWLEDGMENTS

The PRAO 22-m telescope is supported by the Ministry of Industry and Science of the Russian Federation (registration number 01-10).

The authors are grateful to the staff of the Pushchino Radio Astronomy Observatory for their considerable help with the observations.

REFERENCES

1. C. G. Wynn-Williams, E. E. Beklin, and G. Neugebauer, Astrophys. J. **187**, 473 (1974).

2. P. T. P. Ho, R. N. Martin, and A. H. Barrett, Astrophys. J. **246**, 761 (1981).
3. J. Bally and C. J. Lada, Astrophys. J. **265**, 824 (1983).
4. B. Campbell and R. I. Thompson, Astrophys. J. **279**, 650 (1984).
5. J. Fisher, D. B. Sanders, M. Simon, and P. M. Colomon, Astrophys. J. **293**, 508 (1985).
6. N. Z. Scoville, A. I. Sargent, D. V. Sanders, *et al.*, Astrophys. J. **303**, 416 (1986).
7. O. Kameya, K. I. Morita, R. Kawabe, and M. Ishiguro, Astrophys. J. **355**, 562 (1990).
8. B. Campbell and S. E. Persson, Astron. J. **95**, 1185 (1988).
9. R. A. Gaume, W. M. Goss, H. R. Dickel, *et al.*, Astrophys. J. **438**, 776 (1995).
10. E. E. Lekht, V. A. Munitsyn, and A. M. Tolmachev, Astron. Zh. (in press).
11. E. E. Lekht, M. I. Pashchenko, and G. M. Rudnitskiĭ, Astron. Zh. **59**, 276 (1982) [Sov. Astron. **26**, 168 (1982)].
12. V. V. Krasnov and V. M. Minnetaev, Radiotekh. Élektron. **47**, 120 (2002).
13. H. W. Yorke and E. Krügel, Astron. Astrophys. **54**, 183 (1977).
14. A. V. Tutukov and V. M. Shustov, Nauchn. Inform. Astron. Soveta Akad. Nauk SSSR **41**, 125 (1978).
15. E. E. Lekht, V. A. Munitsyn, and A. M. Tolmachev, Astron. Astrophys. (in press).
16. E. E. Lekht, S. F. Likhachev, V. S. Strel'nitskiĭ, and R. L. Sorochenko, Astron. Zh. **70**, 731 (1993) [Astron. Rep. **37**, 367 (1993)].
17. R. Cesaroni, Astron. Astrophys. **223**, 513 (1990).
18. V. Migenes, S. Horiuchi, V. Slysh, *et al.*, Astrophys. J., Suppl. Ser. **123**, 487 (1999).

Translated by D. Gabuzda

Astronomy Reports, Vol. 48, No. 3, 2004, pp. 210–218. Translated from Astronomicheskiĭ Zhurnal, Vol. 81, No. 3, 2004, pp. 234–243.

Masses of Protostars with Methanol Protoplanetary Disks

I. E. Val'tts and S. Yu. Lyubchenko

Astro Space Center, Lebedev Physical Institute, Russian Academy of Sciences, Profsoyuznaya ul. 84/32, Moscow, 117997 Russia

Received June 30, 2003; in final form, September 18, 2003

Abstract—The masses of 12 protostars assumed to be the central bodies in circumstellar protoplanetary disks are estimated based on analysis of their methanol maser spectra and fine spatial structure. The calculations are based on the hypothesis that the class II methanol maser lines are formed in an edge-on Keplerian disk, while the thermal methanol emission and CS lines are formed in a cocoon around the protostar. This provides information about the velocities of the protostar and the methanol maser condensations relative to the center. In most of the star-forming regions studied, the derived masses are within limits admissible for disks around massive OB stars. The masses are in good agreement with the calculations of other authors based on models of the velocity gradients of the maser features. It is suggested that the methanol spectra display a triplet structure in which the two lateral features are class II methanol lines and the central component is a class I methanol maser line or thermal methanol line. This is consistent with the fact that the correlation of regions of maser emission with regions of emission of dense molecular gas in the CS line is about twice as strong (about 100%) as the correlation with ultracompact HII regions (about 50%). This should be taken into account when modeling protoplanetary disks and star-forming regions. © *2004 MAIK "Nauka/Interperiodica"*.

1. INTRODUCTION

The most common way to derive the masses of astronomical bodies is to use the universal law of gravitation. The masses of stars in binary systems can be determined fairly accurately in this way. Such mass estimates formed the initial basis for the mass–luminosity dependence, which was then applied to derive the masses of single stars (to lower accuracy) based on their luminosities. The largest source of error in the masses of single stars is inaccuracy in their distances, which affects the estimated interstellar absorption and absolute magnitude, i.e., the luminosity of the star.

Direct determination of the absolute magnitudes of protostars or very young stars is not possible, since they are hidden in dense gas–dust cocoons. The presence of a protostar in a star-forming region is revealed indirectly: presence of an ultracompact HII region, enhanced molecular emission in dense clumps at the interface between the HII region and the molecular cloud that hosts the star-forming region, and other peculiar features. Ultracompact HII regions are detected as compact radio sources, and the molecular radio emission mases under the action of the infrared radiation from the cocoon surrounding the protostar or from the HII region's radio continuum. Methanol masers whose pumping requires radiation external to the molecular formation are called class II masers.

Thus, the mass of an invisible protostar cannot be found from the mass–luminosity dependence. However, there have been a number of recent attempts to determine the masses of protostars based on the hypothesis that class II methanol masers are formed in gas–dust disks around protostars [1–3]. It is assumed that the methanol maser condensations participate in Keplerian rotation of the disk. However, this approach also encounters a serious difficulty. Since the spectrum of the invisible protostar is unknown, it would seem to be impossible to determine its intrinsic velocity and the relative velocities of the maser condensations whose masses appear in the gravitational law. However, Val'tts and Lyubchenko [4] have shown based on an analysis of methanol maser spectra and thermal methanol and CS spectra for a large sample of sources that the velocities of the maser and thermal lines are related. If the masers are rotating around a protostar, the methanol spectrum should have a triplet profile with maser lines at the edges and a thermal line emitted by the stellar cocoon at the center. In this case, the relative velocities of the masers and the protostar can be readily determined, and this can be used to calculate the mass of the protostar. We present here masses of several protostars derived in this way. Before proceeding to our results, we discuss concepts about the methanol maser structure that lie at the basis of the protostar mass determinations reported in three earlier papers,

1063-7729/04/4803-0210$26.00

by Norris *et al.* [1], Phillips *et al.* [2], and Minier *et al.* [3].

2. MORPHOLOGY AND CLASSIFICATION OF THE STRUCTURE OF METHANOL MASERS

The first studies of the fine spatial structure of class II methanol masers were carried out on the Parkes–Tidbinbilla interferometer at 12.2 GHz [5] and the ATCA at 6.7 GHz [6]. Although both sets of observations showed a wide variety in the spatial structures of these masers, this structure lends itself to a certain classification scheme, which was first proposed in [6] and later formulated more completely in [3].

(1) Linear structures: the masers are arranged in a line.

(2) Extended structures: the masers are distributed such that their position angles are roughly the same.

(3) Complex structures: no ordered large-scale structure is observed in the source.

(4) Simple structures: the source contains only a few individual maser spots.

The most important result of [5, 6] was that many linear sources display monotonic or nearly monotonic velocity gradients across the source. Norris *et al.* [6] discussed in detail three models that could explain the linear structure of the methanol masers:

(i) jets or directed outflows,

(ii) a shock front at the boundary with the compact HII region,

(iii) circumstellar disks (often also referred to as accretion disks or protoplanetary disks).

The first two models encounter serious problems, as is discussed in [1–3]. Jets and outflows are associated with high-velocity components, while the methanol masers occupy a velocity interval of less than 20 km/s. In the shock-front model, the methanol masers, like OH masers [7], lie in a layer of dense, cool gas around a compact HII region; however, methanol is not always associated with ultracompact HII regions. In addition, neither model can explain the observed velocity gradients. Therefore, the model of an edge-on circumstellar disk seems to be the most promising, since the observed velocity gradients are approximately the type expected for such disks. Figure 1 shows a schematic of a simulated disk with methanol masers, a model spectrum, and a plot of velocity versus projected distance. It can readily be shown [1] that, if $r_{\min}$ and $r_{\max}$ are approximately the same (i.e., the maser condensations are located in a thin ring around the star), the line-of-sight velocity of a maser $V(r)$ in an edge-on disk will be a linear function of the projected distance from the star r, and the gradient dV/dr from the star to the maser condensation is a function of the mass and radius $r_{\max}$ of the star.

As is noted in [1], the gradient dV/dr can readily be determined from observational data, but the gradient itself does not provide highly accurate information about calculated physical parameters for the following reasons. The stellar mass is proportional to $r_{\max}^3$; however, $r_{\max}$ is not determined accurately from the observations, since the masers are distributed nonuniformly along the ring, and the observed projected distance r yields only a lower limit on $r_{\max}$. Therefore, only a crude estimate of the stellar mass can be obtained.

If $r_{\min}$ and $r_{\max}$ differ widely, each ring of the maser emission will form a line on which the gradient dV/dr is a function of r. The set of lines from each disk element will form a distribution of points that lie in only two quadrants of the diagram, see Fig. 13 in [1]. In this case, the measured value of $r_{\max}$ also yields only a lower limit on $r_{\max}$, but the stellar mass now depends on the envelope of the distribution formed by several lines [1]; therefore, in this case too the mass cannot be determined to high accuracy. If the disk is not edge-on, the same result will be obtained if we project the distances between masers onto the main axis of the observed distribution.

The modeling of the maser sources carried out in [1] shows that the velocity gradients correspond to Keplerian motion around stars with masses from 4 to $14M_\odot$. It is striking that the derived masses lie approximately in the interval expected for OB stars.

We will not consider in detail the question of why so many disks are viewed edge-on: this situation is discussed extensively in [1].

Though the disk model can explain well the observed velocity gradients and yields quite reasonable masses, Norris *et al.* [1] note that, unfortunately, the available observations do not yield the location of the star with respect to the locus of the maser positions, and information about the stellar velocity is absent. Thus, the division into quadrants in [1–3] that is used as the basis on which to draw conclusions about the structure of the masers is, in fact, completely relative.

However, methanol sources emit thermal lines as well as maser lines. If we take this fact into consideration, the picture changes appreciably.

3. METHANOL EMISSION PROFILE

Norris *et al.* [1] consider in detail the spectrum of a maser source in the disk model. The maximum maser amplification is achieved in the tangential direction toward the edge of the disk and in the radial

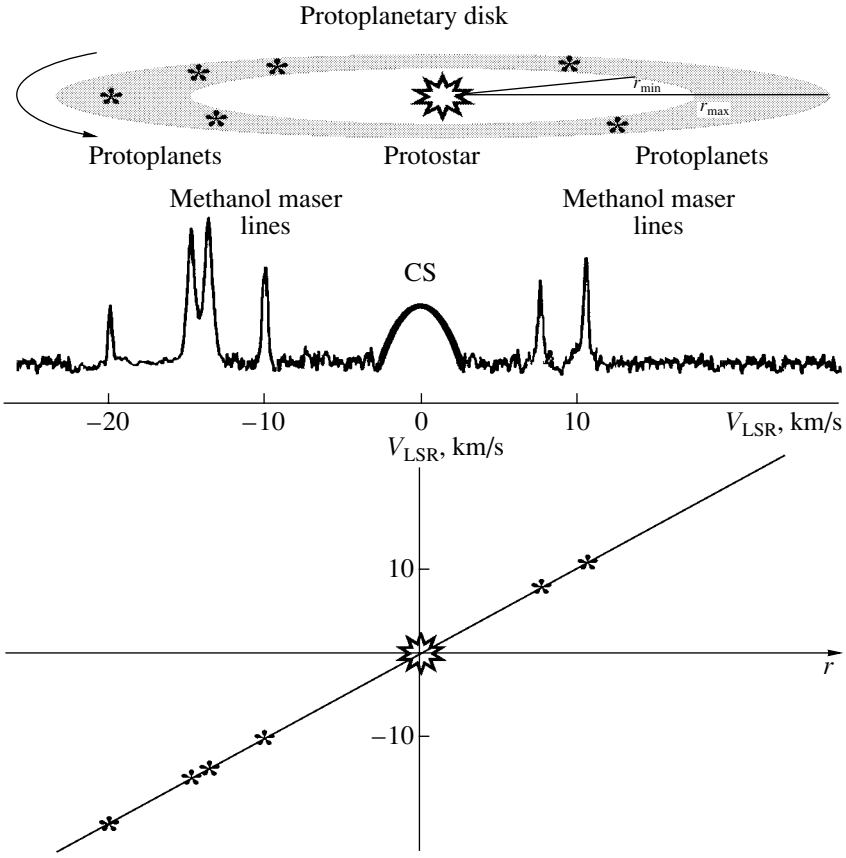

Fig. 1. Schematic model of the arrangement of methanol maser condensations (i.e., protoplanets) in a protoplanetary disk and the corresponding line profile for a hypothetical maser source and cocoon (not shown) emitting the thermal CS line. A plot of the velocity as a function of the projected distance along the source axis is shown below.

direction toward the disk's center, forming a doublet or triplet profile. Such a profile is observed for the H_2O maser in the galaxy NGC 4258 [8]. Norris *et al.* [1] emphasize that the spectrum of the methanol masers is obviously triplet, not doublet, and explain this as an effect of different characters of the local density and velocity perturbations in the circumstellar methanol disk and galactic disk. In the case of NGC 4258, the disk rotational velocity is $v_{rot} \approx 1000$ km/s, much higher than the velocities of internal motions; therefore, the masers display a triplet spectrum, corresponding to three maser clusters. The rotational velocity of methanol maser disks, $v_{rot} \approx 4$ km/s, is comparable with the internal velocity of the gas turbulence. Therefore, the maximum coherence length is achieved only at sites where parcels of gas with the same velocity are aligned along the line of sight [1].

However, Val'tts and Lyubchenko [4] noted that thermal methanol lines (as well as thermal CS lines) are frequently observed in the spectrum between the class II methanol maser lines, forming a triplet configuration, and note typical examples of triplet methanol spectra. If the maser condensations are rotating in a disk around an object that is hidden in a dense molecular cocoon, the velocities of the maser and thermal emission are related; the velocities of the maser features may represent Keplerian orbital velocities, whereas the protostar inside the cocoon emitting thermal methanol and CS lines acts like the center of mass of the system of maser sources, the central body, and the surrounding gas and dust. In this case, knowing the velocity of the thermal methanol or CS line, we can readily determine the relative velocities of the protostar within the cocoon and of protoplanets participating in the disk rotation; as was suggested by Slysh *et al.* [9], maser emission could arise in the atmospheres of these protoplanets. In this case, if each maser feature forms in the atmosphere of a separate protoplanet and each protoplanet has its own orbit, maser features having greater velocities will be less distant from the system center, and, conversely, if each maser feature is formed in the atmosphere of a separate protoplanet, and each protoplanet has its own orbit. Another picture is possible [1–3], in which the protoplanets are revolving in a single thin ring and the methanol maser spectrum reflects the projected

positions of the protoplanets on the axis connecting the center of the system and a tangent point to the ring. The spectral feature that is most remote from the thermal line will then correspond to the most distant part of the ring, i.e., to the ring's size.

We derived masses of the supposed protostars for the simplest quasilinear maser morphologies based on our hypothesis concerning the relationship between the maser and thermal lines. We restrict our analysis to mass estimates based on spectral and interferometric data [1–3] and our hypothesis about the relationship between maser and thermal lines. We consider only simple and linear structures to illustrate our new approach to determining the masses of protostars. It can readily be shown that the formula

$$\frac{GMm}{r^2} = \frac{m(\Delta V)^2}{r}$$

can be used to obtain the following simple approximate relationship, which we have used to estimate the protostellar masses:

$$M = 10^{-3}(\Delta V)^2 r D,$$

where r is the orbital radius of a protoplanet or ring, G is the gravitational constant, 6.67×10^{-8} dyne cm^2 g^{-2}, M is the protostar mass, m is the protoplanet mass, ΔV is the separation between the maser and thermal feature in the spectrum, r is the radius of the protoplanetary orbit or ring, and D is the distance to the star-forming region in kiloparsecs, with M in units of $M_\odot$, ΔV in km/s, and r in milliarcseconds (mas).

4. METHANOL MASERS IN SEPARATE ORBITS

Let us consider as examples three sources whose morphologies can be interpreted as an arrangement of protoplanets in individual orbits. In this case, the star is located on the map of the maser source on the line on the side of the maser spot that has a line-of-sight velocity that differs most from the thermal velocity.

G305.21+0.21. This object is a linear source. Figure 2a shows the spectrum of the 6.7-GHz methanol maser from [6] together with the simulated CS-line profile and the value of $V_{\rm LSR}$ from [10]. The derived position of the protostar is indicated on the map. Our calculations of the distances from the star to the maser components did not include the effect of component B. The derived mass of the protostar is $10M_\odot$, and the diameter of the disk is about 3400 AU.

G59.78+0.06. This object from a sample of northern sources has a simple structure with two clusters of maser features separated by 700 mas. Figure 2b shows the 12.2-GHz spectrum and map from [3] together with the simulated Gaussian CS-line profile and the value of $V_{\rm LSR}$ from [10]. The position of the invisible protostar derived in accordance with the velocity of the thermal emission from the surrounding gas–dust envelope is plotted on the map. The estimated mass of the hidden protostar is $23M_\odot$, and the total size of the disk is about 1700 AU.

W51. This object is a linear source. We calculated the disk size and mass using all seven spatial components of the methanol maser (15 equations) presented in [3] on the 12.2-GHz map of the source. The disk is small, with a diameter of only about 500 AU, and the mass of the protostar is $0.2M_\odot$. We used the data of Larionov *et al.* [11] obtained toward the position of the source W51e1/e2 for the CS line.

Our attempt to represent the linear sources G29.95–0.02 and G309.92+0.48 in models with individual protoplanets in separate orbits did not yield positive results.

5. METHANOL MASERS IN RINGS AROUND PROTOSTARS

We determined the disk sizes and protostar masses for six northern and five southern sources based on the hypothesis that the maser condensations are located in rings (which also forms the basis for all the calculations of [1–3]). Figures 3 and 4 show $V(r)$ diagrams for the components of the northern and southern sources, respectively. These diagrams are based on the velocities of the protostars determined from the thermal CS lines. The spectral and interferometric data are from [2, 3] (the spectrum of the 6.7-GHz methanol maser is from [12]). The masses were found using the most distant maser component of those shown on our maps. Exceptions are G327.120+0.511, for which we calculated the average mass based on the two most distant features in opposite quadrants, and G305.208+0.26, for which we excluded from consideration the two most distant features, which are weak (labeled A and B in [2]). In addition, for G309.92+0.48 we used for our Fig. 4 the part of the maser features that are the brightest at 12.2 GHz; see the map of this source in [6].

It is interesting that, in the majority of the sources presented in Figs. 3 and 4 (80%), the masers are located in the lower left quadrant of the diagram; i.e., they are moving toward the observer. This tendency was first noted in [4] and was analyzed using a large sample of sources.

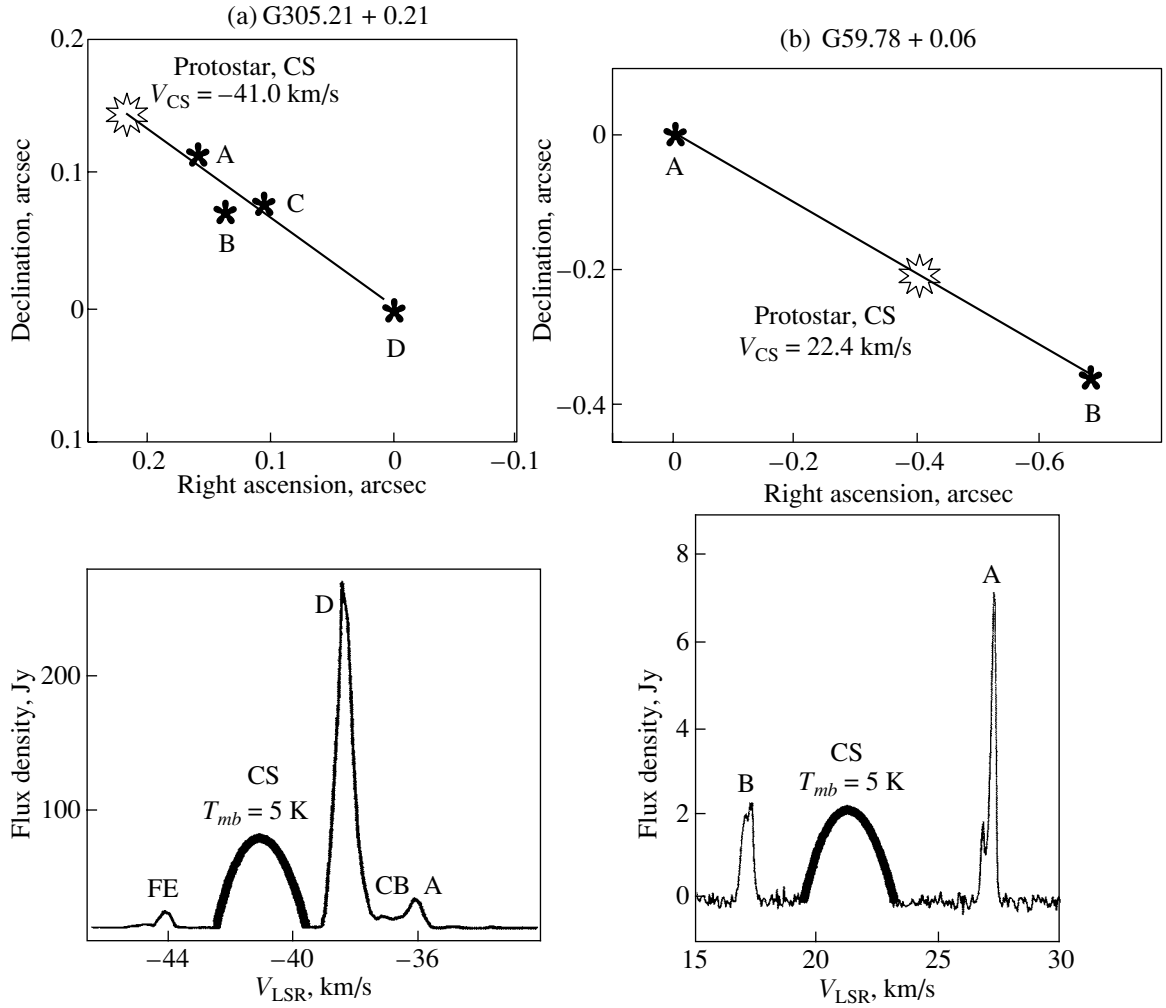

Fig. 2. Spectrum and map of (a) G305.21+0.21 at 6.7 GHz from [1] and (b) G59.78+0.06 at 12.2 GHz from [3]. The simulated profile of the CS line has the value of V_{LSR} from the survey of Bronfman *et al.* [10]. The maps show the position of the protostar according to the calculated sizes of the protoplanetary orbits (if the maser condensations are associated with protoplanets).

6. THE PECULIAR MASER SOURCE 345.01+1.79

We will consider this unique object separately. It is the only source in which 108-GHz maser emission has been detected [13] and one of only a few in which 157-GHz maser emission has been detected [14]. This indicates that the pumping conditions in the source are unusual. Two masing regions have been detected, one in the northern and one in the southern part of the source. All the strong maser lines are formed in the southern region at velocities from −24 to −14 km/s. The thermal class II transitions are concentrated at velocities from −14 to −11 km/s, closer to the velocity of the parent molecular cloud and the northern center of weak class II maser emission. The CS line has a velocity of −14 km/s [15]. Linear structure in the map of the maser spots is observed in both the southern and northerns regions, while the thermal lines are located in the spectrum between these maser groups. Furthermore, as is indicated in [1], nearly all regions of methanol-maser emission display a relationship between the rotational velocities of the maser features in the disk and the turbulent velocities in the star-forming region, $v_{rot}/v_{turb} \approx 1$; however, in 345.01+1.79(S), it appears that $v_{rot}/v_{turb} > 1$. The largest velocity spread is observed in this maser, which may correspond to v_{rot}.

The angular separation of the southern and northern regions is about 20″ for a distance of 2.3 kpc; i.e., the corresponding linear size of the entire structure of the southern and northern regions is approximately an order of magnitude larger than the linear sizes of typical maser sources. Do these two maser regions form a unified system with a common gravitational center? The mass inferred for the central source assuming that the thermal emission is associated with a hidden massive body is unreasonably large, about

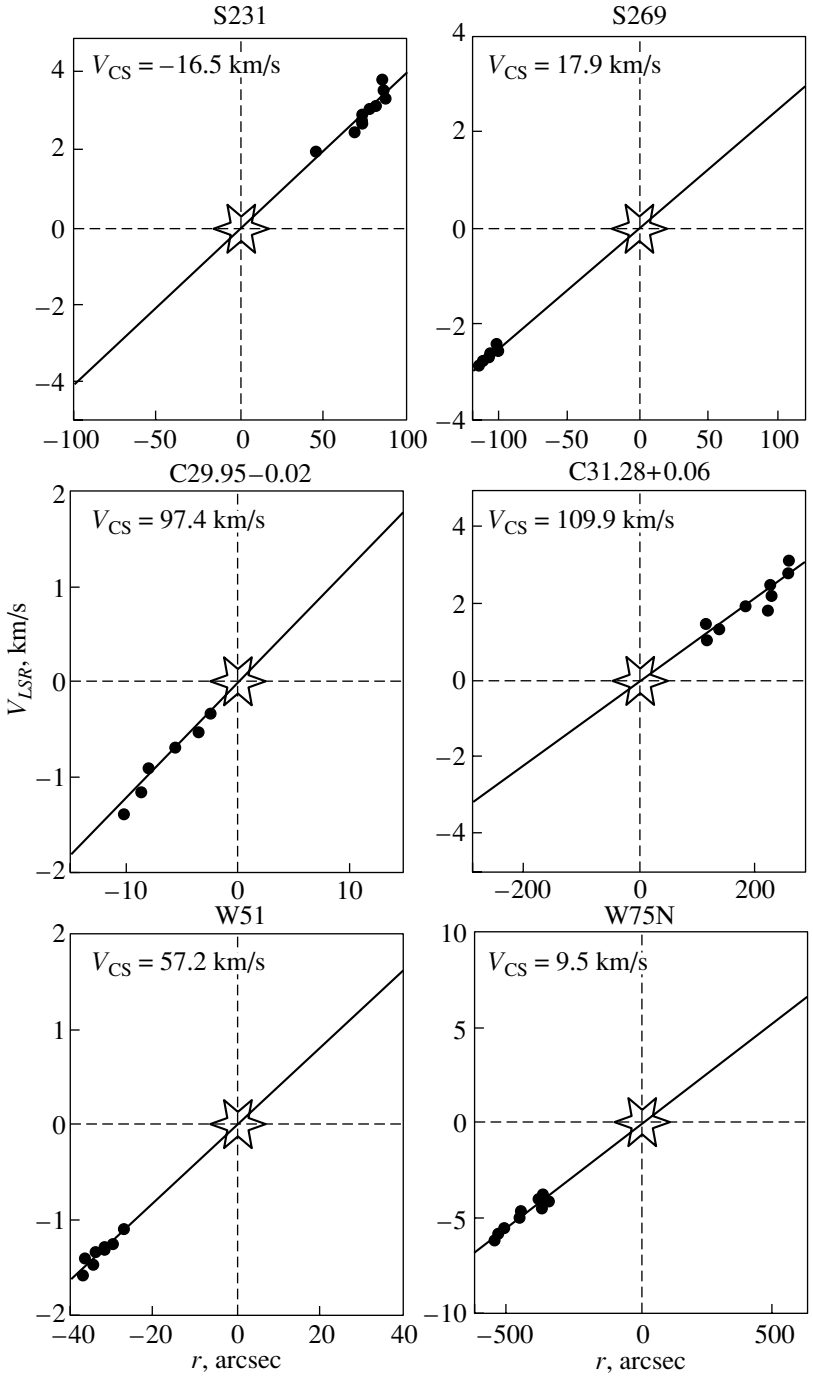

Fig. 3. Velocity–projected distance plots (with the origin at the point of intersection of the source axis and the velocity of the thermal CS line on the vertical axis) for the northern sources. The asterisk indicates the position of the protostar, and the points, the positions of methanol maser components. See text for details.

$170M_{\odot}$. Hence, the northern and southern sources probably are not parts of a single rotating Keplerian disk, and the quasi-symmetric spectral arrangement of the northern and southern groups probably has a different nature.

7. DISCUSSION

The table lists all the initial parameters and results of our calculations. The first column gives the source name; the second column, the velocity of the thermal CS line with references; and the third column, the distance to the source. Most of the distances are taken from [2, 3]; the distance to G59.78+0.06 is

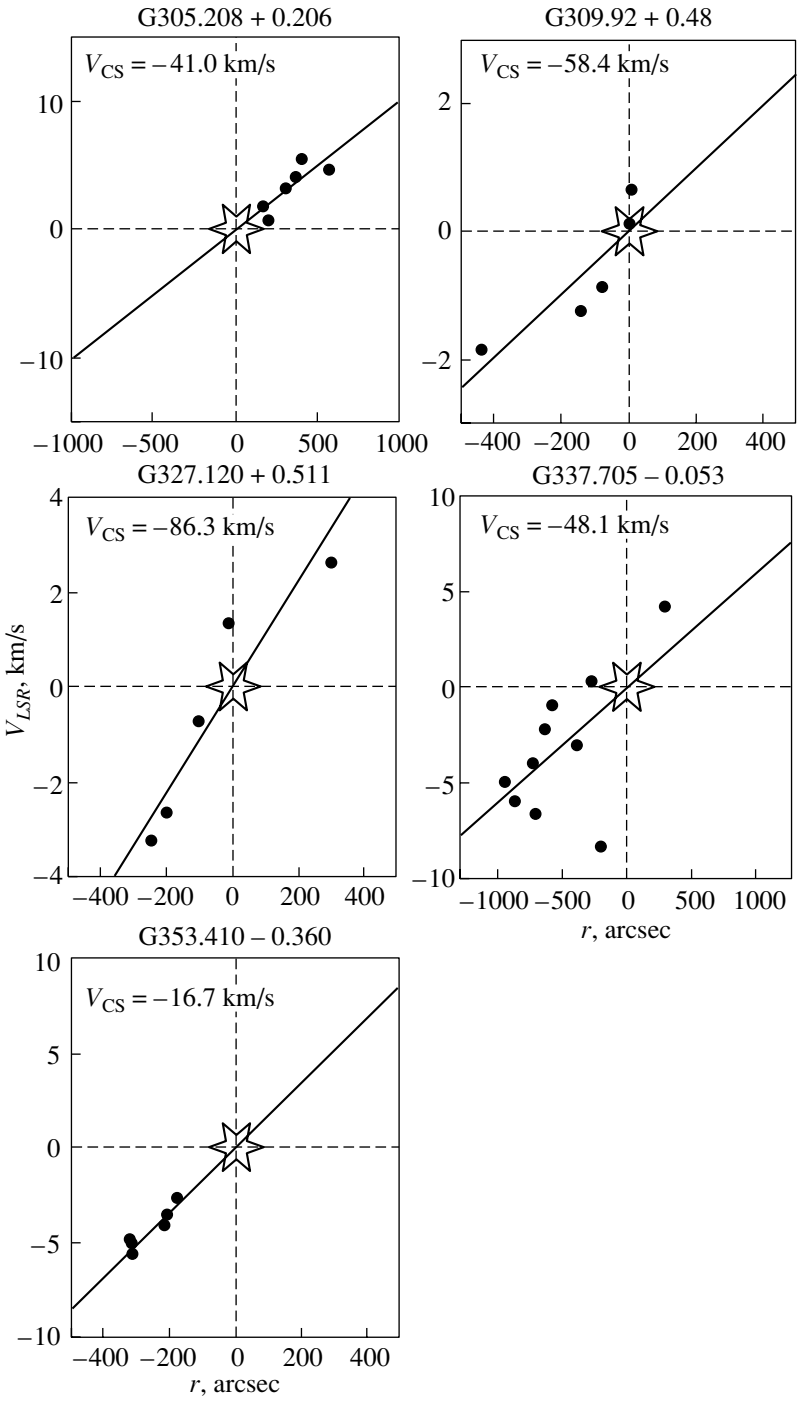

Fig. 4. Same as Fig. 3 for the southern sources.

given in [16]. The following six columns list the disk diameters and protostar masses derived for the model with protoplanets in separate orbits and the model in which all the methanol condensations form in a thin ring, as well as the results of other studies for comparison.

We note first and foremost that, for most of the star-forming regions studied, the disk sizes and protostar masses are within reasonable limits that are admissible for OB stars, as in [1–3]. In some cases, our values are close to those obtained in other studies at least to order of magnitude (see table). An exception is G353.416–0.367, for which both the disk size and the protostar mass in our calculations are much greater than in the calculations of Phillips *et al.* [2]. Our estimates indicate that the disks in W51 and G29.95–0.02 are very small and the masses of the

Protostar masses in the models with protoplanets in separate orbits and in thin rings

Source name	V_{CS}, km/s	Distance D, kpc	"Orbit" model		"Ring" model		Results of other authors	
			diameter d of the largest orbit, AU	protostar mass, $M_\odot$	ring diameter, AU	protostar mass, $M_\odot$	ring diameter, AU	protostar mass, $M_\odot$
S231	−16.5 [11]	2.5	–	–	420	3	95–1000 [3]	0.04–41.7 [3]
S269	17.9 [10]	4.0	–	–	910	4	55–1200 [3]	0.001–10 [3]
G305.208+0.206	−41.0 [10]	6.2	3440	10	4460	35	1600 [1]	1 [1]
							4960 [2]	5.8 [2]
G309.92+0.48	−58.4 [10]	5.5	–	–	4840	8	4300 [1]	10 [1]
							4240 [2]	9.6 [2]
G327.120+0.511	−86.3 [10]	5.5	–	–	2660	13	3300 [2]	14.7 [2]
G337.705−0.053	−48.1 [10]	3.9	–	–	7300	86	5460 [2]	72.6 [2]
G353.416−0.367	−16.7 [10]	3.9	–	–	2470	29	624 [2]	0.5 [2]
G29.95−0.02	97.4 [10]	9	–	–	190	0.2	85–1000 [3]	0.02–30.8 [3]
G31.28+0.06	109.9 [10]	5.6	–	–	2890	15	780–2600 [3]	0.26–10 [3]
G59.78+0.06	22.4 [10]	2.2	1720	23	–	–	–	–
W51	57.2 [11]	7.5	490	0.2	550	0.7	70–1300 [3]	0.002–10 [3]
W75N	9.5 [11]	2	–	–	2180	42	380–1320 [3]	0.24–10 [3]

central protostars do not exceed $1M_\odot$; this does not contradict the estimates of [3].

The masses we have derived are more precise, since we have used the projected distances to the maser condensations (i.e., protoplanets), which are determined from observations, instead of r_{max}, whose determination requires adopting additional hypotheses or accepting the derived masses as lower limits.

Note that we obtained a reasonable disk size and protostar mass in the thin-ring model for G309.92+0.48 (for the components of the 12.2-GHz maser), while the ring-model mass for G305.21+0.21 ($35M_\odot$) differs strongly from the results obtained assuming protoplanets in individual orbits and the results of [1].

Phillips *et al.* [2] carried out a detailed analysis of the coincidences of methanol masers with ultracompact HII regions. Such coincidences are observed for only half of the masers; in addition, the maser and continuum centers are usually shifted with respect to each other. At the same time, the frequency of coincidences of maser emission with thermal CS emission is much higher: in the sample of Caswell *et al.* [17], 80 of 135 masers (60%) have counterparts in the CS line [10], although the survey [10] targeted HII regions. In the survey of Larionov *et al.* [11], which was concerned precisely with CS-line observations of methanol masers, the number of coincidences reaches 94%. It is likely that dedicated observations of methanol masers from the list of Caswell *et al.* [17] would yield a higher number of coincidences. However, our search [18] for maser and thermal emission in the strongest CS emission sources from [10] did not yield positive results. This is likely due to the fact that the observations of [18] were carried out at 107 GHz, where methanol masers are much less common than at 6.7 and 12.2 GHz.

To determine the masses of the central protostars, we should likewise take into account data on OH and H_2O masers and analyze how precisely the spectral features of these masers are correlated with those of the maser and thermal methanol emission based on a rich, uniform sample.

In addition, methanol masers also emit class I lines, although the lack of spatial noncoincidence of class I and II methanol sources is one of their main distinguishing characteristics. In fact, class I methanol masers are frequently found toward star-forming regions in which class II methanol masers are observed. A Parkes list used to search for class I methanol masers at 44 GHz included mostly class II masers, which emit at 6.7 GHz; in many cases, class I masers were detected [19], although with anticorrelated fluxes. However, the velocities of the features in the spectra of the class I and II methanol masers do not coincide, and the velocities of the class I masers are close to those of their parent molecular clouds.

This has been noted in a number of studies, and Val'tts and Larionov [20] analyzed in detail the mutual arrangement of class I methanol maser features at 44 and 95 GHz and of thermal CS lines. However, we can state fairly confidently that the methanol emission spectra form triplet structures, in which the lateral components are class II lines and the central peak is a class I line or thermal feature. However, this quasi-triplet can occur at widely separated frequencies, so that it was probably not recognized as such earlier.

Certainly, the nature of class II methanol masers can be different in different sources. This is especially true for masers with complex morphologies, such as those in W3(OH), in which the masers form at the front of the HII region, probably in the atmospheres of protoplanets, as is shown, for example, in [9]. Thus, the question of why class II methanol maser lines form at the edge of the disk, while class I lines are observed toward the star itself (i.e., toward the center of the disk, in our picture), demands further studies of the pumping mechanisms for these masers.

8. CONCLUSIONS

(1) If we adopt a model in which class II methanol maser lines are formed at the edges of a Keplerian disk, while the thermal methanol emission and CS lines are formed in a cocoon around a protostar at the disk center, we can derive the velocities of the protostar and of the methanol maser condensations relative to the protostar.

(2) We have estimated the partial disk sizes and masses of 12 protostars in this way, which are within the range admissible for disks around massive OB stars.

(3) The results agree well with those of other studies based on Keplerian-disk models for the velocity gradients of the maser features, without regard to the velocity of the central body.

(4) We suggest that methanol masers display a triplet structure in which the two lateral features are class II maser lines, while the central component is a class I maser line or thermal methanol line.

(5) The validity of the hypotheses underlying our analysis is supported by the fact that coincidences of maser emission regions with emission regions of dense molecular gas and the CS line are observed twice as often (about 100%) as coincidences with ultracompact HII regions (50%). This should be taken into account when modeling protoplanetary disks and star-forming regions.

ACKNOWLEDGMENTS

The authors are grateful to V.I. Slysh for useful discussions. This work was partially supported by the Russian Foundation for Basic Research (project code 01-02-16902), a CRDF grant (RP1-2392-MO-92), the Program for Fundamental Research of the Branch of Physical Sciences of the Russian Academy of Sciences "Extended Objects in the Universe." This research also received support in the framework of the preparation of a program of observations of masers in star-forming regions on the Kalyazin Radio Telescope.

REFERENCES

1. R. P. Norris, S. E. Byleveld, P. J. Diamond, *et al.*, Astrophys. J. **508**, 275 (1998).
2. C. J. Phillips, R. P. Norris, S. P. Ellingsen, and P. M. McCulloch, Mon. Not. R. Astron. Soc. **300**, 1131 (1998).
3. V. Minier, R. S. Booth, and J. E. Conway, Astron. Astrophys. **362**, 1093 (2000).
4. I. E. Val'tts and S. Yu. Lyubchenko, Astron. Zh. **80**, 867 (2003).
5. R. P. Norris, W. H. McCutcheon, J. L. Caswell, *et al.*, Nature **335**, 149 (1988).
6. R. P. Norris, J. B. Whiteoak, J. L. Caswell, *et al.*, Astrophys. J. **412**, 222 (1993).
7. M. Elitzur, Astron. Astrophys. **30**, 75 (1992).
8. M. Miyoshi, J. Moran, J. Hernstein, *et al.*, Nature **373**, 127 (1995).
9. V. I. Slysh, I. E. Val'tts, S. V. Kalenskiĭ, and G. M. Larionov, Astron. Zh. **76**, 751 (1999) [Astron. Rep. **43**, 657 (1999)].
10. L. Bronfman, L. A. Nyman, and J. May, Astron. Astrophys., Suppl. Ser. **115**, 81 (1996).
11. G. M. Larionov, I. E. Val'tts, A. Winnberg, *et al.*, Astron. Astrophys., Suppl. Ser. **139**, 257 (1999).
12. M. Szymczak, G. Hrynek, and A. J. Kus, Astron. Astrophys., Suppl. Ser. **143**, 269 (2000).
13. V. I. Slysh, I. E. Val'tts, and S. V. Kalenskiĭ, Astron. Zh. **79**, 54 (2002) [Astron. Rep. **46**, 49 (2002)].
14. V. I. Slysh, S. V. Kalenskii, and I. E. Val'tts, Astrophys. J. **442**, 668 (1995).
15. M. Juvela, Astron. Astrophys., Suppl. Ser. **118**, 191 (1996).
16. R. Plume, D. T. Jaffe, and N. J. Evans, Astrophys. J., Suppl. Ser. **78**, 505 (1992).
17. J. L. Caswell, R. A. Vaile, S. P. Ellingsen, and R. P. Norris, Mon. Not. R. Astron. Soc. **1126**, 274 (1995).
18. I. E. Val'tts, S. P. Ellingsen, V. I. Slysh, *et al.*, Mon. Not. R. Astron. Soc. **310**, 1077 (1999).
19. V. I. Slysh, S. V. Kalenskii, I. E. Val'tts, and R. Otrupcek, Mon. Not. R. Astron. Soc. **268**, 464 (1994).
20. I. E. Val'tts and G. M. Larionov, Astron. Zh. (2004, in press).

Translated by G. Rudnitskiĭ

Astronomy Reports, Vol. 48, No. 3, 2004, pp. 219–228. Translated from Astronomicheskiĭ Zhurnal, Vol. 81, No. 3, 2004, pp. 244–254.

Evolutionary Connection between Low-Mass Detached Binaries, Contact W UMa Systems, and Blue Stragglers

A. V. Tutukov[1], G. N. Dremova[2], and M. A. Svechnikov[2]

[1] *Institute of Astronomy, Russian Academy of Sciences, ul. Pyatnitskaya 48, Moscow, 119017 Russia*

[2] *Ural State University, pr. Lenina 51, Yekaterinburg, 620083 Russia*

Received May 16, 2003; in final form, August 8, 2003

Abstract—We analyze the distribution of close binary stars in the orbital semimajor axis—primary mass plane. The reduced spatial density of stars with semimajor axes below $10R_\odot$ is confirmed. We identify the area in this plane occupied by precursors of W UMa stars, assuming that the driving force causing the components to approach each other is their magnetic stellar wind. This scenario enables us to estimate the rate of formation (0.02/year) and lifetime (10^8 yr) of W UMa stars. We derive a theoretical estimate of the ratio of the number of blue stragglers, N_{BS}, and of horizontal-branch stars, N_{HB}, in globular clusters based on the hypothesis that all blue stragglers are the result of component mergers in W UMa contact binaries. This ratio is $N_{BS}/N_{HB} = 0.4$, close to the observed value for 62 Galactic globular clusters. We discuss possible reasons for the considerable dispersion of the observed estimates of this ratio for different clusters in our Galaxy. © *2004 MAIK "Nauka/Interperiodica"*.

1. INTRODUCTION

The possibility that late-type (later than F0) contact systems, referred to as W UMa systems in the literature, could be formed from low-mass detached close binary systems via the loss of orbital angular momentum due to the magnetic stellar wind (MSW) was proposed as early as the 1960s [1–6].

The empirical basis of this scenario is provided by observational data on stellar rotation rates in clusters of different ages, which testify to a considerable decrease in the rotation rates of single solar-type stars with age, expressed by the empirical law of Skumanich [7]. Evidence for the action of an MSW is also provided by the coronal activity of W UMa contact systems in the X-ray and radio, manifest in the presence of dark spots in the photospheric and chromospheric emission [8] and in the strong variability of the light curves of these contact systems. This latter property is related to the effects of mass transfer or mass loss from the system [9] and is reflected by the occurrence of abrupt changes in the orbital periods, which were systematized by Kreiner [10] in his analysis of $(O-C)$ diagrams. It later became possible to study the evolutionary of a number of close binaries whose components were capable of supporting an MSW using semiempirical estimates of the efficiency of the angular-momentum loss via the MSW [11–13] based on the rotation rates of late-type stars [7]. These close binaries were contact W UMa systems, cataclysmic systems, and low-mass close X-ray binaries.

Studies of component mergers in W UMa systems due to the action of the MSW make it possible to explain the origin of single "blue stragglers" populating old clusters (older than 2×10^9 yr) [14–17]. Thus, a connection between low-mass, detached, close binaries and single blue stragglers was established. The current paper will demonstrate this connection based on extensive observational material from the catalog of approximate photometric and absolute elements for eclipsing variables of Svechnikov and Kuznetsova [18], using a formalism developed to include the influence of the MSW [13].

Magnetic braking, which is used to explain the evolutionary transition from detached, low-mass, close binaries to contact systems, reveals its action through the loss of orbital angular momentum via the MSW. Mestel [3] and Spitzer [19] introduced the term "magnetic braking" in connection with the loss of angular momentum by a collapsing protostellar cloud during the formation of a star. The loss of angular momentum by single stars via the MSW has been studied by Schatzman [1] and others [3, 20]. The success of the quantitative theory of magnetic braking is due to the use of an approximate empirical relation between the rotation rates and ages of solar-type stars, $V_{\rm rot} \sim t^{-1/2}$ [7], to quantitatively normalize the efficiency of the MSW. Studies of the evolution of cataclysmic variables demonstrate that the presence of a convective envelope and radiative core are necessary conditions in order for the MSW to be efficient. Fully convective stars [13] do not possess

efficient MSWs. Only the components of low-mass, detached, close binaries with masses of $0.3{-}1.5M_\odot$ have well-developed convective envelopes and radiative cores, so that their MSWs can influence the evolution of these close binaries. Thus, the main goal of the current paper is to carry out a quantitative test of the evolution scenario low-mass, detached, close binaries → W UMa systems → blue stragglers for component masses of $0.3{-}1.5M_\odot$ using a formalism developed to include the MSW [13].

2. THE $\log M_1{-}\log A$ DIAGRAM

The $M_1{-}A$ diagram occupies a central place in studies of early stages in the evolution of low-mass close binaries. In his study of eclipsing systems with known absolute elements at the end of the 1960s, Svechnikov [21] was the first to note a deficiency of short-period, detached, close binaries with $M_1 + M_2 \geq 2.5M_\odot$ and $A \leq 10R_\odot$ [21, Fig. 12], although contact systems with $M_1 + M_2 \geq 2.5M_\odot$ were well represented in the diagram. This area acquired the name "the forbidden triangle." The existence of the forbidden triangle in the $\log M_1{-}\log A$ diagram was confirmed by Kraicheva *et al.* [22] and Staniucha [23], who analyzed data for spectroscopic binaries for which the spectra of both components were visible (SB2). In addition, after a careful analysis of the observational selection effects, it was demonstrated [11, 22] that the spatial density of detached and contact binaries with $A/R_\odot \leq 6(M_1/M_\odot)^{1/3}$ is significantly (by more than a factor of ten) lower than the density of wider systems. As a result, it became clear that all young close binaries should have semimajor axes above this limit. Closer (W UMa) systems arise due to the action of the MSW of components with convective envelopes and radiative cores, with the radiation of gravitational waves by close binaries with $A/R_\odot \leq 6(M_1/M_\odot)^{1/3}$ having a negligible effect on their evolution.

In the early 1980s, the absence of young binary stars with $A/R_\odot \leq 6(M_1/M_\odot)^{1/3}$ was explained by Popova *et al.* [11] as a consequence of the formation conditions for close binaries. The accretion regime operating during the formation of the components of close binaries sets a limit of $\sim 3R_\odot$ on the radii of young stars in such systems. As a result, the components of the closest binaries merge during the Hayashi stage, forming single stars. The rotation of the products of such mergers with masses below $\sim 1.5M_\odot$ rapidly slows due to the action of their MSW, whereas stars with higher masses probably remain rapidly rotating main-sequence A stars. There is a lower limit for the major axes of "surviving" systems,

$$\left(\frac{A_{\min}}{R_\odot}\right)_{\rm low} \sim 6\left(\frac{M_1}{M_\odot}\right)^{1/3}, \quad P_{\rm orb} \sim 1\overset{\rm d}{.}2. \qquad (1)$$

In the current paper, we consider the $\log M_1{-}\log A$ diagram using observational material from the catalog of close binaries of Svechnikov and Kuznetsova [18], which includes 437 detached main-sequence (DMS) systems, 153 precontact (~CW, or short-period RS CVn) systems, 304 W UMa contact (CW) systems, and 462 early-type contact (CE) systems. The abbreviations in parentheses indicate the close-binary evolutionary status according to the classification of Svechnikov [24]. Figure 1a shows all the systems of these classes with visual magnitudes brighter than 10^m, whereas Fig. 1b shows only those close binaries with $m_v \geq 10^m$.

Let us now identify in Fig. 1 the "feeding zone" with objects that can give rise to contact close binaries and blue stragglers due to the action of an MSW. Relation (1) delineates the lower boundary of the area of detached close binaries (dot–dash line). In the course of their evolution, systems in which the mass of one of the components does not exceed $1.5M_\odot$ can enter the "forbidden zone" with $P \leq 1\overset{\rm d}{.}2$ if they have lost most of their initial orbital angular momentum via magnetic braking. Since the evolution of close binaries with masses this low is determined by the time scale for the loss of orbital momentum via the MSW, τ_{MSW}, rather than by the primary's nuclear time scale, $\tau_{MS}^{(1)}$, we can derive two more boundaries for the contact-system feeding zone determined by the primary and secondary components by equating these two scales ($\tau_{MSW} = \tau_{MS}^{(1)}$). According to Iben and Tutukov [13], the time scale for the loss of orbital angular momentum via the MSW can be written as

$$\tau_{MSW} = 3 \times 10^6 \frac{A^5}{{R_1}^4} \frac{M_1}{(M_1 + M_2)^2} \text{ yr}. \qquad (2)$$

The lifetime of a primary in a close binary on the main sequence is

$$\tau_{MS}^{(1)} = 10^{10} {M_1}^{-2.9} \text{ yr}. \qquad (3)$$

Since detached binaries with $M_1 \leq 1.5M_\odot$ and $M_2 \leq 1.5M_\odot$ lose their angular momentum via the MSW twice as intensely, we can use the condition $\tau_{MSW}^{(1)}/2 = \tau_{MS}^{(1)}$ to estimate an upper boundary for the feeding zone based on the primary component (dashed line in Fig. 1):

$$\left(\frac{A}{R_\odot}\right)_{\rm upper} \approx 7.67\left(\frac{M_1}{M_\odot}\right)^{0.42}. \qquad (4)$$

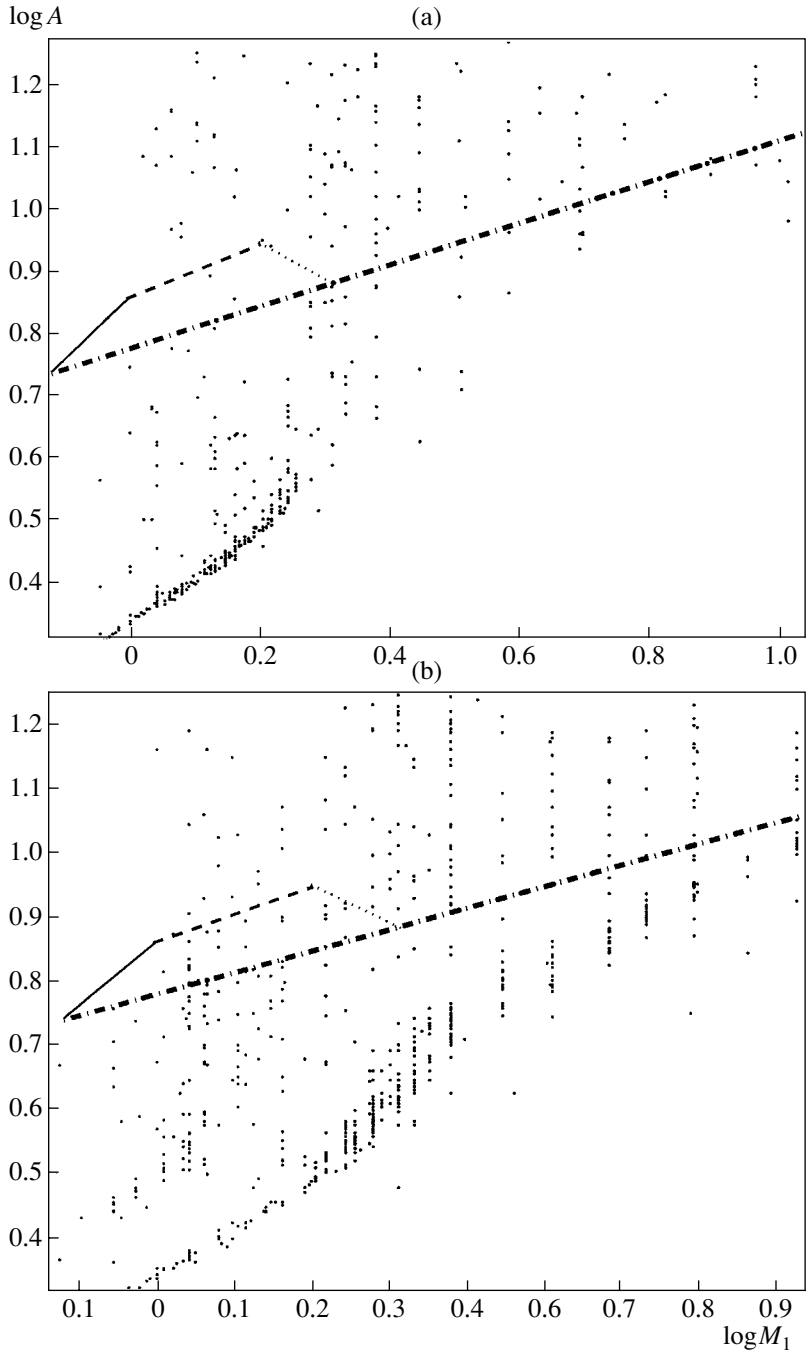

Fig. 1. (a) M_1–A diagram for close binaries of various classes with $m_v \leq 10^m$. The boundaries delineate the "feeding zone" with detached close binaries that are potential parents of late-type contact systems and, further, of single merging blue straggler-type objects. (b) M_1–A diagram for close binaries of various classes with $m_v > 10^m$.

However, since not only close binaries with $M_1 \leq 1.5M_\odot$ can enter the forbidden triangle in the course of their evolution but also detached close binaries with $M_1 \geq 1.5M_\odot$ and $M_2 \leq 1.5M_\odot$, in which only one component is responsible for the magnetic braking, we can use the condition $\tau^{(2)}_{MSW} = \tau^{(1)}_{MS}$ to derive a right-hand boundary for the feeding zone based on the secondary component (dotted line in Fig. 1):

$$\left(\frac{A}{R_\odot}\right)_{\text{right}} \approx 11.58\left(\frac{M_1}{M_\odot}\right)^{-0.58}. \qquad (5)$$

Equations (4) and (5) identify systems in Fig. 1 whose lifetimes are limited by magnetic braking.

To find the last boundary of the contact-system

feeding zone, we can use the fact that the time scale for the process of coming into contact, i.e., for the evolutionary transition from a low-mass detached system to a contact close binary, is limited by our Galaxy's age τ_{Galaxy}. The solid line in Fig. 1 was found from the condition $\tau^{(1)}_{MSW} = \tau_{Galaxy}$ by assuming that the lifetime of the Galaxy is $\tau_{Galaxy} \approx 15 \cdot 10^9$ yr:

$$\left(\frac{A}{R_\odot}\right)_{\text{left}} \approx 7.25\frac{M_1}{M_\odot}. \quad (6)$$

The four boundaries plotted using (1) and (4)–(6) enclose an area in the $\log M_1$–$\log A$ plane resembling a "feeding trapezoid." This area includes all young detached binaries that are capable of forming late-type contact systems via the action of their MSW in the course of their evolution.

Analyzing Fig. 1, we can immediately understand why the masses of the primaries in W UMa systems are restricted to the range 0.8–$1.5M_\odot$ and the orbital periods of these systems to the range 0.3–0.6 days [25]. These boundaries are determined by the boundaries of the feeding trapezoid. It is interesting that, judging from the evolution of cataclysmic systems, close binaries with masses of 0.3–$0.8M_\odot$ possess efficient MSWs [18], but, as follows from Fig. 1, these MSWs are insufficient to form contact systems with these masses over the Hubble time. Figure 1 also demonstrates the presence of many systems that are on the way to forming contact binaries, whose components are in the process of approaching each other.

Figure 1 shows that the forbidden area with $A/R_\odot \leq 6(M_1/M_\odot)^{1/3}$ and $M_1 \approx 1.5$–$6M_\odot$ also contains some close binaries. Let us consider possible mechanisms for populating this zone. Systems with $M_1 \approx 1.5$–$2M_\odot$ can become closer in the course of their evolution via the MSW from secondaries with masses of $M_2 \approx 0.3$–$1.5M_\odot$. Some of the systems in this area of Fig. 1 could have evolved due to mass transfer between the components or a common-envelope stage. An excellent example of such a system is v Sge ($A \approx 3R_\odot$), a contact close binary containing a degenerate dwarf with a mass of $\sim 0.9M_\odot$ and a $3.3M_\odot$ main-sequence star. The degenerate dwarf is a bright source of soft X rays ($L_X \approx 10^{38}$ erg/s) [26] generated in the hydrogen-burning shell source [27]. Another possible way to populate the forbidden zone in Fig. 1 is the disruption of multiple, primarily close triple, systems. Judging from the observed distribution of semimajor axes for their components, about 10% of these systems are unstable due to the low ratios of the subsystem axes. Multiple systems are common. For example, three of ten W UMa stars studied in detail were found to be triple systems [28], and seven of ten blue-straggler objects proved to be binaries [29]. Some of the blue stragglers could initially have been close triple systems whose disruption brought the components of the close binary closer to distances subject to the influence of the MSW.

Triple systems suggest another possibility for bringing the components of a close binary closer: the "propeller" effect, which operates when the distant component expands due to its nuclear evolution and fills its Roche lobe, so that some of its matter falls into the Roche lobe of the inner close-binary components. Some of this matter will be accreted by the close binary, and some will be ejected by the propeller action of the orbital motion. When the propeller mechanism operates, the binary components will unavoidably become closer and "descend" into the forbidden zone (Fig. 1). This process has not been studied via numerical simulations, making it difficult to obtain quantitative estimates of the mechanism's efficiency. It is possible that some W UMa stars and blue stragglers were initially triple systems that have undergone a propeller stage. These various possibilities help us understand the presence of close binaries in the forbidden zone in Fig. 1. We note, however, that the main mechanism for populating the forbidden zone and creating W UMa stars remains the action of the MSW of components with initial masses of 0.8–$1.5M_\odot$. Firm evidence for this is provided by the mass distribution for the primaries in the W UMa contact stars in Fig. 1a, whose boundaries coincide with those of the feeding trapezoid.

3. DISTRIBUTION OF LOW-MASS CLOSE BINARIES IN $\log A$

Several selection effects distort the distribution of close binaries in Fig. 1 and must be taken into account when constructing the initial, intrinsic semimajor axis distribution for the close binaries. This distribution can be derived from the observed distributions after they have been corrected for these observational selection effects. These include the geometrical, W_1, and photometric, W_2, probabilities for the close binaries to be detected as eclipsing variables; the volume V in which this type of system is observed to a given limiting magnitude; and a sample incompleteness factor, f, to account for the existence of undetected faint systems.

The geometrical detection probability, W_1, is the probability for the close binary's orbital plane to be oriented relative to the observer such that eclipses with a depth at least equal to the detection limit, Δm_{lim}, will occur [30].

The photometric detection probability, W_2, is the probability that an observer will detect variability of

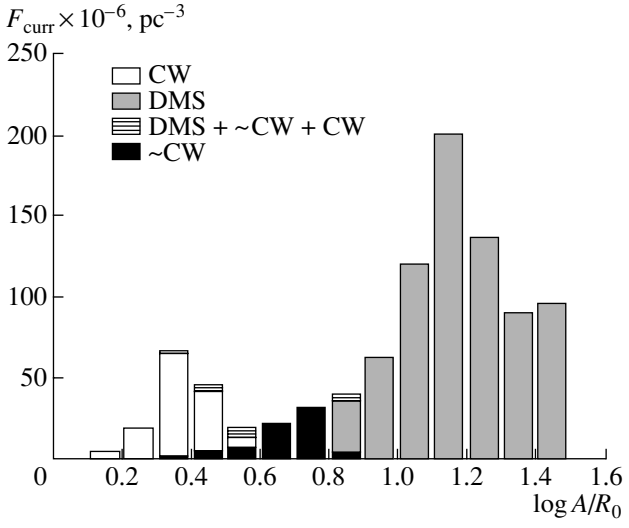

Fig. 2. Current semimajor axis ($\langle\log A\rangle$) distribution for detached (DMS), semicontact (~CW), and contact (CW) close binaries contained in a unit volume of space in the solar neighborhood.

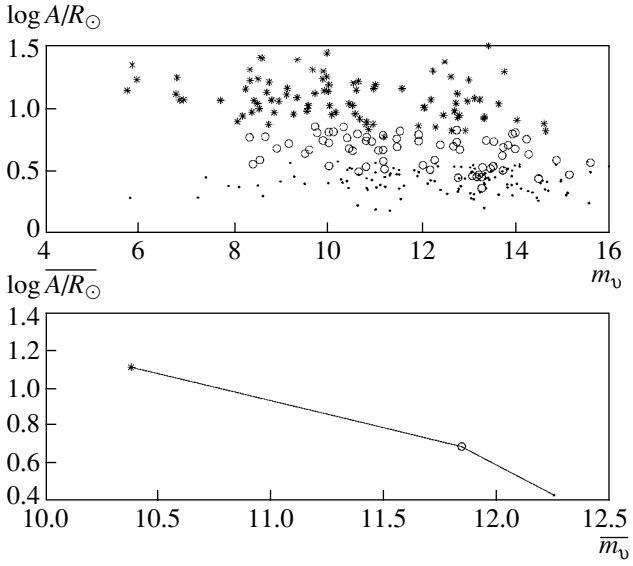

Fig. 3. Dependence of the logarithm of the orbital semimajor axis on apparent magnitude (top) and dependence of the mean logarithm of the orbital semimajor axis on the mean apparent magnitude (bottom). DMS systems are denoted by asterisks; ~CW systems, by circles; and CW systems, by dots.

a close binary with an amplitude exceeding the detection limit, $\Delta m_{\rm lim}$. The value of W_2 depends on several factors: the detection method, the difference in the photometric epochs, the shape of the light curve, the amplitude of the brightness variations, the mean magnitude, and the ratio of the period and the difference in the photometric epochs.

The total close-binary detection probability is equal to the product of the geometrical and photometric probabilities, $W = W_1W_2$, and can be expressed for detached and precontact systems (DMS and ~CW) as a function $W(M_1, A, q, i)$ of four variables: the primary mass M_1, semimajor orbital axis of the system A, component-mass ratio q, and orbital inclination i. For contact systems (CW), the value of A is uniquely determined by M_1 and q, so that the probability of their detection as eclipsing variables can be computed from M_1, q, and i. We calculated the detection probability, $W_i(M_1, A, q, i)$ or $W_i(M_1, A, q, i)$, individually for each system via linear interpolation between known tabulated probabilities from [31, 32]. It was shown in [33] that the error in the photometric detection probability estimated using Monte Carlo simulations is no greater than 3%, while the error in the geometrical detection probability, for which the empirical M_1-R relation for main-sequence stars must be known, is no greater than 7%.

The volume V_i is estimated individually for each system as the volume of a spherical layer with thickness $h = 180$ pc [34] and limiting radius r_i equal to the distance from the observer to the corresponding system. When computing these volumes, we assumed the parameter β in the distribution $D = D_0\exp(-|z|/\beta)$ to be equal to 90 pc for the entire subsystem of eclipsing variable stars, regardless of their type [35, 36].

Taking into account the sample incompleteness factor, f_i, which we also determined individually for each system, makes it possible to reconstruct the "true" spatial density in the solar neighborhood for close binaries that were missed because, as the visual magnitude m_v increases, the number of systems detected increases more slowly than does the volume of the corresponding layer.

With this in mind, we can construct the current spatial distribution of the semimajor axes of close binaries,

$$F_{\rm curr}(\Delta_j \log A) = \sum_{i=1}^{n} \frac{1}{W_i V_i} f_i, \qquad (7)$$

and compute the behavior of this density for the close-binary classes studied here (DMS, ~CW, CW) (Fig. 2). The detached systems (DMS), which were limited to those with brightnesses exceeding 15^m, include only systems satisfying the conditions $0.8M_\odot \le M_1 \le 1.5M_\odot$ and $1.5M_\odot < M_1 \le 2.8M_\odot$, $M_2 \le 1.5M_\odot$. We included essentially all the precontact (~CW) and contact W UMa (CW) systems to 16^m from the catalog [18].

Figure 2 indeed shows a rapid decrease in the close-binary density for $A \le 10R_\odot$. As was shown

earlier, this is due to the limiting size of the young stellar components in such systems ($\sim 3R_\odot$). The decrease in the density with decreasing semimajor axis (Fig. 2) results from the increased rate of approach of the components of detached close binaries with decreasing A. The increase in the close-binary spatial density for $A \approx 2R_\odot$ (Fig. 2), corresponding to W UMa stars, is striking. The most probable origin of this local maximum is an excess of such stars in modern close-binary catalogs due to the favorable conditions for their detection due to their short periods and "standard" light curves, as well as the ease of applying modern photometric techniques to large numbers of stars, which make it possible to detect many W UMa stars in a short time [25]. Note that the nuclear evolution of the components of wide systems and the possible evolution of the binary in a common-envelope stage are not able to populate this area so densely, as is shown by the more massive ($M_1 \geq 2M_\odot$) contact systems in Fig. 1.

Figure 3 clearly demonstrates the role of one of the observational selection effects: the apparent brightness of the close binaries increases with increasing semimajor axis. This provides evidence for an increase in the spatial density of stars as the orbital semimajor axes increase in the range 3–$13R_\odot$. Simple estimates show that a two-magnitude change in the apparent brightness corresponds to a change in the spatial density by a factor of 16. Our statistical analysis of the data from the catalog of close binaries of Svechnikov and Kuznetsova [16] shows that the density of DMS systems down to 15^m with arbitrary q and A and component masses $M_1 \leq 2.8M_\odot$ and $M_2 \leq 1.5M\odot$ is 750×10^{-6} pc^{-3}, while the densities of the ∼CW and CW systems are 67×10^{-6} and 145×10^{-6} pc^{-3}, respectively. Thus, we estimate the jump in density from the low-mass detached systems in the feeding trapezoid to the precontact and contact systems to be $\rho_{DMS}/\rho_{\sim \mathrm{CW}+\mathrm{CW}} \approx 3.5$.

Thus, our analysis of Figs. 1, 2, and 3 confirms the reduced spatial density of systems with $A \leq 10R_\odot$ and enables us to identify a small area in Fig. 1 that corresponds to the precursors of W UMa contact systems. It is important that the limiting masses for the primaries of this type of star coincide with those predicted by the MSW formalism.

4. QUANTITATIVE TEST OF THE DMS → W UMa → BLUE STRAGGLER SCENARIO

4.1. Number of Blue Stragglers that Are Products of Mergers of DMS Systems

If we assume that all single blue stragglers are the products of mergers in W UMa contact systems, which, in turn, arise as a result of mergers of the components of low-mass detached systems due to their MSW, we can obtain theoretical estimates of the blue-straggler birth rate and the number of these stars in our Galaxy. Since blue stragglers can be most reliably identified in globular clusters of various masses, it is convenient to work with the ratio of the number of blue stragglers to the number of horizontal-branch (HB) stars in a cluster rather than the absolute number of blue stragglers. Since the lifetimes of HB stars are "fixed" ($\sim 10^8$ yr), their number reflects their birth rate. The lifetime of a blue straggler is determined by its mass, and the ratio of the number of blue stragglers (N_{BS}) to the number of HB stars (N_{HB}) ultimately reflects the ratio of their birth rates.

To estimate the blue-straggler birth rate, we will use the birth function for Galactic close binaries derived from stars in the solar neighborhood [37]:

$$d^3\nu = 0.2 d\log\frac{A}{R_\odot}\left(\frac{M_1}{M_\odot}\right)^{-2.5} d\frac{M_1}{M_\odot}dq \ \text{year}^{-1}, \quad (8)$$

where ν is the close-binary birth rate per Galaxy, A is the initial orbital semimajor axis, M_1 is the initial mass of the primary, and q is the initial component-mass ratio. This function assumes that $10 \leq A/R_\odot \leq 10^6$ for essentially all stars, at least for binaries, as has been confirmed by recent studies. A study of binarity among M dwarfs [38] showed that more than half were binary systems with $10^2 \leq A/R_\odot \leq 10^6$ ($dN \sim d\log A$). A study of stars in the young cluster ρ Oph [39] demonstrated that 24% were visual binaries with $3 \times 10^3 \leq A/R_\odot \leq 3 \times 10^4$. These data confirm the earlier estimate (8) of the frequency of binarity and the character of the binaries' distribution over their orbital semimajor axes.

If we now suppose that all blue stragglers are the products of mergers of initially detached components of close binaries from the feeding trapezoid in Fig. 1 due to the action of the components' MSW, Fig. 1 indicates that their birth rate in our Galaxy should be $\nu \sim 0.2 d\log A \approx 0.02$/year. It is interesting that, if the distribution of initial component-mass ratios is given by (8), a significant fraction of the merger products will have masses exceeding $\sim 1.5M_\odot$, and thus will be unable to slow their rotation via their MSW. This could lead to the formation of an extended circumstellar gas and dust disk, with the subsequent formation of a planetary system in this disk [40]; about 10% of all planetary systems could be formed in this way [41].

In order for an HB star with a mass of $\sim 1M_\odot$ to form, it must have no close companions, i.e., the condition $3 \leq \log A/R_\odot \leq 6$ must be satisfied. Together with (8), this condition yields an estimate for the formation rate of HB stars in our Galaxy of

~ 0.6/year. Given the characteristic lifetimes of HB stars, $\sim 10^8$ yr, there should be $N_{HB} \sim 6 \times 10^7$ such stars in the Galaxy. Horizontal-branch and so-called extreme HB stars must be distinguished here. Most of the latter ($\sim 70\%$) are cooling helium-dwarf components of close binaries [42], and some of these stars are helium nondegenerate dwarfs that are the products of mergers of degenerate helium dwarfs. As a rule, they can be distinguished from genuine HB stars on the basis of their positions in the Hertzsprung–Russell (HR) diagram. The formation of blue stragglers in the course of mergers of degenerate helium dwarfs due to the radiation of gravitational waves is negligible [43].

To estimate the number of blue stragglers in globular clusters, we must take into account the fact that the range of initial close-binary semimajor axes producing blue stragglers narrows to $\log A \approx 0.1$ if the masses of stars leaving the main sequence in these clusters are $\sim 0.8 M_\odot$ (Fig. 1). Assuming the masses of the merger products are $\sim 1.6 M_\odot$ and their lifetimes are 2.5×10^9 yr, we find their formation rate to be ~ 0.01 (Fig. 1), in which case $N_{BS} \sim 2.5 \times 10^7$. Even with all the uncertainties, the resulting ratio, $N_{BS}/N_{HB} \approx 0.4$, coincides with the observed ratio for globular-cluster stars, $N_{BS}/N_{HB} \approx 0.1$–1 [44].

Let us discuss some consequences of this result. First, it is important to estimate the role of the Algol mechanism in the formation of blue stragglers in globular clusters, including the effect of conservative mass transfer between the components. Rare examples of such systems are known. An eclipsing blue straggler with an orbital period of ~ 0.64 d was found in NGC 2354 [45], and another (NJL5), in ω Cen [46]. However, such systems are probably exceptions. Were they typical, their formation rate would have to be comparable to the formation rate of HB stars, as follows from (8). Since the lifetime of a blue straggler is longer than that of an HB star by more than a factor of ten, this would unavoidably lead to high ratios in globular clusters, $N_{BS}/N_{HB} \approx 20$–30, which are not observed [44]. The mean value of N_{BS}/N_{HB} is almost two orders of magnitude lower [44], indicating a low probability that the Algol scenario operates (~ 0.01); this mechanism probably occurs in rare cases when a donor with a mass of $\sim 0.8 M_\odot$ that fills its Roche lobe has a small ($\leq 0.1 M_\odot$) degenerate helium core that prevents the components from merging under the action of the MSW. At the same time, the components in such a system are close enough for the MSW to play an active role [47], working against the increase of the system's orbital period. As a result, the system evolves with a nearly constant orbital period of ~ 0.5–1 day [47].

A detailed analysis of N_{BS}/N_{HB} [44] revealed a correlation, albeit with a considerable dispersion, between this ratio and the luminosity of the parent globular clusters:

$$\frac{N_{BS}}{N_{HB}} \approx 3000 \left(\frac{L_\nu}{L_\odot} \right)^{-\frac{3}{4}}, \qquad (9)$$

where L_ν is the globular cluster's integrated visual luminosity. There may also be a correlation between N_{BS}/N_{HB} and the central brightness (density) of the cluster, with N_{BS}/N_{HB} decreasing as the cluster density increases [44]. This cannot be the result of collisions due to close passages of stars, since the typical distance for the closest passages of cluster stars over the Hubble time is several astronomical units, whereas the typical semimajor axes of the close-binary precursors of blue stragglers are almost two orders of magnitude smaller (Fig. 1).

Let us consider two possible explanations for the observed correlations of N_{BS}/N_{HB} with the cluster mass and density. First, we can see in Fig. 1 that the range of semimajor axes of the blue-straggler feeding zone rapidly narrows as the stellar mass at the turn-off point of the HR diagram decreases. In other words, the relative number of blue stragglers should decrease with increasing cluster age: older clusters, whose stars at the turn-off point have lower masses, possess a smaller feeding zone containing blue-straggler precursors. However, there is no known correlation between globular cluster ages and their luminosities (masses), and this possibility remains open for further study.

Another possible explanation for the discussed correlation is related to the lower boundary of the feeding trapezoid in Fig. 1. Its position is ultimately determined by the density of the parent cluster [48], which determines the rate of accretion by a young star as it is forming and, hence, its radius. The radius of an accreting convective star of mass M at the Hayashi limit is $R \sim \rho^{1/6} M^{1/3}$ [40], where ρ is the protostar's initial density. This density should naturally be correlated with the current cluster density. As a result, the largest radii of young stars in denser clusters, and probably in more massive and brighter globular clusters, are larger than the radii of young stars in sparse clusters. Therefore, the lower boundary of the trapezoid in Fig. 1 could be higher for dense clusters, leading to a narrower range of initial semimajor axes for blue-straggler-producing systems. De Angeli and Piotto [44] found a slight tendency for the ratio N_{BS}/N_{HB} to decrease with increasing values of $l_c^3 r_c$, where l_c is the central brightness and r_c is the core radius of the cluster. This provides evidence for a possible dependence of this ratio on the cluster density, but this requires further investigation.

Blue stragglers have been known since the construction of the first HR diagrams reaching the main-sequence turn-off. Several possible explanations for the origin of blue stragglers were suggested [49], including mass transfer between components of close binary systems, collisions [50, 51], and component mergers. We have shown above that mergers of the components of low-mass close binaries due to the action of their MSW are sufficient to explain the observed numbers of blue stragglers in globular clusters. Despite the existing example of Algol-type systems [45, 46], mass transfer between evolved close-binary components is probably a rare exception among blue stragglers. Collisions of stars in dense globular-cluster cores, especially exchange collisions between massive stars and close binaries, are an efficient mechanism that probably creates the majority of low-mass X-ray systems in these clusters. In principle, together with the action of the MSW, this mechanism is capable of forming some fraction of blue stragglers. However, two things make it unlikely that this is the main scenario for these stars' formation. First, the relative numbers of blue stragglers in globular clusters, N_{BS}/N_{HB}, shows no correlation with the rate of collisions [44]. Second, close binaries formed in collisions have no "genetic" limit of $6(M_1/M_\odot)^{1/3}$ for their semimajor axes [37, 40]. Therefore, all systems with masses in excess of $\sim 0.3M_\odot$, and hence with MSWs, can merge over the Hubble time and, as a result, form W UMa stars [13] with primary masses down to $0.3M_\odot$ and orbital periods down to ~ 0.1 days. However, according to the extensive study [25], no such W UMa stars with periods shorter than 0.3 days exist, and stars with longer orbital periods can be explained by the action of an MSW that moves the close binary components away from the "genetically" determined limit for their semimajor axes (1). These arguments lead us to adopt this last mechanism as the main one forming W UMa stars.

Now comes the question of the fate of blue stragglers. A component merger significantly increases the rotation rate of the merger product. Rapid rotation has indeed been observed for one blue straggler in a globular-cluster core [52]. The rotation rate of this star, which has a mass of $1.7M_\odot$, is $v \sin i \approx 160$ km/s. It is obvious that a merger product can get rid of excess angular momentum in several ways. If its mass is below $1.5M_\odot$, the most efficient mechanism for slowing its rapid rotation is the MSW, while the most efficient mechanism when the blue straggler's mass is higher than $\sim 1.5M_\odot$ is the formation of a circumstellar decretion disk that transfers angular momentum to the extended gas and dust disk surrounding the star. It is also possible that planets or brown dwarfs can form in this disk. If a blue straggler is a member of a close binary with a period of ≤ 10 days, the blue straggler can get rid of its excess rotation via the spin–orbital interaction [53]. This is possible in the case of an initial triple system.

4.2. W UMa Systems

The obvious observational selection effects—their eclipses and the high efficiency of modern automated methods for variable-star searches—are favorable for finding W UMa-type contact systems, so that these systems should be widely represented in catalogs of close binaries. A study of the distribution of orbital periods for 1621 contact systems of this type showed that the vast majority were in the range 0.3–0.6 day [25]. Since both components of such systems are usually similar to initial main-sequence stars [54], assuming an average mass of $2.5M_\odot$, we can deduce masses for their primaries of 1–$2M_\odot$, which nearly coincides with the mass range for the contact systems shown in the figures in [55]. This again confirms on the basis of a large statistical database the mass limits for contact systems formed in mergers of close-binary components via the action of their MSW.

We can use (2) to estimate the typical lifetime (merging time) for the components of W UMa systems due to the action of the MSW. Here, we assume that $A \sim 2.5R_\odot$ and $R_1/R_\odot \sim M_1/M_\odot$, as is valid for stars with $M_1 \leq 1.5M_\odot$. The resulting lifetime is $\sim 10^8$ yr, independent of the system's mass. This estimate does not differ significantly from the value of [15], $\sim 5 \times 10^8$ yr. The lifetimes of such stars can also be estimated in other ways. According to the data of Rucinski [56] on 32 contact systems, with the "true" density restored from the luminosity function, the observed local density of W UMa stars is $\sim 10^{-5}$ pc^{-3}. This is an order of magnitude lower than our estimate, 1.5×10^{-4} pc^{-3}, due to our attempt to take into account various observational selection effects (the geometrical and photometric detection probabilities, detection volumes, sample-incompleteness factors) individually for each of 304 contact systems. For a volume of the Galaxy of $\sim 10^{11}$ pc^3, such densities yield the estimate $\sim 10^6$–10^7 for the total number of W UMa stars. Further, taking into account their formation rate, shown above to be $\sim 10^{-2}$/year, we find their lifetimes to be 10^8–10^9 yr. Another means to estimate this lifetime follows from the statistics of blue stragglers and W UMa stars in globular clusters. A study of 14 globular clusters [57] demonstrated that there were about 50 blue stragglers per W UMa star. Since the formation rates of these objects are the same

in the standard scenario, the ratio of their numbers should be equal to the ratio of their lifetimes. Adopting the lifetime ~ 3–7×10^9 yr for the blue stragglers, we find a lifetime for the W UMa stars of $\sim 6 \times 10^7$–1.4×10^8 yr. The scatter in these estimates is not surprising, given the considerable uncertainties in the input parameters. It is important for us that this time ($\sim 3 \times 10^8$ yr) is much shorter than the lifetime of the primary on the main sequence. This provides additional evidence for a critical role of the MSW in the evolution of W UMa stars.

5. CONCLUSIONS

This paper has been devoted to an analysis of the distribution of close binaries in the semimajor axis—primary mass plane and a study of the evolution of close binaries under the influence of their components' MSW. Modern data on the observed properties of close binaries with orbital semimajor axes smaller than $\sim 50R_\odot$ (Fig. 1) have enabled us to confirm the reduced spatial density of stars with $A \leq 10R_\odot$. This provides evidence for an absence of close binaries with such semimajor axes among young binaries due to limits on the sizes of young stars [40].

As follows from Fig. 1, most stars with smaller component separations have primary masses in the range 0.8–$2M_\odot$. Their existence is due primarily to the action of the MSW of the components, which also determines the evolution of cataclysmic systems and low-mass X-ray binaries [40], as well as the braking of the rotation of single stars [7]. The loss of angular momentum in close binaries with initial semimajor axes of ~ 6–$10R_\odot$ leads to the formation of contact W UMa systems. According to semiempirical estimates, the lifetimes of such stars are only several hundred million years, much shorter than their nuclear evolution time scale. The merger products are blue stragglers in open and globular clusters. The observed number of blue stragglers relative to the number of HB stars in globular clusters is close to the theoretical estimate in the scenario we have considered, confirming the relevance of this scenario.

The most massive systems (1.5–$3M_\odot$) have no MSW and can therefore rotate with rates that are close to the limiting values. In the absence of other braking mechanisms, this can lead to the formation of decretion disks, line emission, and ultimately the possible formation of planetary systems [41].

The limitation of the semimajor axes of young solar-mass close binaries to $\sim 8R_\odot$ (Fig. 1) prevents the formation at the end of these systems' evolution of helium degenerate dwarfs in close binaries with combined component masses below $\sim 0.4M_\odot$. The reason for this is simple. To rule out a critical role for the MSW in a system's evolution, the radius of the star filling its Roche lobe must exceed $\sim 4R_\odot$, with the mass of the solar-mass star's degenerate helium core at that time exceeding $\sim 0.2M_\odot$ [13]. This means that the combined mass of the closest binary of degenerate helium dwarfs must exceed $\sim 0.4M_\odot$. In fact, the modern catalog [58] containing 29 degenerate dwarf pairs includes no systems with a combined component mass below $\sim 0.5M_\odot$. The absence of a clear dependence of the degenerate-dwarf cooling curve on time [59] and obvious observational selection effects that prevent the detection of low-mass degenerate dwarfs suggests that this effect is related to the action of the MSW.

ACKNOWLEDGMENTS

This work was supported by the Russian Foundation for Basic Research (project codes 02-02-17524 and 03-02-16254) and the Federal Scientific and Technological Program "Astronomy."

REFERENCES

1. E. Schatzman, Ann. Astrophys. **25**, 18 (1962).
2. S. S. Huang, Ann. Astrophys. **29**, 331 (1966).
3. L. Mestel, Mon. Not. R. Astron. Soc. **138**, 359 (1968).
4. I. Roxburgh, Astrophys. J. **143**, 111 (1966).
5. F. van Veer, Astron. Astrophys. **80**, 287 (1979).
6. O. Vilhu, Astron. Astrophys. **109**, 17 (1982).
7. A. Skumanich, Astrophys. J. **171**, 565 (1972).
8. R. E. Wilson, Astrophys. J. **234**, 1054 (1979).
9. F. van Veer, Veroff. Rem. Sternwarte Bamberg **11**, 388 (1977).
10. J. M. Kreiner, in *IAU Coll. No. 42: The Interaction of Variable Stars with their Environment,* Ed. by R. Kippenhahn and W. Strohmeier (Remeis-Sternwarte, Bamberg, 1977), p. 393.
11. E. I. Popova, A. V. Tutukov, and L. R. Yungel'son, Pis'ma Astron. Zh. **8**, 297 (1982) [Sov. Astron. Lett. **8**, 160 (1982)].
12. A. E. Tutukov, A. Fedorova, and L. R. Yungel'son, Pis'ma Astron. Zh. **8**, 365 (1982) [Sov. Astron. Lett. **8**, 198 (1982)].
13. I. J. Iben and A. V. Tutukov, Astrophys. J. **284**, 719 (1984).
14. R. F. Webbink, Astrophys. J. **209**, 829 (1976).
15. T. Rahunen, Astron. Astrophys. **102**, 81 (1981).
16. S. Mochnacki, Astrophys. J. **245**, 650 (1981).
17. M. Mateo, H. Harris, J. Nemec, and E. Olszewski, Astron. J. **100**, 469 (1990).
18. M. A. Svechnikov and E. F. Kuznetsova, *Catalog of Approximate Photometrical and Absolute Elements of Eclipsing Variables* (Izd. Ural. Gos. Univ., Ekaterinburg, 1990), Vols. 1 and 2 [in Russian].
19. L. Spitzer, in *IAU Symp. No. 6: Electromagnetic Phenomena in Cosmic Physics,* Ed. by B. Lehnert (Cambridge Univ. Press, Cambridge, 1958), p. 169.

20. E. J. Weber and L. Davis, Astrophys. J. **148**, 217 (1967).
21. M. A. Svechnikov, *Catalog of Orbital Elements, Masses, and Luminosities of Close Binary Stars,* Uchsh. Zapiski Uralsk. Gos. Univ., Ser. Astron. **5** (88) (1969).
22. Z. T. Kraĭcheva, E. I. Popova, A. V. Tutukov, and L. R. Yungel'son, Astron. Zh. **55**, 1176 (1978) [Sov. Astron. **22**, 670 (1978)].
23. M. Staniucha, Acta Astron. **29**, 587 (1979).
24. M. A. Svechnikov and L. I. Snezhko, *Non-Stationary Events and Stellar Evolution* (Nauka, Moscow, 1974), Chap. 5, p. 181 [in Russian].
25. M. Szymanski, M. Kubriak, and A. Udalski, Acta Astron. **51**, 259 (2001).
26. J. Greiner, New Astron. Rev. **44**, 149 (2000); astro-ph/9906011.
27. I. Iben and A. Tutukov, Astrophys. J. **342**, 430 (1989).
28. S. Qian, Mon. Not. R. Astron. Soc. **328**, 914 (2001).
29. B. Carney, D. W. Latham, J. B. Laird, *et al.,* Bull. Am. Astron. Soc. **33**, 1311 (2001).
30. N. E. Kurochkin, in *Methods of Variable Star Research*, Ed. by V. B. Nikonov (Nauka, Moscow, 1971), p. 11 [in Russian].
31. M. A. Svechnikov, O. V. Eretnova, M. N. Ol'neva, and T. A. Taĭdakova, Nauchn. Inform. Astrosoveta Akad. Nauk SSSR **67**, 15 (1989).
32. M. A. Svechnikov and O. V. Eretnova, in *Astronomical and Geodetical Research* (Ekaterinburg, 1995), p. 115 [in Russian].
33. M. A. Svechnikov and O. V. Eretnova, Astron. Tsirk., No. 1552, 17 (1992).
34. L. F. Istomin, *Stellar Clusters and Binary Systems* (Ekaterinburg, 1978) [in Russian].
35. L. F. Istomin, Candidate's Dissertation in Physics and Mathematics (1986).
36. G. N. Dremova and M. A. Svechnikov, Astron. Zh. **78**, 248 (2001) [Astron. Rep. **45**, 212 (2001)].
37. E. I. Popova, A. V. Tutukov, and L. R. Yungelson, Astrophys. Space Sci. **88**, 155 (1982).
38. D. A. Simon, T. J. Henry, and J. P. Kirkpatrick, Astron. J. **112**, 2238 (1996).
39. M. Barsony, C. Koresko, and T. Matthews, astro-ph/0303595.
40. A. G. Masevich and A. V. Tutukov, *Stellar Evolution: Theory and Observations* (Nauka, Moscow, 1988) [in Russian].
41. A. V. Tutukov, Zemlya Vselenn., No. 4, 17 (2000).
42. P. Maxted, U. R. Heber, T. R. Marsh, and R. C. North, Mon. Not. R. Astron. Soc. **326**, 1391 (2001).
43. A. V. Tutukov and L. R. Yungel'son, Astron. Zh. **79**, 738 (2002) [Astron. Rep. **46**, 667 (2002)].
44. F. De Angeli and G. Piotto, astro-ph/0303292.
45. E. Laposset and J. Ahumada, Astron. Astrophys. **314**, 448 (1996).
46. B. E. Helt, H. E. Jorgensen, S. Ring, and A. Larsen, Astron. Astrophys. **270**, 297 (1993).
47. A. Fedorova and A. V. Tutukov, Astron. Zh. **71**, 431 (1994) [Astron. Rep. **38**, 377 (1994)].
48. A. V. Tutukov, Pis'ma Astron. Zh. **9**, 160 (1983) [Sov. Astron. Lett. **9**, 86 (1983)].
49. P. Leonard, Astrophys. J. **470**, 521 (1996).
50. J. R. Hurley, C. A. Tout, S. J. Aarseth, and O. R. Pols, Mon. Not. R. Astron. Soc. **323**, 630 (2001).
51. J. C. Lombardi, J. S. Warren, F. A. Rasio, *et al.*, Astrophys. J. **568**, 939 (2002).
52. R. A. Saffer, M. M. Shara, and M. Livio, Bull. Amer. Astron. Soc. **29**, 807 (1997).
53. A. M. Cherepashchyuk and V. G. Karetnikov, Astron. Zh. **80**, 42 (2003) [Astron. Rep. **47**, 38 (2003)].
54. J. Kaluzny, Acta Astron. **35**, 313 (1985).
55. C. Maceroni and F. van Veer, Astron. Astrophys. **311**, 523 (1996).
56. S. Rucinski, Publ. Astron. Soc. Pac. **114**, 1124 (2002).
57. S. Rucinski, Astron. J. **120**, 319 (2000).
58. R. Napiwotski *et al.*, private communication.
59. I. Iben, Jr. and A. Tutukov, Astrophys. J. **311**, 742 (1986).

Translated by N. Samus'

Astronomy Reports, Vol. 48, No. 3, 2004, pp. 229–235. Translated from Astronomicheskiĭ Zhurnal, Vol. 81, No. 3, 2004, pp. 255–261.

The Influence of High-Energy Neutrinos on the Ejection of the Envelope of a Type-II Supernova

I. V. Baikov and V. M. Chechetkin

Keldysh Institute of Applied Mathematics, Moscow, Russia

Received August 17, 2003; in final form, September 18, 2003

Abstract—We have derived the qualitative dependence of the ejection energy in a type-II supernova on the regime of accretion onto the central body, including the influence of high-energy neutrinos on the ejection energy. We have also obtained a qualitative picture for the behavior of the shock that leads to the ejection of the envelope as a function of the accretion regime and the character of the neutrino emission. These results are necessary for the construction of effective multidimensional models for supernovae, which we are in the process of developing. © *2004 MAIK "Nauka/Interperiodica"*.

1. INTRODUCTION

A fully comprehensive theory of type-II supernova explosions has not yet been developed. There remains the question of the mechanism for ejection of the envelope, including the source of the energy transferred to the ejected envelope and the transfer mechanism itself. The nuclear energy, which reaches about 1% of the rest mass, is not sufficient to eject matter from the surface of a neutron star, where the gravitational potential energy is up to 20% of the rest mass. The rotational energy before the onset of instability does not exceed 5% of the gravitational energy [1] and for a number of reasons is not sufficient to eject envelopes with the observed kinetic energies of up to 10^{52} erg [2]. The gravitational energy of the collapsing core of the presupernova when it attains the nuclear density is up to 10^{53} erg for an object with a mass of the order of the solar mass. This could be the necessary source of the envelope-ejection energy, but the mechanism for transporting this energy to the envelope remains unclear.

Due to these physical problems, previous studies have not led to a fully successful model of a type-II supernova (see, e.g., [2–4]). The model of [5, 6], which considers the energy of the neutrinos from the neutrinosphere of the neutron star, likewise did not yield satisfactory results. Other models did not result in the ejection of an envelope with the required energy due to energy losses from the shock front due to the escape of neutrinos and the decay of nuclei [7, 8].

During the collapse of the iron core of a star, most of the gravitational energy of the nascent neutron star is carried away by neutrinos. The ejection of an extended envelope requires the transfer of some of this energy to the outer layers of the star by an efficient and rapidly acting mechanism. In the classical study by Colgate and White [9], this was accomplished by neutrino transport, assuming that the matter is transparent to neutrinos. However, as was shown by Imshennik and Nadezhin [10], at densities exceeding 10^{12} g/cm^3, the escape of neutrinos is determined by the opacity of the matter (and the time scale for diffusion of the neutrinos is much larger than the envelope lifetime). In [11], we considered neutrino transport from the core by means of large-scale convection, with the rise time of a so-called "bubble"—region of enhanced entropy—to the surface of the core being much shorter than the neutrino diffusion time scale. The size of the bubbles for high central densities of the matter is such that their optical depth to high-energy neutrinos exceeds unity, making it possible to partially trap neutrinos inside the bubbles and transport them to the surface until the bubbles become completely optically thin to neutrinos.

Despite the huge amount of work that has been done on this problem, it is not completely clear what flux of neutrinos can result during the ejection of the supernova envelope. It is evident that this physical phenomenon must be studied using three-dimensional hydrodynamical models that take into account the most important physical processes. However, such models require large computational resources and "good" initial conditions. Therefore, before undertaking three-dimensional computations, it is necessary to estimate, at least qualitatively, the influence of neutrino transport on the propagation of the shock that ultimately results in the ejection of the envelope and in the supernova phenomenon.

The aim of the present paper is to derive a qualitative description of the behavior of the shock as it

1063-7729/04/4803-0229$26.00

is "heated" by high-energy neutrinos emitted by the proto-neutron core.

2. FORMULATION OF THE PROBLEM

Let us consider the following formulation of the problem. We assume that a young proto-neutron star is already formed and the accretion of the envelope occurs in a free-fall regime with velocity v_0. The profile of the accretion velocity will be described in accordance with the Bondi solution for the Newtonian gravitational potential:

$$\rho(r) = \frac{\dot{M}}{4\pi}\frac{r^{3/2}}{v_0\sqrt{GM}}, \qquad v(r) = -v_0\sqrt{\frac{GM}{r}},$$

where $v_0 \in (0, \sqrt{2})$ is a parameter that determines the accretion rate ($v_0 = \sqrt{2}$ corresponds to the free-fall velocity), ρ is the density, M is the mass, and r is the radial coordinate.

This initial state is steady; i.e., for "historical" boundary conditions at both the outer and inner boundaries, the initial state does not change. The flux of matter through a spherical surface, equal to $4\pi\rho v r^2$, is time-independent and is constant throughout the computational domain. This assertion was directly verified via the computations and served as a test for the code used.

The computational domain was bounded by a rigid "wall" that models the cessation of the infall of the matter during the collision with the surface of the neutron star. As a result, a shock is formed and propagates outward through the infalling matter. The profile of the shock was very similar to that found in [7, 8]. The energy of the shock in this case can be sufficient for the ejection of the envelope [7, 8]; however, energy losses due to the decay of nuclei and neutrino losses from the shock front due to the high temperature there substantially weaken the shock [10], and it cannot eject the envelope without an additional influx of energy.

This raises the problem of supporting the amplitude of the shock via external sources of energy that can compensate for the energy losses. The energy of the neutrinos emitted by the proto-neutron star can serve as one such energy source [9]. As is noted above, the neutrinos can carry away a considerable fraction of the gravitational energy; i.e., for a core mass of the order of a solar mass, the total energy can be $E \approx 3\times10^{53}$ erg. For various radiation rates, the neutrino luminosity can vary from $L_\nu = 5\times10^{50}$ erg/s to $L_\nu = 2\times10^{53}$ erg/s. Following [12], we will adopt the value $L_\nu = 5\times10^{52}$erg/s. Neutrino heating is included as a source in the right-hand side of the energy equation. The source is assumed to have the form [13]

$$\frac{dq}{dt} = 7.3\times10^{31}\frac{\mathrm{erg}}{\mathrm{s}\cdot\mathrm{g}}\left(\frac{L_\nu}{r^2}\left[\frac{\mathrm{erg}}{\mathrm{s}\cdot\mathrm{cm}^2}\right]\right)(T_\nu - T)T,$$

where T_ν is the neutrino temperature, which was taken to be 30 MeV in the first set of computations and 60 MeV in the second set, following [11, 12].

Energy losses via neutrino emission from the shock front were taken into account by the factor [14]

$$\frac{dq}{dt} = -1.9\times10^{25}\frac{\mathrm{erg}}{\mathrm{s}\cdot\mathrm{g}}\left(\frac{T^9}{\rho}\right).$$

The decay of nuclei at the shock front, which also results in energy losses, was not taken into account.

The computational domain covered the region from 50 to 2000 km. The computational grid had 4001 cells.

To numerically solve this system of equations, we write it in the following conservative form for the case of spherical symmetry:

$$\frac{\partial\mathbf{U}}{\partial t} + \frac{1}{r^2}\frac{\partial r^2\mathbf{F}}{\partial r} = \mathbf{S},$$

$$\mathbf{U} = \begin{pmatrix}\rho\\ \rho v\\ \rho E\end{pmatrix}, \qquad \mathbf{F} = \begin{pmatrix}\rho v\\ \rho v^2 + P\\ \rho v h\end{pmatrix},$$

$$\mathbf{S} = \begin{pmatrix}0\\ 2\dfrac{P}{r} - \rho g\\ \rho v g + \rho\dfrac{dq}{dt}\end{pmatrix},$$

where $h = E + P/\rho$ is the enthalpy. Here, $\mathbf{U}$ is the vector of the variables, $\mathbf{F}$ is the vector of the fluxes in the r direction, and $\mathbf{S}$ is the source vector, which takes into account gravity and neutrino processes.

All physical quantities in the problem were assigned a dimensionless form. The density was taken in units of $\rho_0 = 2\times10^8$ g/cm^3; the length, in units of $r_s = 2\times10^7$ cm; and the mass, in units of $M_\odot = 2\times10^{33}$ g. As the scales for the time (t_0), velocity (v_0), temperature (T_0), and energy (E_0), we adopted

$$t_0 = \sqrt{\frac{r_s^3}{GM_\odot}} = 7.74\times10^{-3}\ \mathrm{s},$$

$$v_0 = \sqrt{\frac{GM_\odot}{r_s}} = 2.583\times10^9\ \mathrm{cm/s},$$

$$T_0 = \frac{P_0}{\rho_0 R} = 7\times10^{10}\ \mathrm{K},$$

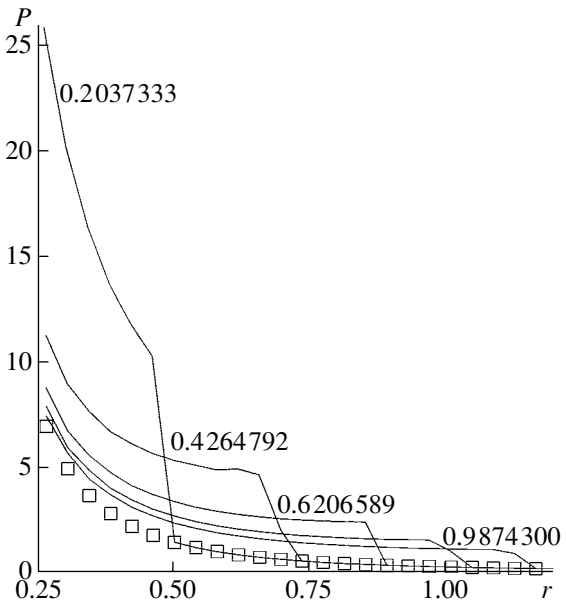

Fig. 1. Profiles of the dimensionless pressure for the model with $\dot{M} = 0.2$ and $v_0 = 0.7$ in the absence of neutrinos escaping the core. The values of the dimensionless time are indicated by the curves. The squares show the initial state.

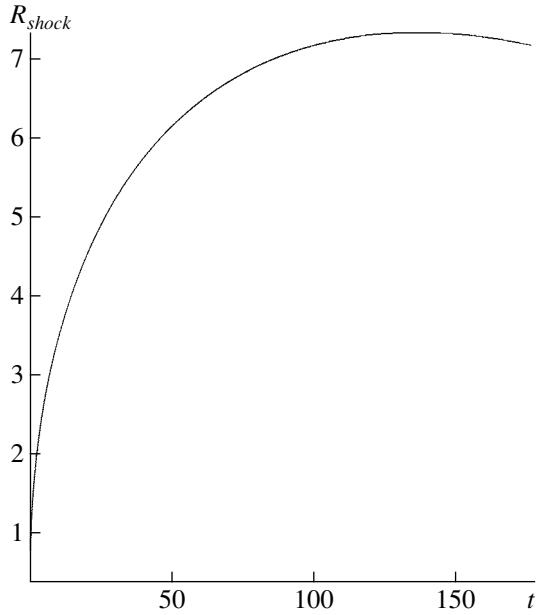

Fig. 2. Position of the shock in the model with $\dot{M} = 0.2$ and $v_0 = 0.7$ in the absence of neutrinos escaping the core. We can see that the shock begins to move backward.

$$E_0 = \frac{GM_\odot}{r_s}\rho_0 = 5.166 \times 10^{17}\ \mathrm{erg/cm^3}.$$

The integration was carried out using an explicit, conservative, second-order TVD scheme [15–18]. The motion through time was carried out using a third-order Runge–Kutta method that preserved the conservative form of the scheme and did not increase the total variation of the solution at each time step.

The outer boundary conditions were assumed to be "historical"; i.e., the parameter values corresponding to the initial time were retained. This is justified by the circumstance that physical quantities must retain their initial values in front of the shock, making historical boundary conditions the most suitable. Such conditions would hinder the propagation of the shock through the outer boundary, but this does not pose a problem for us, since it is sufficient for the shock to reach the boundary. Thus, the computations were stopped when the shock reached the outer boundary of the computational domain.

At the inner boundary, the specific energy and density of the matter in the two edge cells (with numbers 1 and 2) were computed assuming that their gradients remain constant:

$$\frac{x_i - x_{i-1}}{dr} = \frac{x_{i+1} - x_i}{dr}.$$

Due to the uniform step in r, this yields

$$x_{i-1} = 2x_i - x_{i+1}.$$

The velocity at the inner boundary was set to zero, mimicking reflection of the matter from the core.

3. RESULTS OF THE COMPUTATIONS

We carried out several sets of computations for this physical model for the interaction of the neutrinos and shock. Our aim was to determine the influence of heating by the neutrinos on the propagation of the shock and the possibility of ejecting the envelope. We adopted a steady infall of matter onto the accreting center as an initial condition. We varied the velocity of the infalling matter v_0 and the amount of accreted matter $\dot{M}$; $4\pi\dot{M}$ is the mass flowing through unit area of the spherical surface per unit time. We performed two series of computations, for neutrino energies of 30 and 60 MeV, with the total energy being the same in both cases. We put a "wall" in the path of the infalling matter at a distance of 50 km from the center of the star (corresponding to the radius of the proto-neutron star) for a certain time:

$$v_1 = 0, \quad v_2 = 0.$$

The density and energy were computed according to the formulas

$$\rho_2 = 2\rho_3 - \rho_4, \quad \rho_1 = 2\rho_2 - \rho_3 = 3\rho_3 - 2\rho_4,$$
$$E_2 = 2E_3 - E_4, \quad E_1 = 2E_2 - E_3 = 3E_3 - 2E_4,$$

where the subscript 1 corresponds to the first cell in the grid and the subscript 3 corresponds to the first

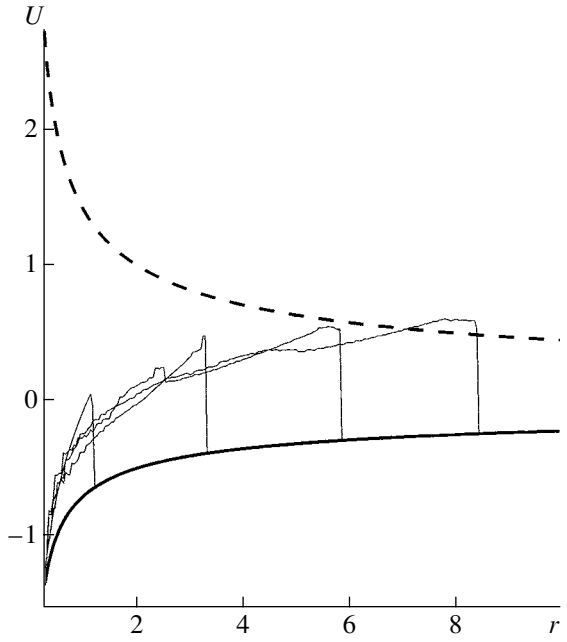

Fig. 3. Profiles of the dimensionless velocity for the model with $\dot{M} = 0.8$ and $v_0 = 0.7$. The initial state is shown by the thick curve. The dashed curve shows the escape velocity. The neutrino temperature is $T_\nu = 30$ MeV.

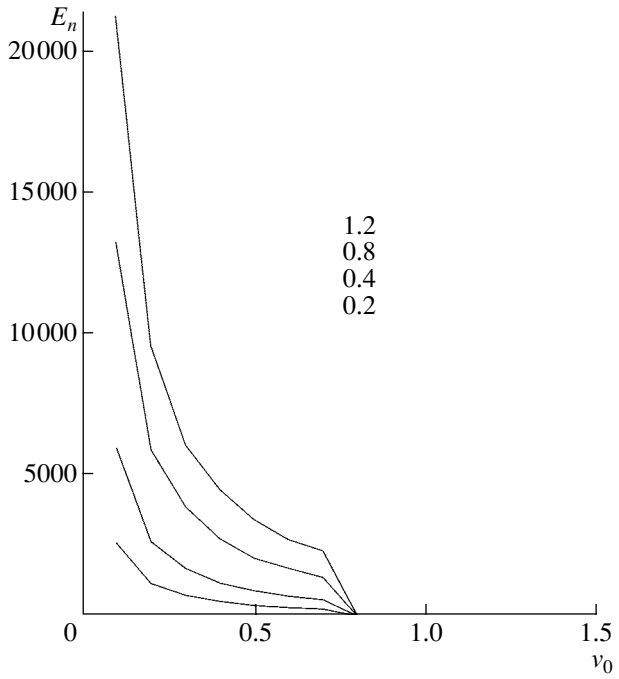

Fig. 4. Energy of the matter with velocities exceeding the escape velocity when the shock reaches the outer boundary as a function of the parameter v_0. The upper plot corresponds to the computations with $\dot{M} = 1.2$; the lower plot, to those with $\dot{M} = 0.2$; and the middle plot, to those with $\dot{M} = 0.8$ and $\dot{M} = 0.4$. The neutrino temperature is $T_\nu = 30$ MeV.

computational cell. These formulas describe the inner boundary condition.

In this way, the matter falling onto the accreting center collides with the stellar surface, forming a shock wave with characteristics close to those found in [7, 8].

Thus, the outer boundary condition is historical, with the values of physical quantities remaining fixed at their initial values, while a shock wave forms at the inner boundary and begins to propagate outward. The development of the shock for the model with $\dot{M} = 0.2$ and $v_0 = 0.7$ is shown in Fig. 1.

We can see from Fig. 1 and Fig. 2, which shows the position of the shock front, that this shock is not able to eject the envelope. Moreover, in a number of cases, it is not able to propagate beyond a certain critical radius. More accurate modeling of the collapse using a more complex equation of state shows that the shock is transformed into an accreting wave. This does not happen in our computations, first and foremost, due to our non-self-consistent formulation of the problem and our use of a simple equation of state. However, the main aim of our computations was to investigate the influence of neutrinos on the shock and the probability of envelope ejection.

Figure 3 shows the computational results for the models with $\dot{M} = 0.8$ and $v_0 = 0.7$ and with neutrino heating. We can see that some fraction of the matter attains velocities exceeding the parabolic velocity. In accordance with [11], the neutrinos begin to escape approximately $t_\nu = 10$ ms after the formation of the proto-neutron core (or, in dimensionless units, at time $\tilde{t}_\nu \approx 1.3$). The impulse lasts for about $\tau = 25$ ms, and the time between the surfacing of the bubbles is about $\tau = 15$ ms. The assumed neutrino temperature in this series of computations was $T_\nu = 30$ MeV. Up to time $\tilde{t}_\nu$, the behavior of the shock is the same as in the case without neutrinos, but it changes after the neutrinos are "switched on." Figures 4 and 7 show the energies of particles with velocities exceeding the escape velocity. We do not show similar plots for the case without neutrinos, since this energy is then equal to zero.

Figure 5 shows the dependence of the maximum radial advance of the shock on the velocity of the accreting matter. The plot corresponds to the computations with $\dot{M} = 1.2$, but it remains nearly unchanged as the accreting mass is varied, as is expected for our choice of the initial state. When $v_0 < 0.8$, the shock advances to the outer border, while it does not when $v_0 > 0.8$. There is a critical velocity separating these two regimes near $v_0 = 0.8$. Given our formulation of the problem, there is no sense in computing this

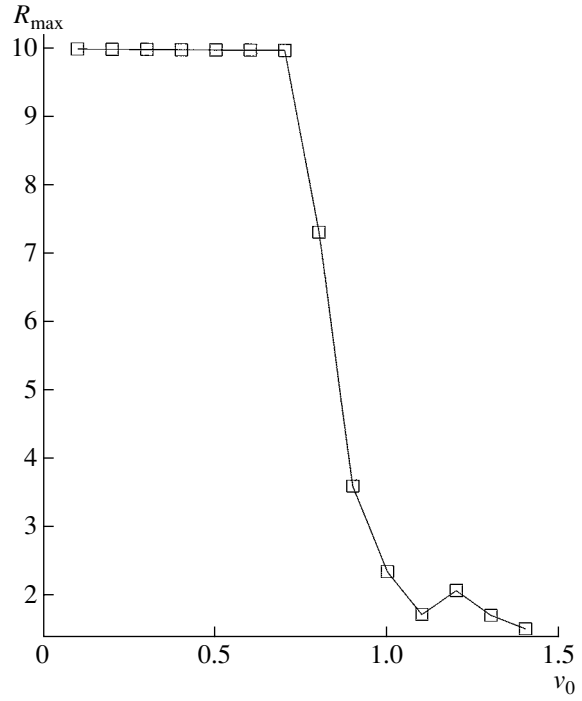

Fig. 5. Dependence of the maximum distance of the shock's propagation on the parameter v_0 for the computations with $\dot{M} = 1.2$. The neutrino temperature is $T_\nu = 30$ MeV.

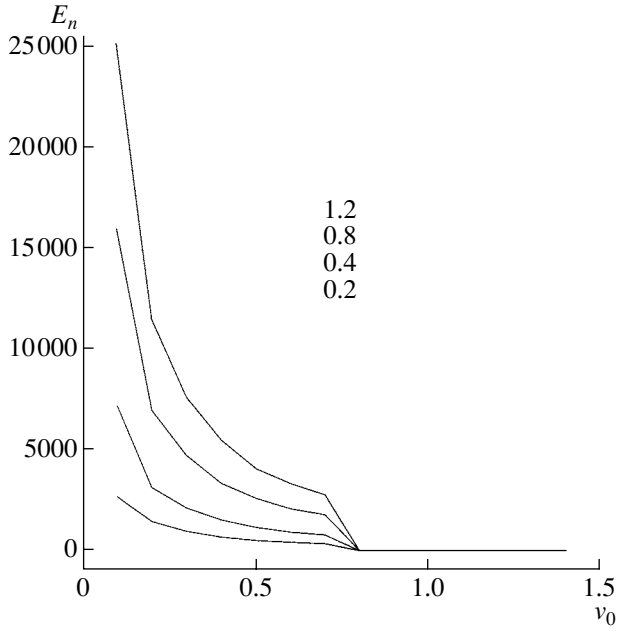

Fig. 6. Same as Fig. 4 for a neutrino temperature of $T_\nu = 60$ MeV.

value more precisely; it is much more important to understand that such a critical value exists.

This circumstance indicates that there exists a limiting velocity for the infalling matter and that this critical velocity, above which ejection of the envelope is unlikely, is virtually independent of the amount of matter falling onto the core.

In the next set of computations, we raised the temperature of the emitted neutrinos to $T_\nu = 60$ MeV (Figs. 6, 7).

Figures 4 and 6 show the dependence on v_0 of the energy of the matter with velocities exceeding the escape velocity at the time when the shock reaches the outer boundary of the computational domain for various values of $\dot{M}$. Figure 4 shows the results for $T_\nu = 30$ MeV, and Fig. 6, the results for $T_\nu = 60$ MeV. A comparison of these two plots shows that doubling the energy of the neutrinos increases the energy of the ejected matter by no more than 20%.

Thus it is evident that we did not introduce significant errors by adopting a constant neutrino temperature. It is also noteworthy that the maximum distance of advance of the shock is nearly the same in the two cases.

Tables 1 and 2 present the energy of the matter with velocities exceeding the escape velocity when the shock reaches the outer boundary of the computational domain. The velocity v of the infalling matter is given in units of $v_0 = 2.583 \times 10^9$ cm/s; the energy, in units of $E_0 = 5.166 \times 10^{17}$ erg/cm^3; and the accret-

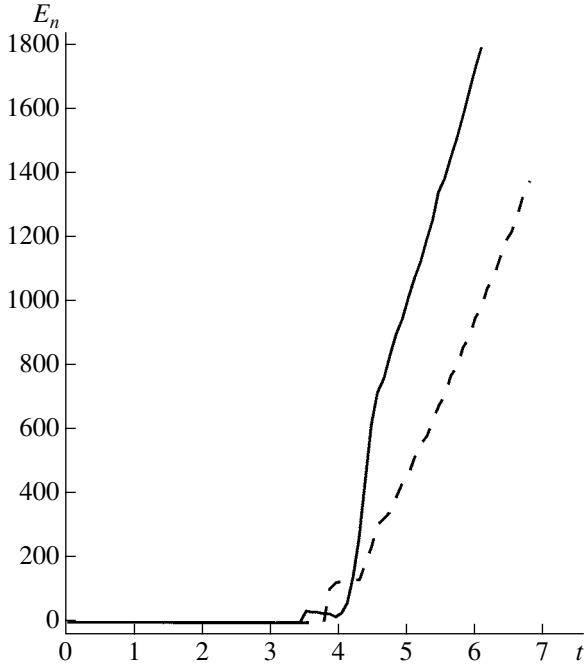

Fig. 7. The energy of the matter with velocities exceeding the escape velocity for the models with $\dot{M} = 0.8$ and $v_0 = 0.7$. The solid curve is for $T_\nu = 60$ MeV and the dashed curve is for $T_\nu = 30$ MeV.

Table 1. Computations with $T_\nu = 30$ MeV

v	$\dot{M}$			
	0.2	0.4	0.8	1.2
	E			
0.1	2600	6000	13 000	21 100
0.2	1100	2800	6000	9800
0.3	1000	2000	4000	6000
0.4	800	1500	2800	4500
0.5	500	1000	2000	3800
0.6	400	800	1800	2800
0.7	380	700	1500	2200
0.8	0	0	0	0
0.9	0	0	0	0

Table 2. Computations with $T_\nu = 60$ MeV

v	$\dot{M}$			
	0.2	0.4	0.8	1.2
	E			
0.1	3000	6300	16 000	25 050
0.2	1800	3000	7000	11 300
0.3	1100	2100	4900	7500
0.4	900	1800	3200	5200
0.5	850	1150	2800	4100
0.6	700	900	2100	3100
0.7	450	800	1800	2800
0.8	0	0	0	0
0.9	0	0	0	0

ing mass, in solar masses. Tables 1 and 2 correspond to the computations with neutrino energies of $T_\nu =$ 30 MeV and 60 MeV.

The results clearly demonstrate that the neutrinos play a substantial role in the model of the envelope ejection (collapse) during the supernova explosion. The numbers in the tables show differences in the expected ejection energy for different accretion regimes. We showed above that there exists a limiting velocity for the infalling matter, above which ejection of the envelope is unlikely; judging from all our results, this limit depends only weakly on the amount of accreted matter and, more interestingly, on the neutrino energy, while the ejection energy does depend on these parameters.

However, as we noted above, we can expect to obtain a plausible picture of the supernova explosion only via self-consistent three-dimensional modeling that allows for neutrino losses. It was shown in [11] that bubbles rising to the surface of the proto-neutron star due to convection can emit neutrinos that were trapped in deep layers of the star. Since the star is rotating, the bubbles should form and rise predominantly along the rotational axis. Because there is no reason to suppose that one or the other direction along the axis is preferred, it is most likely that two bubbles moving along the axis in opposite directions will rise to the surface. This suggests that the density of the neutrino emission will be higher close to the rotation axis and that the ejection of the matter will, accordingly, also be nonuniform.

One-dimensional hydrodynamical computations including neutrino losses were carried out in [19–21], where it was shown that neutrino emission has the effect of supporting the deflagration front. However, the one-dimensional models computed in various studies have not produced ejected envelopes during the formation of the neutron star.

These circumstances make it clear that reasonable models of the explosions must be at least two-dimensional. However, before attempting to solve a multidimensional problem that requires vastly more computational resources, we must understand under what conditions envelope ejection is most probable. Our present study has enabled us to obtain a qualitative picture of the influence of the accretion rate and the character of the neutrino emission on the expected ejection. Our results can play an important role in our ongoing development of a multidimensional model that takes into account the asymmetry of the emission of high-energy (20–70 MeV) neutrinos from the core, the diffusion of low-energy (5 MeV) neutrinos, and energy losses from the shock front due to neutrinos and the decay of nuclei.

ACKNOWLEDGMENTS

This work was supported by the Ministry of Industry and Science (grant NSh-1029.2003.3) and the Russian Foundation for Basic Research (project no. 03-02-16548).

REFERENCES

1. J.-L. Tassoul, *Theory of Rotating Stars* (Princeton Univ. Press, Princeton, 1978; Mir, Moscow, 1982).
2. *Supernovae and Supernova Remnants* (Cambridge Univ. Press, 1996).
3. J. R. Wilson and R. W. Mayle, Phys. Rep. **227**, 97 (1993).

4. H.-Th. Janka and E. Muller, Astron. Astrophys. **306**, 167 (1996).
5. A. Burrows and B. A. Fluxell, Preprints of Steward Obs., No. 1124.
6. A. Burrows, T. Young, Ph. Pinto, *et al.*, Preprints of Steward Obs., No. 1520.
7. K. A. van Riper and J. M. Lattimer, Astrophys. J. **249**, 270 (1981).
8. K. A. van Riper, Astrophys. J. **257**, 793 (1982).
9. S. A. Colgate and R. H. White, Astrophys. J. **143**, 626 (1966).
10. V. S. Imshennik and D. K. Nadezhin, Zh. Éksp. Teor. Fiz. **63**, 1548 (1972).
11. V. M. Suslin and G. P. Churkina, Astron. Zh. **78**, 280 (2001) [Astron. Rep. **45**, 241 (2001)].
12. V. M. Chechetkin, S. D. Ustyugov, A. A. Gorbunov, and V. I. Polezhaev, Pis'ma Astron. Zh. **23** (1997) [Astron. Lett. **23**, 30 (1997)].
13. T. Shimizu, T. Ebisuzaki, K. Sato, and S. Yamada, Astrophys. J. **552**, 756 (2001).
14. W. Fowler and F. Hoyle, *Nucleosynthesis in Massive Stars and Supernovae* (Univ. of Chicago Press, Chicago, 1965; Mir, Moscow, 1967).
15. O. A. Kuznetsov, Preprint No. 29 (Inst. Appl. Math. RAS, 1992).
16. P. Glaistner, J. Comput. Phys. **74**, 382 (1988).
17. P. L. Poe, Ann. Rev. Fluid Mech. **18**, 337 (1986).
18. P. K. Sweby, J. Numer. Anal. **21**, 995 (1984).
19. L. N. Ivanova, V. S. Imshennik, and V. M. Chechetkin, Astron. Zh. **54**, 354 (1977) [Sov. Astron. **21**, 197 (1977)].
20. L. N. Ivanova, V. S. Imshennik, and V. M. Chechetkin, Astron. Zh. **54**, 661 (1977) [Sov. Astron. **21**, 374 (1977)].
21. L. N. Ivanova, V. S. Imshennik, and V. M. Chechetkin, Astron. Zh. **54**, 1009 (1977) [Sov. Astron. **21**, 571 (1977)].

Translated by L. Yungel'son

Astronomy Reports, Vol. 48, No. 3, 2004, pp. 236–245. Translated from Astronomicheskiĭ Zhurnal, Vol. 81, No. 3, 2004, pp. 262–271.

Light Curve and Neutrino Spectrum Emitted during the Collapse of a Nonrotating, Supermassive Star

A. N. Baushev and G. S. Bisnovatyĭ-Kogan

Space Research Institute, ul. Profsoyuznaya 84/32, Moscow, Russia

Received May 26, 2003; in final form, August 8, 2003

Abstract—The formation of a neutrino pulse emitted during the relativistic collapse of a spherical supermassive star is considered. The free collapse of a body with uniform density in the absence of rotation and with the free escape of the emitted neutrinos can be solved analytically by quadrature. The light curve of the collapsing star and the spectrum of the emitted neutrinos at various times are calculated. © *2004 MAIK "Nauka/Interperiodica".*

1. INTRODUCTION

The properties of a neutrino pulse arising during the spherically symmetrical collapse of a supermassive star into a black hole have been considered in a number of studies, the earliest of which were carried out nearly 40 years ago [1]. It was shown in [2] that, in general, the asymptotic time dependence of the total luminosity of the star has the form

$$I \propto \exp\left(-\frac{ct}{3\sqrt{3}r_g}\right).$$

The propagation of photons outside a nonrotating collapsing star was considered in detail in [3]. The brightness distribution across the visible disk and the time dependence of the stellar spectrum were obtained for late stages of the collapse. The results of numerical computations of the light curve and the spectrum of a nonrotating, collapsing star are presented by Shapiro [4, 5], who computed the propagation of photons inside the star in a diffusion approximation taking into account general relativistic effects. The propagation of photons to a distant observer is also treated in detail in [4]. Estimates of the parameters of the spectrum and of the total intensity of a neutrino pulse arising during the collapse of a supermassive state were obtained in [6]. The possibility of detecting such a pulse using modern detectors was analyzed, and the general background of neutrinos arising as a result of explosions of supermassive stars was estimated. The results of relativistic hydrodynamical computations of the collapse of a nonrotating, supermassive star are presented in [7], together with temperature and density profiles for the matter inside the star at various times. However, the propagation of the neutrinos was computed using a very simple scheme; it was essentially assumed that the neutrinos propagated instantaneously. In addition, all general relativistic effects were neglected.

Thus, in spite of the abundance of publications on the topic, the properties of neutrino pulses arising during the collapse of supermassive stars are not fully understood. As a rule, previous papers have either considered very simple models for this phenomenon that have admitted exact solutions (as in [1]), constructed very detailed models that have required the use of approximation computational methods, or have neglected certain physically important effects. For example, the propagation of the neutrinos is taken to be instantaneous in [7], and gravitational forces are not taken into account. Such an approach is clearly not justified physically. During the collapse of a supermassive star, the temperature of the matter grows as the collapse proceeds; accordingly, the neutrino-loss rate in a comoving frame also grows, reaching its highest values in the late stages of the collapse. The drop in the radiation intensity at the end of the collapse is due exclusively to gravitational effects: the gravitational redshift and time dilation. Thus, the shape of the light curve is determined by the battle between two competing processes: the increase in the brightness of the star due to heating and the decrease in its brightness due to gravitational effects. In addition, the characteristic time scale for the collapse r_g/c is comparable to the time for a neutrino to travel a distance equal to the radius of the star. Under such conditions, the neglect of gravitational effects and of the neutrino-propagation time is completely unjustified. Ordinary (not supermassive) stars were considered in [5]; these computations included all general relativistic effects, but the propagation of the neutrinos inside the star was treated in an Eddington approximation, which cannot be formulated

1063-7729/04/4803-0236$26.00

unambiguously inside the star, where the effects of sphericity are appreciable.

The aim of the current paper is to construct a model for the neutrino emission radiated by a supermassive star that can yield as accurate a solution as possible, including all general relativistic effects, while simultaneously providing a good description of a real collapsing star. The light curve and spectra obtained with this model should display all the main properties characteristic of the light curves and spectra of real collapsing supermassive stars, while the simplicity of the model enables us to understand the dependence of the parameters of the neutrino impulse on the parameters of the problem. As we will show below, by introducing a number of natural constraints on the parameters of the problem, we can obtain a solution by quadrature.

2. DYNAMICS OF THE COLLAPSE

We introduce a number of assumptions about the physical parameters of the collapse that simplify the computations. Most importantly, the star is taken to be nonrotating and the distribution of matter to be uniform at all times. In addition, we neglect completely the influence of the pressure on the motion of the matter; i.e., the dynamics of the collapse are taken to be the same as for a sphere of dust. We also assume that the matter is heated according to a power law as a result of compression.

Our neglect of the pressure is a rather crude approximation at the onset of the collapse, but the temperature of the matter is still modest at this stage, and few neutrinos are radiated. As the star approaches its gravitational radius r_g, the influence of the pressure tends to zero, so that it indeed becomes negligible.

As is shown in [8], inside a homogeneous dust sphere that is shrinking or expanding, it is possible to introduce a comoving, synchronous coordinate system in which ordinary three-dimensional space has the same curvature everywhere, which depends only on time. The character of this curvature (positive, negative, zero) does not change in the course of the collapse and is uniquely specified by the initial conditions (initial density and velocity). We will take the three-dimensional space inside the sphere to have zero curvature, which appreciably simplifies the computations without introducing large errors.

Let the initial radius of the star be x_0.[1] According to [8], the metric inside the dust sphere can be written as

$$ds^2 = d\tau^2 - a^2(\tau)[dR^2 + R^2(d\zeta^2 + \sin^2\zeta d\xi^2)], \quad (1)$$

where

$$a(\tau) = \left(1 - \frac{\tau}{\tau_{col}}\right)^{\frac{2}{3}}. \quad (2)$$

Here, τ_{col} is a parameter of the problem that is defined below and the "spatial" coordinates (R, ζ, ξ) are analogous to the usual spherical coordinates in three-dimensional space. The coefficient a plays the role of a scale factor: to find the physical distance between two points in the metric (1), we must multiply the "coordinate distance" [calculated in the coordinates (R, ζ, ξ)] by a. In particular, the distance from a point with radial coordinate R to the center of the star is

$$x = aR. \quad (3)$$

The coordinate system (τ, R, ζ, ξ) is comoving. This means that each element of the collapsing matter has some fixed R, ζ, and ξ that do not change in time. In this sense, (R, ζ, ξ) can be considered Lagrange coordinates.

Note the full analogy between the solution for a collapsing dust sphere considered here and the Friedmann solution for a flat universe filled with homogeneous dust, whose metric coincides fully with (1). Therefore, the inner space of the dust sphere can be considered part of a Friedmann universe; the motion of the neutrinos within the dust sphere occurs precisely as within a Friedmann universe.

In a comoving coordinate system, the radial coordinate R_s of the surface does not change and at any time $\tau < \tau_{col}$ is equal to its initial value

$$R_s = \frac{x_s}{a} = R_{s0} = \frac{x_{s0}}{a_0}. \quad (4)$$

In addition, it is straightforward to obtain the following relation using the results of [8]:

$$2\pi k\varepsilon = \frac{1}{3\tau_{col}^2 a^3}. \quad (5)$$

Here, k is the gravitational constant and ε is the density of the stellar matter in its rest frame. Integrating ε over the entire volume of the collapsing sphere yields the total rest mass of the stellar matter. It is of interest to determine how this quantity is related to the total mass of the star measured by a distant stationary observer. This latter mass consists of the rest mass of the matter and the sum of its kinetic and potential energy. As was noted above, we are considering the collapse of a dust sphere within which the three-dimensional curvature of space is zero. In this case, the motion of dust matter toward the center is a free fall with zero velocity at infinity. The sum of the kinetic

[1] Here and below, unless explicitly stated otherwise, we will work with a physical system of units in which $c = 1$ and $r_g = 2kM/c^2 = 1$, which specifies the units of velocity (c), length (r_g), and time (r_g/c).

and potential energy of matter undergoing such a free fall is zero. Therefore, the mass of the star is equal to the rest mass of its matter, i.e.,

$$M = \int \varepsilon dV. \tag{6}$$

Hence, taking into account also the homogeneity of the star, we have

$$\varepsilon = \frac{3M}{4\pi x_s^3}. \tag{7}$$

Combining this relation with (5) yields

$$\frac{3kM}{2x_s^3} = \frac{1}{3\tau_{col}^2 a^3}.$$

In other words, in accordance with (4),

$$kM = \frac{2R_s^3}{9\tau_{col}^2}. \tag{8}$$

Since in our units $r_g = c = 1$, it follows from the definition $r_g = 2kM/c^2$ that

$$kM = 1/2, \tag{9}$$

which yields

$$\frac{4R_s^3}{9\tau_{col}^2} = 1, \quad \tau_{col} = \frac{2}{3}R_s^{\frac{3}{2}}. \tag{10}$$

We will adopt the time $\tau = 0$ as the initial time. Then, $a_0 = 1$ and

$$x_{s0} = R_{s0} = R_s. \tag{11}$$

Having specified the initial radius of the star x_{s0}, we can use (10) to determine the collapse parameter τ_{col}. The collapse of a uniform sphere with a flat internal space involves two independent parameters: the Lagrange radius of the surface R_s and the mass of the star. The quantity $\tau_{col} - \tau_0$ is uniquely determined by these two parameters, and variations in τ_0 only shift the zero time. In the case of arbitrary three-dimensional curvature, we can arbitrarily specify the mass, initial radius, and initial collapse velocity of the star. If we consider a collapse with zero curvature, this is not possible, and the initial collapse velocity always differs from zero for a finite initial radius. This is automatically determined from the condition of zero curvature and turns out to be equal to the velocity for free fall from infinity for the radius x_{s0}. In the interest of conciseness, we will denote the initial radius of the star simply as x_0.

3. COMPUTATION OF THE RADIATION SPECTRUM IN A COMOVING FRAME

We will assume that each matter element emits neutrinos isotropically in a comoving frame and that the intensity and spectrum of the emitted neutrinos depend on the temperature and density of the matter. In our analysis, the dynamics of the collapse corresponds to the motion of the dustlike material. If the law for variations of the density and the parameters M and R_s is known, the variations of the temperature in the compressed matter can be found from the solution of the energy equation for a specified initial entropy using the known rate of neutrino emission as a function of the temperature and density. Below, we use a simplified approach in order to obtain an analytical solution, in which we approximate the time dependence of the temperature with a power-law dependence of the temperature on the density. The variations of the density of the matter $\varepsilon(\tau)$ are determined in accordance with (4) and (7) by the single function $a(\tau)$. To find the observed light curve and spectrum of the neutrinos, we must first determine the propagation toward the observer of a neutrino signal arising within a uniform collapsing body of a specified mass M.

We will suppose that

$$f(a,q)dV d^3p d\tau \tag{12}$$

neutrinos are emitted in an element of physical[2] volume dV in an element of physical phase space d^3p in an interval of proper time $d\tau$ in the element's rest frame, where $f(a,q)$ is some function whose form will be determined below.

We introduce the neutrino distribution function N[3] such that the quantity Nd^3pdV specifies the number of neutrinos in an element of physical volume dV in an element of physical phase space d^3p. In the spherically symmetric case with isotropic neutrino emission in the comoving frame, N depends on only four quantities: the radial coordinate R, the angle between the neutrino trajectory and the direction from the center of the star ϑ, the neutrino energy q, and time τ. In this case,[4] the kinetic equation can be written in the form [9]

$$\cos\vartheta\frac{\partial N}{\partial R} - \frac{\sin\vartheta}{R}\frac{\partial N}{\partial \vartheta} + \frac{2q}{3\tau_{col}\sqrt{a}}\frac{\partial N}{\partial q} - \frac{2\sqrt{a}}{3\tau_{col}}\frac{\partial N}{\partial a} = af(a,q). \tag{13}$$

[2] Not coordinate.

[3] We will call a quantity defined in this way a physical distribution function.

[4] We also apply here the condition of zero three-dimensional curvature of the space inside the star.

Here, the parameter a, which depends on time in accordance with (2), is used in place of the time τ. The characteristic system for this equation has the form

$$\frac{dR}{\cos\vartheta} = dy, \tag{14}$$

$$-\frac{Rd\vartheta}{\sin\vartheta} = dy, \tag{15}$$

$$\frac{3\tau_{col}\sqrt{a}dq}{2q} = dy, \tag{16}$$

$$-\frac{3\tau_{col}da}{2\sqrt{a}} = dy. \tag{17}$$

The solutions of this system determine the trajectories of individual neutrinos. Combining pairwise the equations for characteristic system (16) and (17), and also (14) and (15), we obtain the two first integrals:

$$A = aq, \tag{18}$$

$$B = R\sin\vartheta. \tag{19}$$

Combining (15) and (17) and using (19), we obtain the third, last, integral of the system (14)–(17):

$$C = 3\tau_{col}\sqrt{a} + R\cos\vartheta. \tag{20}$$

The physical meaning of these quantities can be elucidated based on the analogy between the solution for a collapsing dust sphere and the solution for a Friedmann universe. As was noted above, the motion of a neutrino is absolutely identical in these two cases; in particular, all three of the first integrals of system (14)–(17) are also valid in a Friedmann universe. The presence of integral (18), i.e., the fact that the product $a \cdot q$ is constant, leads to the appearance of a "redshift" in a Friedmann universe. As the parameter a increases (corresponding to the expansion of space), the energy of a neutrino along its trajectory decreases. In contrast, in our case we have a compression of a sphere, so that a decreases and the neutrino energy increases. Thus, we can think of our case as giving rise to a "violet shift."

Supermassive stars with masses exceeding $\sim 10^5 M_\odot$ have small optical depths to the absorption of neutrinos, which can be taken to propagate freely. Taking the radius of the star to be $R = nR_g = 2nGM/c^2$, we obtain expressions for the mean density,

$$\rho = \frac{3M}{4\pi R^3} = \frac{1.8\times 10^{16}}{n^3}\left(\frac{M_\odot}{M}\right)^2 \text{g/cm}^3,$$

and the optical depth to neutrino absorption,

$$\tau_\nu = 10^{-44}\rho R = \frac{33}{n^2}\frac{M_\odot}{M} \ll 1,$$

for $n \sim 3$, $M = 10^5 M_\odot$.

Let us elucidate the qualitative form of the characteristics determining system (14)–(17). The motion of photons and neutrinos is linear in a Friedmann universe. Indeed, integral (19) shows that a neutrino moves along straight lines in the (τ, R, ζ, ξ) coordinate frame. In addition, since this frame is comoving, the collapsing star can be represented at any time in this frame as a sphere with a constant radius R_s. The trajectory described by (14)–(17) proves to be a chord of this sphere. In accordance with the definition of the angle θ, the trajectory enters the sphere at some angle $\vartheta > \pi/2$ and leaves at an angle $\vartheta < \pi/2$. Proceeding from this property of the characteristic, it is straightforward to impose the appropriate boundary conditions for (13). For this, it is sufficient to specify the value of the function N at the surface of the star for angles $\vartheta > \pi/2$. We will assume that no neutrinos impact the star from outside, in which case

$$N|_{R=R_s} = 0 \quad \text{for} \quad \vartheta > \frac{\pi}{2}. \tag{21}$$

This is the boundary condition for (13).

We will denote the initial point of the characteristic and all related quantities with the subscript I and the final point and related quantities with the subscript II. Since both points are located on the surface of the collapsing sphere,

$$R_\text{I} = R_\text{II} = R_s. \tag{22}$$

Hence, we obtain using (19)

$$\sin\vartheta_\text{I} = \sin\vartheta_\text{II}. \tag{23}$$

Since $\vartheta_\text{I} > \pi/2$, $\vartheta_\text{II} < \pi/2$,

$$\cos\vartheta_\text{I} = -\cos\vartheta_\text{II}. \tag{24}$$

In addition, it follows from the existence of the integral (18) that

$$a_\text{I}q_\text{I} = a_\text{II}q_\text{II}, \quad \text{i.e.,} \quad a_\text{I} = a_\text{II}\frac{q_\text{II}}{q_\text{I}}. \tag{25}$$

Finally, writing integral (20), we obtain

$$3\tau_{col}\sqrt{a_\text{I}} + R_\text{I}\cos\vartheta_\text{I} = 3\tau_{col}\sqrt{a_\text{II}} + R_\text{II}\cos\vartheta_\text{II}. \tag{26}$$

Using relations (24) and (25), we obtain

$$\sqrt{a_\text{II}\frac{q_\text{II}}{q_\text{I}}} = \sqrt{a_\text{II}} + \frac{2R_s}{3\tau_{col}}\cos\vartheta_\text{II}, \tag{27}$$

$$q_\text{I} = \frac{q_\text{II}}{\left(1 + \dfrac{2R_s}{3\tau_{col}\sqrt{a_\text{II}}}\cos\vartheta_\text{II}\right)^2}. \tag{28}$$

Let us turn to the solution of (13) itself. We first take the neutrino-emission function (12) to be

$$f(a,q) = \lambda a^\beta \delta(q - q_0); \tag{29}$$

i.e., each element of matter in the proper frame radiates monochromatic neutrinos with energy q_0. Here,

λ and β are numerical parameters. Since (13) is linear, the resulting solution can easily be generalized to the case of a more complex function $f(a,q)$. We will discuss the form of this function for a real system and possible values of the power-law index β in more detail below.

For a neutrino-emission function of the form (29), Eq. (13) can be written in the form

$$\cos\vartheta\frac{\partial N}{\partial R}-\frac{\sin\vartheta}{R}\frac{\partial N}{\partial\vartheta}+\frac{2q}{3\tau_{col}\sqrt{a}}\frac{\partial N}{\partial q} \qquad (30)$$
$$-\frac{2\sqrt{a}}{3\tau_{col}}\frac{\partial N}{\partial a}=\lambda a^{\beta+1}\delta(q-q_0).$$

To solve this equation, we must integrate the right-hand side along the characteristic. Using boundary condition (21), we obtain for the surface of the collapsing sphere

$$N=\int_{\rm I}^{\rm II}\lambda a^{\beta+1}\delta(q-q_0)dy. \qquad (31)$$

We obtain using (18)–(28)

$$N=\int_{\rm I}^{\rm II}\frac{3}{2}\tau_{col}\lambda\frac{A^{\beta+\frac{3}{2}}}{q^{\beta+\frac{5}{2}}}\delta(q-q_0)dq \qquad (32)$$
$$=\frac{3}{2}\tau_{col}\lambda\frac{A^{\beta+\frac{3}{2}}}{q_0^{\beta+\frac{5}{2}}}\left(\Xi[q_{\rm II}-q_0]-\Xi[q_{\rm I}-q_0]\right).$$

Here, the function Ξ is defined to be

$$\Xi[x]=\begin{cases}0 & \text{for} \quad x<0,\\ 1 & \text{for} \quad x>0.\end{cases}$$

Note that quantities relating to the end of the characteristic are those that are measured by an observer located on the surface of the collapsing star. Therefore, we can omit the subscript"II." Substituting relations (18) and (28) into (32), we finally obtain

$$N=\frac{3}{2}\tau_{col}\lambda\frac{a^{\beta+\frac{3}{2}}q^{\beta+\frac{3}{2}}}{q_0^{\beta+\frac{5}{2}}} \qquad (33)$$
$$\times\left(\Xi[q-q_0]-\Xi\left[q-\left(1+\frac{2R_s}{3\tau_{col}\sqrt{a}}\right)^2q_0\right]\right).$$

This formula specifies the neutrino distribution function measured by an observer located on the surface of the star and moving with this surface.

4. PROPAGATION OF NEUTRINOS FROM THE STAR TO AN OBSERVER

Let us now consider the motion of the neutrinos outside the star. The gravitational field here is a Schwarzschild field [10]; i.e., it has the metric

$$ds^2=\left(1-\frac{1}{r}\right)dt^2-\left(1-\frac{1}{r}\right)^{-1}dr^2 \qquad (34)$$
$$-r^2(d\theta^2+\sin^2\theta d\phi^2).$$

The neutrino distribution function N in such a field in the spherically symmetrical case depends on four quantities: the angle between the neutrino trajectory and the direction from the center of the star θ, the neutrino energy w, the radius r, and the time t. We can find N by solving the kinetic equation, for which the boundary conditions must be obtained using (33). Let us determine the relationship between physical quantities measured on the surface of the star in the Friedmann and Schwarzschild reference frames. Local observers in the Schwarzschild frame are stationary, while local observers in the Friedmann frame move along with the stellar material. Therefore, physical quantities measured by such observers at some time at the same point on the stellar surface will be related by the usual Lorentz transformation. The velocity in this transformation is the physical velocity of the stellar surface measured by a local Schwarzschild observer, which will be equal to [10]

$$V=1/\sqrt{h}, \qquad (35)$$

where h is the current Schwarzschild radius of the star.

The circumference of the stellar surface in the Friedmann frame is $2\pi x$, and in the Schwarzschild frame, $2\pi h$. Since dimensions perpendicular to the motion are not changed by the Lorentz transformation, $2\pi x=2\pi h$, i.e., $x=h$. Thus, the Schwarzschild radius of the star is equal to x. In particular, (35) can be rewritten as

$$V=\frac{1}{\sqrt{x}}. \qquad (36)$$

As is shown in [8], the physical distribution function of the particles (see the comment on p. 6) is Lorentz invariant. Therefore, to recalculate function (33) in the Schwarzschild frame, we can simply express the variables $(q,\cos\vartheta)$ in terms of the quantities $(w_s,\cos\theta_s)$ in the Schwarzschild frame[5] using the Lorentz transformation and the velocity determined

[5] Here and below, the subscript s denotes variables in the Schwarzschild frame specified on the surface of the collapsing sphere.

by (36). Using the results of [8], it is straightforward to obtain the relations

$$q = w_s \frac{1 + V\cos\theta_s}{\sqrt{1-V^2}} = w_s \frac{\sqrt{x} + \cos\theta_s}{\sqrt{x-1}}, \qquad (37)$$

$$\cos\vartheta = \frac{\cos\theta_s + V}{1 + V\cos\theta_s} = \frac{\sqrt{x}\cos\theta_s + 1}{\sqrt{x} + \cos\theta_s}. \qquad (38)$$

Substituting (37) and (38) into (33), we finally obtain

$$N|_{r=x} = \frac{\lambda}{x_0^\beta} \frac{x^{\beta+\frac{3}{2}}}{q_0^{\beta+\frac{5}{2}}} \left(w_s \frac{\sqrt{x} + \cos\theta_s}{\sqrt{x-1}} \right)^{\beta+\frac{3}{2}} \qquad (39)$$

$$\times \left(\Xi \left[w_s - \left(\frac{\sqrt{x-1}}{\sqrt{x} + \cos\theta_s} \right) q_0 \right] - \Xi \Bigg[w_s - \left(\frac{\sqrt{x-1}}{\sqrt{x} + \cos\theta_s} \right) \left(1 + \frac{\sqrt{x}\cos\theta_s + 1}{\sqrt{x}\cos\theta_s + x} \right)^2 q_0 \Bigg] \right).$$

Thus, we have derived the physical neutrino distribution function on the stellar surface in the Schwarzschild frame. To fully specify the boundary conditions, we must determine an expression describing the motion of this surface. The equation for radial free fall of a body in a Schwarzschild field is such that the velocity of the body is zero at infinity [10] (as was indicated above, the surface of the dust sphere moves in precisely this way) and has the form

$$t = \ln\left(\frac{\sqrt{x}+1}{\sqrt{x}-1} \right) - \frac{2}{3}x^{\frac{3}{2}} - \sqrt{x} + D. \qquad (40)$$

Here, D is the constant of integration. By specifying this constant, we determine the zero time in the Schwarzschild frame. Setting D equal to zero, we obtain

$$t = \ln\left(\frac{\sqrt{x}+1}{\sqrt{x}-1} \right) - \frac{2}{3}x^{\frac{3}{2}} - \sqrt{x}. \qquad (41)$$

This formula describes the motion of the stellar surface. Thus, we have fully specified the boundary conditions for the kinetic equation in the Schwarzschild metric. The kinetic equation for such a field was obtained in [2], where it was shown that, in this case, the integrals of motion have the form

$$\rho = \frac{r\sqrt{r}}{\sqrt{r-1}} \sin\theta, \qquad (42)$$

$$\Omega = w \left(1 - \frac{1}{r} \right)^{\frac{1}{2}}, \qquad (43)$$

$$\xi = t - \int_{x(\xi)}^{r} \frac{z^2\sqrt{z}}{(z-1)\sqrt{z^3 - \rho^2(z-1)}} dz. \qquad (44)$$

The first of these quantities specifies the impact parameter in the Schwarzschild field, and the second determines the redshift for the motion of a neutrino in such a field. The third integral is essentially the time when the neutrino is emitted from the stellar surface. However, it will be more convenient for us to use in place of the time when the neutrino is emitted, ξ, the radius of the star at this time, x. It is obvious that these quantities are unambiguously related to each other in accordance with (41):

$$\xi = \ln\left(\frac{\sqrt{x}+1}{\sqrt{x}-1} \right) - \frac{2}{3}x^{\frac{3}{2}} - \sqrt{x}. \qquad (45)$$

Let us now express the quantities $\cos\theta_s$ and w_s in (39) in terms of the integrals of motion Ω, ρ, and x. We substitute the values of variables corresponding to the stellar surface into formulas (42)–(44) (in particular, we must set $r = x$). This yields

$$\rho = \frac{x\sqrt{x}}{\sqrt{x-1}} \sin\theta_s, \qquad (46)$$

$$\Omega = w_s \left(1 - \frac{1}{x} \right)^{\frac{1}{2}}. \qquad (47)$$

Hence,[6]

$$w_s = \sqrt{\frac{x}{x-1}}\Omega, \qquad (48)$$

$$\cos\theta_s = \frac{\sqrt{x^3 - \rho^2(x-1)}}{x\sqrt{x}}. \qquad (49)$$

Substituting the resulting expressions into formula (39) for the neutrino distribution function at the stellar surface,

$$N = \frac{2\lambda}{x_0^\beta} \frac{x^{\beta+\frac{3}{2}}\Omega^{\beta+\frac{3}{2}}}{q_0^{\beta+\frac{5}{2}} m^{\beta+\frac{3}{2}}} \left(\Xi\left[\Omega - mq_0\right] - \Xi\left[\Omega - g^2 mq_0\right] \right). \qquad (50)$$

Here, we have introduced the notation

$$u = \sqrt{x^3 - \rho^2(x-1)}, \quad m = \frac{x(x-1)}{x^2+u}, \quad g = 1 + \frac{x+u}{x^2+u}. \qquad (51)$$

Since the space outside the star does not contain any neutrino sources, the the distribution function is constant along the characteristics. Therefore, the resulting expression specifies the neutrino distribution at an arbitrary point outside the star.

[6] Since the surface of the collapsing star is moving, some neutrinos emitted from the surface have $\theta > \pi/2$ at the time they are emitted (as a consequence of the aberration of light). We do not take these into account when deriving (49). However, the fraction of such particles among those reaching a distant observer will be very small, so that we are quite justified in neglecting them.

However, we are ultimately interested in the parameters of a neutrino pulse that is measured by an observer infinitely distant from the collapsing star. Let the distance from the observer to the star be $d \gg 1$. Thus, we will be interested in the behavior of the integrals (42)–(44) for $r = d$, i.e., $r \gg 1$. The first two integrals, (42) and (43), acquire the form

$$\rho = d\sin\theta, \tag{52}$$

$$\Omega = w. \tag{53}$$

As is noted above, we use x in place of the integral ξ from system (42)–(44); these quantities are unambiguously related by (45). We substitute this relation into (44) and express the time t when the neutrino reaches the radius r in terms of x and ρ:

$$t = \ln\left(\frac{\sqrt{x}+1}{\sqrt{x}-1}\right) - \frac{2}{3}x^{\frac{3}{2}} - 2\sqrt{x} + \int_x^r \frac{z^2\sqrt{z}}{(z-1)\sqrt{z^3-\rho^2(z-1)}}dz. \tag{54}$$

We transform the integral in this formula by substituting r with d:

$$\int_x^d \frac{z^2\sqrt{z}}{(z-1)\sqrt{z^3-\rho^2(z-1)}}dz = d + \ln(d-1) - x - \ln(x-1) + \int_x^d \frac{z}{z-1}\left[\frac{z\sqrt{z}}{\sqrt{z^3-\rho^2(z-1)}} - 1\right]dz. \tag{55}$$

The last integral in this expression converges as $d \to \infty$. Therefore, it is natural to set the upper limit equal to infinity. However, we can see that the initial integral of (55) diverges. To elucidate the physical meaning of this fact, we substitute relation (55) into the initial formula (54):

$$t = d + \ln(d-1) - 2\ln(\sqrt{x}-1) - \frac{2}{3}x^{\frac{3}{2}} - 2\sqrt{x} - x + \int_x^\infty \frac{z}{z-1}\left[\frac{z\sqrt{z}}{\sqrt{z^3-\rho^2(z-1)}} - 1\right]dz. \tag{56}$$

We can see that the divergence of (55) leads to an unlimited growth in the arrival time of the neutrino to the observer as the distance to the observer approaches infinity. A similar behavior shown by function (54) is quite natural. However, it is clear that such a dependence for the neutrino arrival time on the distance to the observer has absolutely no effect on the light curve or the observed spectrum; it only affects the arrival time of the neutrino pulse. Therefore, we can shift the zero time for an infinitely distant observer by $d + \ln(d-1)$; i.e., we make the substitution

$$t^* = t - d - \ln(d-1). \tag{57}$$

Substituting this value into (54), we obtain

$$t^* = -2\ln(\sqrt{x}-1) - \frac{2}{3}x^{\frac{3}{2}} - 2\sqrt{x} - x + \int_x^\infty \frac{z}{z-1}\left[\frac{z\sqrt{z}}{\sqrt{z^3-\rho^2(z-1)}} - 1\right]dz. \tag{58}$$

This expression relates the parameters t^*, x, and ρ of some phase trajectory. It can be considered a specification of the integral of motion x in the form of an implicit function $x(\rho, t^*)$ of the impact parameter ρ and the time t^* of the arrival of the neutrino to a distant observer. Everywhere below, by x, we will mean precisely this function. Note that, since t^* is a function only of x and ρ, i.e., of integrals of the motion, it is also an integral of the motion.

Now, using (52) and (53), we can readily find the number of neutrinos with energies in the interval $[w, w+dw]$ passing through a sphere of radius d over a time dt^*. This quantity can be expressed in terms of the distribution function N as follows:

$$\Phi_0(w, t^*) = 8\pi^2 w^2 \int \rho N(w, \rho, x(\rho, t^*))d\rho, \tag{59}$$

where the integration is over all ρ values admissible for a given t^* and w. Here, we have taken into account the equality of Ω and w that follows from (53).

Having integrated (59) over the energy, we can obtain an expression for the light curve:

$$E_0(t^*) = 8\pi^2 \int\int \rho w^3 N(w, \rho, x(\rho, t^*))d\rho dw. \tag{60}$$

We now substitute in the resulting expressions the distribution function (50) and transform them into the form

$$\Phi_0(w, t^*) = 8\pi^2\lambda\frac{q_0}{x_0^\beta}\left(\frac{w}{q_0}\right)^{\beta+\frac{7}{2}} \times \int \rho\left(\frac{x}{m}\right)^{\beta+\frac{3}{2}}\left[\Xi(w - mq_0) - \Xi(w - g^2 mq_0)\right]d\rho, \tag{61}$$

$$E_0(t^*) = 8\pi^2\lambda\frac{q_0^2}{x_0^\beta}\int\int \rho\left(\frac{w}{q_0}\right)^{\beta+\frac{9}{2}} \times \left(\frac{x}{m}\right)^{\beta+\frac{3}{2}}\left[\Xi(w - mq_0) - \Xi(w - g^2 mq_0)\right]d\rho dw = \frac{8\pi^2\lambda}{\left(\beta+\frac{11}{2}\right)}\frac{q_0^3}{x_0^\beta}\int \rho m^4 x^{\beta+\frac{3}{2}}(g^{2\beta+11} - 1)d\rho. \tag{62}$$

In all these formulas, integration over ρ is understood to mean integration over all values of ρ for which there

exists a solution to (58) for a given t^*. The resulting formulas specify the desired analytical solution for the source function of the form (29).

5. APPLICATION OF THE MODEL TO THE COLLAPSE OF A REAL STAR

We can use our model to compute the light curve and spectrum of a real collapsing star. We take the mass of the star to be $M = 10^5 M_\odot$. Since the intensity of the neutrino emission by the stellar matter grows with temperature, which, in turn, grows as the star is compressed, it is expedient to consider only the last stages of the collapse, when the vast majority of neutrinos are emitted. We therefore take the initial radius to be $x_0 = 10$.

Let us now consider the heating of the stellar matter during the compression. In our model, this matter is taken to be dust, which, of course, does not change its temperature as it is compressed. Therefore, the law describing the temperature variations of the matter must be specified separately. We will assume that the matter is heated like an ideal gas during an adiabatic compression:

$$T/\varepsilon^{\gamma-1} = \text{const}. \tag{63}$$

Here, T is the temperature of the matter and ε is its density. For a relativistic gas (radiation), $\gamma = 4/3$. In addition, it follows from (5) that $\varepsilon \propto a^{-3}$. Therefore, we can rewrite formula (63) in the form

$$aT = \text{const}. \tag{64}$$

Denoting the initial temperature of the matter T_0 (and using the fact that $a_0 = 1$), we finally obtain the formula

$$T = T_0/a. \tag{65}$$

The parameters for which a star loses its stability were derived in [11], in a study of the evolution of massive stars. If we suppose that the subsequent compression is adiabatic and that the influence of the pressure can be neglected, we can use the parameters presented in [11] to estimate the density and temperature when the radius of the collapsing star is equal to x_0. We obtain $\varepsilon_0 = 2 \times 10^3$ g cm^{-3} and $T_0 = 3 \times 10^9$ K.

Let us now consider the physical processes occurring up to the radiation of neutrinos by the heated matter. As was shown in [12, 13], the main mechanism for the radiation of neutrinos during the collapse of a supermassive star is the annihilation of electron–positron pairs. In this case, the energy radiated per unit volume of matter per unit time is specified by the very simple formula [6][7]

$$Q \simeq 4 \times 10^{-66} T^9 \ \text{g cm}^{-3}\,\text{s}^{-1}, \tag{66}$$

where the temperature is in Kelvin. Hence, $\beta = -9$. When finding the light curve, the energy distribution of the neutrinos is not important and we can take all the emitted neutrinos to have the same energy, q_0. In this case, the function $f(q, a)$ in (12) corresponding to the radiation intensity (66) and the parameters of the star presented above is given by

$$\tilde{f}(a, q) = \frac{2 \times 10^{29}}{q_0^3} a^\beta \delta(q - q_0). \tag{67}$$

We thus obtain using (62)[8]

$$E(t^*) = 4 \times 10^{60} \int \frac{\rho m^4}{x^{15/2}} (1 - g^{-7}) d\rho \ \text{erg s}^{-1}. \tag{68}$$

This formula specifies the desired light curve.

Let us now consider the spectrum of the neutrinos. The spectrum of neutrinos generated during pair annihilations was calculated using Monte Carlo simulations in [6]; under the conditions of interest to us, the shape of this spectrum is approximated well by the formula

$$L(q) \propto \frac{(q/T)^2}{1 + \exp\left(\dfrac{q}{1.6T} - 2\right)}, \tag{69}$$

where L is the energy radiated per unit volume of matter per unit time in a unit interval of energy. We can see that the shape of the spectrum depends on the temperature. However, we will assume that temperature variations affect only the total intensity of the radiation, leaving the spectrum unchanged; i.e., the spectrum's shape will correspond to that for some fixed temperature E_0:

$$L(q) \propto \frac{(q/E_0)^2}{1 + \exp\left(\dfrac{q}{1.6E_0} - 2\right)}. \tag{70}$$

It is reasonable to choose the parameter E_0 so that it is approximately equal to the temperature of the matter when the luminosity of the star is maximum. We will take this parameter to be equal to the temperature of the matter when $x \simeq 1.43 r_g$; i.e., $E_0 = 7T_0$ in our case.

Thus, using expression (66) for the total intensity of the radiation, we can readily show that the function $f(q, a)$ in (12) is

$$f(a, q) = \frac{1.44 \times 10^{107}}{q\left(1 + \exp\left(\dfrac{q}{1.6E_0} - 2\right)\right)} a^{-9}. \tag{71}$$

[7] Expressions (66), (68), and (74) are written in the cgs system.

[8] Note that, during the calculations, all quantities in (68) and (74) must be taken in the system of units in which $c = 1$ and $r_g = 2kM/c^2 = 1$. The transition to cgs units is carried out via the numerical coefficient preceding the formula.

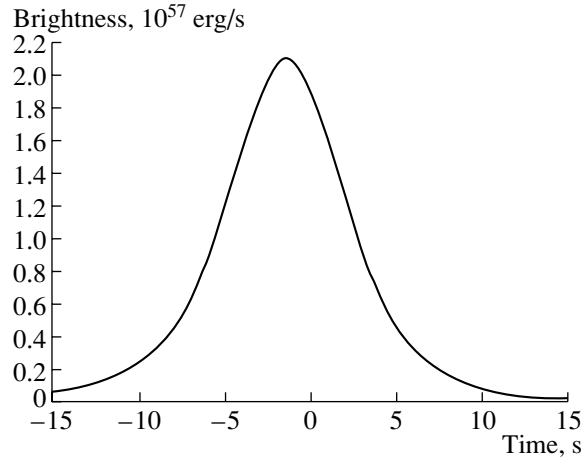

Fig. 1. Neutrino light curve. The time in the plots is the time t^* for an infinitely distant observer whose zero time has been shifted in accordance with (57). For more detail about the choice of zero time for a distant observer, see the text following formula (53).

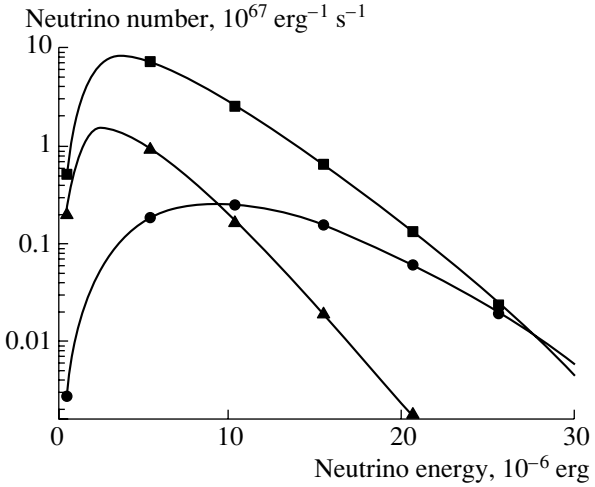

Fig. 2. Spectra of the neutrinos at times $t^* = -10.55$ s (curve with squares, luminosity 10% of the maximum), $t^* = -1.25$ s (curve with circles, maximum luminosity), and $t^* = 7.25$ s (curve with triangles, luminosity 10% of the maximum).

Thus, in our case, the source function will be

$$f(q,a) = y(q)a^\beta. \tag{72}$$

It is straightforward to derive the form of the light curve and resulting spectrum in this case if we make use of the linearity of the right-hand side of (13). Expression (72) can be rewritten as

$$f(q,a) = \int_0^\infty y(q_0)\delta(q-q_0)a^\beta dq_0. \tag{73}$$

Thus, it is clear that we can obtain the spectrum corresponding to a source function of the form (73) by replacing λ in formula (61) with $y(q_0)$ and integrating over q_0. In our case, we obtain after straightforward manipulation

$$\Phi(w,t^*) = 4\times 10^{71} w^{(\beta+7/2)} \tag{74}$$
$$\times \int_0^\infty \frac{{q_0}^{-(\beta+7/2)}}{1+\exp\left(\dfrac{q_0}{1.6E_0}-2\right)} d\left(\frac{q_0}{E_0}\right)$$
$$\times \int \rho \left(\frac{x}{m}\right)^{\beta+3/2}$$
$$\times \left[\Xi\left(1-m\frac{q_0}{w}\right) - \Xi\left(1-g^2 m\frac{q_0}{w}\right)\right] d\rho \text{ erg}^{-1}\text{ s}^{-1}.$$

The results of computations carried out using (68) and (74) are presented in Figs. 1 and 2. Figure 1 depicts the light curve of the collapsing star, which has a characteristic bell-shaped appearance. The duration of the neutrino pulse is approximately 10 s, i.e., $\sim 10 r_g/c$.

Figure 2 presents neutrino spectra at times $t = -1.25$ s (curve with circles), $t = -10.55$ s (curve with squares), and $t = 7.25$ s (curve with triangles), with the luminosity being maximum in the first case and 10% of the maximum in the latter two cases. We can see that the spectrum becomes softer with time due to the influence of the redshift.

6. CONCLUSIONS

The model presented here can be applied with source functions (12) with fairly arbitrary shapes. Our approximation that the shape of the spectrum of the radiating matter does not depend on temperature in our derivation of formula (70) was made only to simplify the calculation. If the source function cannot be presented in the form (72), it must be expanded in a Loran series,

$$f(q,a) = \sum_{n=-\infty}^{\infty} y_n(q)a^n,$$

and the linearity of the problem taken into account; i.e., it is necessary to obtain a solution for each term of the series separately and then sum the results.

Thus, our solution for the properties of a neutrino pulse arising during the collapse of a supermassive star can be used to consider various processes that generate neutrinos (plasma neutrinos, pair annihilation, and so forth). There is no question that the solution does not model a real collapse completely accurately; in particular, the assumption that the star is uniform during the collapse is crude. However, the resulting solution is very simple while also displaying

all the properties that are characteristic of real systems. This makes it possible to obtain light curves and spectra for such stars that are close to the real curves without having to carry out complex three-dimensional computations.

ACKNOWLEDGMENTS

One of the authors (A.N.B.) thanks S.L. Karepov and Yu. I. Khanukaev for useful discussions. This work was partially supported by the Russian Foundation for Basic Research (project codes 01-02-06146, 02-02-06596, 02-02-16900) and INTAS (INTAS-EKA grant 99-120 and INTAS grant 00-491).

REFERENCES

1. Ya. B. Zel'dovich, At. Energ. **521**, 49 (1963).
2. M. A. Podurets, Astron. Zh. **41**, 28 (1964) [Sov. Astron. **8**, 19 (1964)].
3. W. L. Ames and K. S. Thorn, Astrophys. J. **151**, 659 (1968).
4. S. L. Shapiro, Phys. Rev. D **40**, 1858 (1989).
5. S. L. Shapiro, Astrophys. J. **472**, 308 (1996).
6. X. Shi and G. M. Fuller, Astrophys. J. **503**, 307 (1998).
7. F. Linke, J. A. Font, H. T. Janka, *et al.*, Astron. Astrophys. **376**, 568 (2001).
8. L. D. Landau and E. M. Lifshits, *Field Theory* (Nauka, Moscow, 1980) [in Russian].
9. R. W. Lindquist, Ann. Phys. **37**, 487 (1966).
10. Ya. B. Zel'dovich and I. D. Novikov, *Relativistic Astrophysics* (Nauka, Moscow, 1967) [in Russian].
11. G. S. Bisnovatyĭ-Kogan, Astron. Zh. **45**, 74 (1968) [Sov. Astron. **12**, 74 (1968)].
12. P. J. Schinder, D. N. Schramm, P. J. Wiita, *et al.*, Astrophys. J. **313**, 531 (1987).
13. N. Itoh, T. Adachi, M. Nakagawa, *et al.*, Astrophys. J. **339**, 354 (1989).

Translated by D. Gabuzda

Astronomy Reports, Vol. 48, No. 3, 2004, pp. 246–253. Translated from Astronomicheskiĭ Zhurnal, Vol. 81, No. 3, 2004, pp. 272–280.

Topological Model for the Large Solar Flare of July 14, 2000

B. V. Somov[1], I. V. Oreshina[1], and G. P. Lubimov[2]

[1] *Sternberg Astronomical Institute, Universitetskiĭ pr. 13, Moscow, 119899 Russia*

[2] *Moscow State University, Skobeltsyn Institute of Nuclear Physics, Vorob'evy gory, Moscow, 119899 Russia*

Received July 5, 2003; in final form, August 8, 2003

Abstract—Using observational data obtained with the Yohkoh, SOHO, and TRACE satellites, it is shown that the three-dimensional structure of the large solar flare of July 14, 2000 was determined by the topology of the large-scale magnetic field of the active region giving rise to the flare. The locations and shapes of chromospheric ribbons and brightness centers on these ribbons are explained. The observed behavior of the flare is attributed to rapid magnetic reconnection in the corona. The electric field accelerating particles in the reconnecting current sheets is estimated. © *2004 MAIK "Nauka/Interperiodica"*.

1. INTRODUCTION

The flare of magnitude 3B/X5.7 observed on July 14, 2000 (nicknamed the "Bastille flare"), is among the most carefully studied solar flares of recent years. The active region NOAA 9077 that gave rise to the flare was observed over several days before and after the flare, and the flare itself was observed by all available ground and space facilities over its entire lifetime [1]. The most important observations for our work are Yohkoh observations [2] or, more precisely, soft and hard X-ray images of the flare [3]; TRACE ultraviolet observations of the flare-loop arcades and chromospheric ribbons [4, 5]; and SOHO observations of the photospheric magnetic field [4].

We propose a flare model based on the topological properties of the large-scale fields in active regions. The essence of the modeling [6] is that the real field of an active region in the solar atmosphere is replaced by a model field, whose sub-photospheric sources are chosen so that the calculated photospheric magnetogram gives the best fit to the observed photospheric field. The main features of the photospheric field should be reproduced: no fewer than four of its most important sources (sunspots and/or background fields), the shape of the photospheric neutral line, and the boundaries of regions with opposite magnetic polarities.

When this modeling is successful (for example, in the case of the prolonged flare of November 5, 1980 [7]), the topological model can reproduce the main features of the large-scale field in the corona, such as the separatrix surfaces (separatrices) and their lines of intersection (separators). This enables us to determine where and how the energy is stored before large flares and why this huge amount of energy is released during the short time of the flare. These questions are discussed in [6, 8].

In Section 2, we choose certain equivalent field sources located beneath the photosphere, which create the photospheric field that provides the best fit to the field observed before the flare. It is important that these sources uniquely determine the topological properties of the active-region magnetic field. In Section 3, we find the separatrices and separators for the magnetic field in the corona.

Note that the separatrices divide the field into fluxes, which interact at the separators during the evolution of the active region. During the flare, the accumulated interaction energy is converted into thermal and kinetic energy of plasma and accelerated particles [6]. Accordingly, in Section 4, we calculate the chromospheric locations of flare ribbons originating from the energy fluxes leaving the reconnection regions at the separators. Section 5 compares the active-region magnetic fields of July 12 and 14. This enables us to estimate the magnetic flux accumulated before the flare, as well as the electric field generated during the flare in regions of reconnection. Our conclusions are presented in the last section.

2. PHOTOSPHERIC FIELD MODEL

We model the photospheric field using several magnetic "charges" q_i located in a horizontal plane Q beneath the photosphere, in accordance with [9, 10]. In the recent studies [11, 12], the charges were situated directly in the plane of the photosphere Ph and the vertical field component B_z was zero everywhere except at the points where the charges were located. It is impossible to compare such a model with observed photospheric magnetograms, although this approach

1063-7729/04/4803-0246$26.00

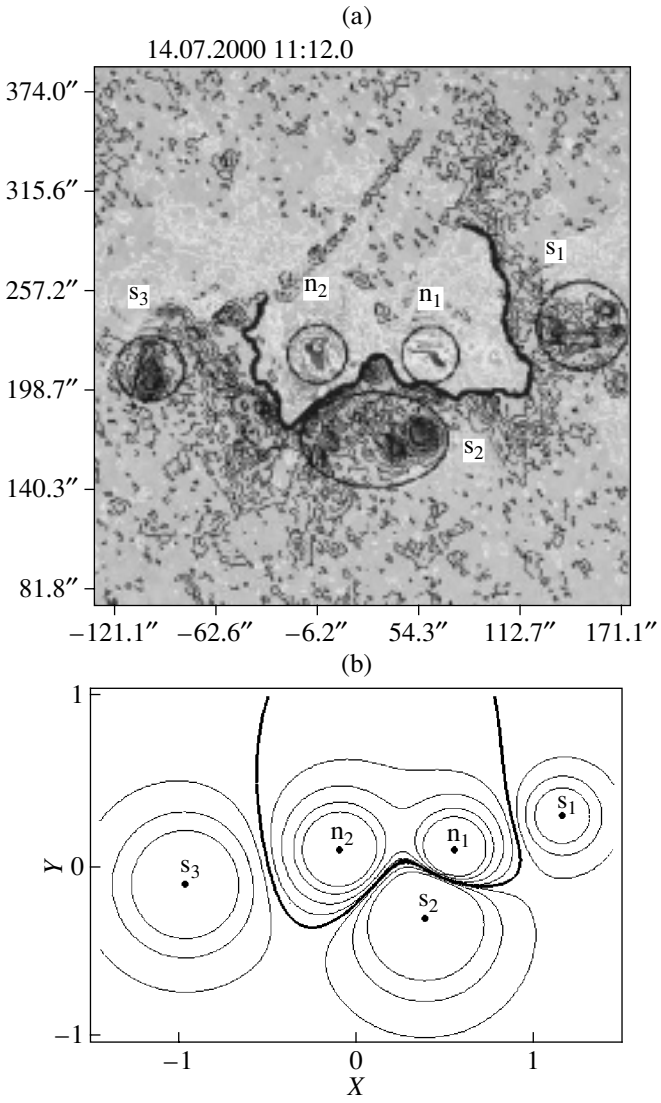

Fig. 1. (a) Observed and (b) modeled magnetograms for July 14, 2000 for the active region NOAA 9077.

is similar to our formulation of the problem. However, another aspect of our formulation is more important.

In [9–12], the magnetic field above the source plane Q is calculated in a potential approximation. Of course, the real active-region field differs from a potential field, especially at points where the flare energy accumulates. However, we assume that the nonpotential component is small and does not change the topological connectivity of the large-scale fields of active regions. This is based on the assumption that the magnetic field above the photosphere is strong [6], so that the energy of the field dominates over other forms of energy (see [13] for details).

We used for the initial data the SOHO MDI magnetogram obtained on July 14, presented in Fig. 1a (compare with Fig. 4 in [4]). One characteristic feature of this active region is the ω-shaped structure of the photospheric neutral line, shown by the thick curve in Fig. 1 (compare with Fig. 7 in [14]). We will attempt to reproduce this feature in the model magnetogram.

We somewhat arbitrarily identify the five largest regions in which magnetic field of a single polarity is concentrated in the real magnetogram (Fig. 1a): two of northern polarity (n_1 and n_2) and three of southern polarity (s_1, s_2, and s_3). Since the active region is comparatively close to the central meridian and the center of the solar disk, the magnetogram represents the vertical field component B_z at the photospheric level fairly well.

We then calculate B_z in the photospheric plane Ph in a potential approximation, i.e., using for the

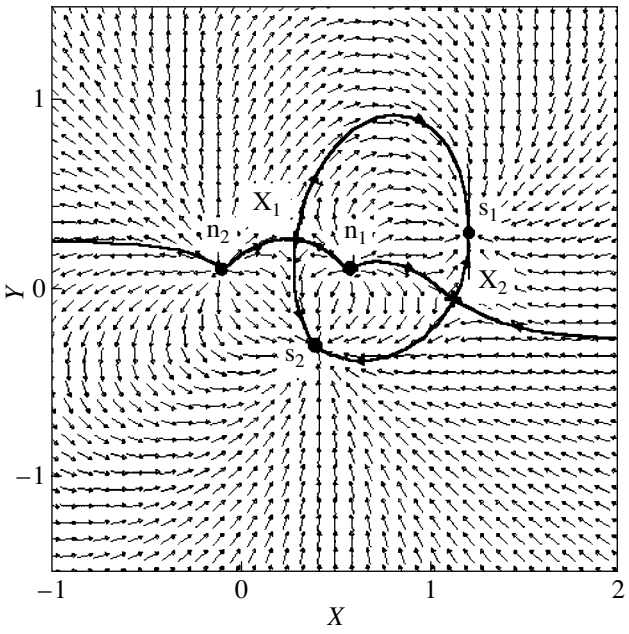

Fig. 2. Topological portrait of the western part of the active region giving rise to the first stage of the flare. The magnetic-field directions in the source plane Q, i.e., $z = -0.1$, are shown. The effective field sources n_1, n_2, s_1, and s_2 determine the topological features of the field: the zero points X_1 and X_2 and the bases of the separatrix surfaces in Q.

magnetic-field vector the simple formula

$$\mathbf{B}(x,y,z) = \sum_{i=1}^{5} \frac{q_i}{|\mathbf{r}-\mathbf{r}_i|^2}\frac{\mathbf{r}-\mathbf{r}_i}{|\mathbf{r}-\mathbf{r}_i|}. \qquad (1)$$

Here, q_i are the charges, and $\mathbf{r}_i$, their radius vectors:

$$q_1 = 2.0, \quad \mathbf{r}_1 = (-0.1, 0.1, -0.1); \qquad (2)$$

$$q_2 = 1.5, \quad \mathbf{r}_2 = (0.57, 0.1, -0.1);$$

$$q_3 = -0.5, \quad \mathbf{r}_3 = (1.2, 0.3, -0.1);$$

$$q_4 = -4.0, \quad \mathbf{r}_4 = (0.4, -0.3, -0.1);$$

$$q_5 = -2.6, \quad \mathbf{r}_5 = (-1.0, -0.1, -0.1).$$

The $z = 0$ plane corresponds to the photosphere, and the source plane Q is located at $z = -0.1$, beneath the photospheric level. Figure 1b shows contours of the z component of the field (1) and the neutral line $B_z = 0$ in the photospheric plane Ph, i.e., at $z = 0$. We can reproduce the largest-scale features of the real field, in particular, the ω-shaped photospheric neutral line, using only five sources, and this is quite sufficient for our analysis.

3. TOPOLOGICAL PORTRAIT OF THE ACTIVE REGION AND RELATED CORONAL FIELDS

Observations in various spectral lines, in particular a film presenting the TRACE data (see http://vestige.lmsal.com/TRACE/POD/TRACEpod.html), show that the flare moved along the neutral line from west to east, i.e., from right to left in Fig. 1a. The HXT Yohkoh hard X-ray images of the flare clearly indicate two stages in the impulsive phase of the flare: the bursts S1 and S2 [3]. We are especially interested in these stages, since the impulsive acceleration of a large number of electrons was observed at these times.

It appears that the two pairs of field sources n_1, n_2 and s_1, s_2 played the main role in the first flare stage S1, while the large-scale structure of the flare field in S2 was mainly determined by the sources n_1, n_2 and s_2, s_3. In other words, the region of the most powerful release of energy and accelerated electrons is initially located nearer to the field source s_1, then moves closer to s_3. This is clearly visible in the hard X-ray images of [3] (see also [4, 8]). Consequently, it is sufficient to use only the field sources n_1, n_2 and s_1, s_2 in our analysis of the topological structure of the large-scale field of the active region during the hard X-ray burst S1. Figure 2 shows these sources in the source plane Q at the level $z = -0.1$ beneath Ph. The arrows show the directions of the magnetic-field vectors in Q. The points X_1 and X_2 are zero-field points, where $B = 0$, and are important topological features of the field. The field separatrix lines, shown by solid curves with arrows, pass through the zero points and charges. The separatrix lines separate the magnetic fluxes connecting various sources of magnetic field. At the same time, these lines are the bases of the separatrix surfaces of the half-space above Q.

Figure 2 thus contains all the information needed to analyze the topology of the active-region magnetic field, and we therefore will refer to it as the topological portrait of the active region.

Figure 3 shows the three-dimensional field structure above the plane of the topological portrait. The separatrix surfaces have the forms of domes of various sizes, with their bases being situated on separatrix field lines in the source plane Q. The separatrix surfaces intersect along the magnetic-field line connecting the zero points X_1 and X_2. This critical line belongs simultaneously to four magnetic fluxes with differing connectivity; it is called a separator. There was a redistribution of magnetic fluxes (magnetic reconnection) at the separator during the burst S1.

The field lines were calculated via numerical integration of the ordinary differential equations

$$\frac{dx}{B_x} = \frac{dy}{B_y} = \frac{dz}{B_z}, \qquad (3)$$

where (dx, dy, dz) is an arc element along the field line. The vector **B** is determined at each point by (1).

4. CHROMOSPHERIC RIBBONS

Reconnection at separators transforms accumulated magnetic energy into the thermal and kinetic energy of plasma and accelerated particles. Propagating along the magnetic-field lines and reaching dense layers in the chromosphere, the flare energy fluxes give rise to a complex hydrodynamic and radiative response [15]. Secondary processes in the chromospheric plasma result in the basic flare behavior observed in the optical, UV, and hard X-ray.

Large flares frequently display two-ribbon structures in their chromospheric emission, long suspected of being associated with magnetic reconnection processes in the corona (see [4] and references therein). The correctness of this hypothesis was confirmed by the topological model for the flare of November 5, 1980 [7, 10].

Returning to the Bastille flare, the impulsive phase of the flare consisted of the two bursts of hard X rays S1 [8] and S2 [3]. Following [7, 10], we will assume that the most powerful release of energy and accelerated electrons during S1 [8] took place at the vertex of the separator situated in the western part of the active region, as was determined in the previous section and shown in Fig. 3.

Consider as an illustration a circle O encompassing the separator near its vertex in a plane perpendicular to the separator. We choose a system of uniformly distributed points on this circle and calculate the magnetic-field lines passing through each point until their intersection with the photospheric plane Ph. Figure 4 shows the circle O at the separator vertex, the magnetic-field lines passing through the circle, and narrow ribbons formed by the intersections of field lines with Ph.

We can easily understand the formation of long, narrow ribbons. The magnetic field near the separator has a characteristic saddle configuration. The field lines approach the separator on the first separatrix surface and diverge from it on the second separatrix surface (see Fig. 2 in [16]). Consequently, a closed contour passing along the field lines and encompassing the separator, initially in the form of a circle O, is deformed first into an ellipse and then (approaching the chromosphere) into a narrow, long ribbon. Figure 4 shows two ribbons formed by the field lines: the first in the direction of the magnetic field and the second in the opposite direction. For this reason, the ribbons are located on either side of the photospheric neutral line.

The chromospheric ribbons of the Bastille flare observed in the UV using the TRACE satellite (for example, at 171 Å) [4, 5] and in hard X rays using Yohkoh [3, 8] were created by energy fluxes from the entire separator. In addition, real sources of magnetic field are not as concentrated and simple as model sources. Nevertheless, the simple example with the circle O is quite informative and seems to capture the essence of the phenomenon of chromospheric ribbons.

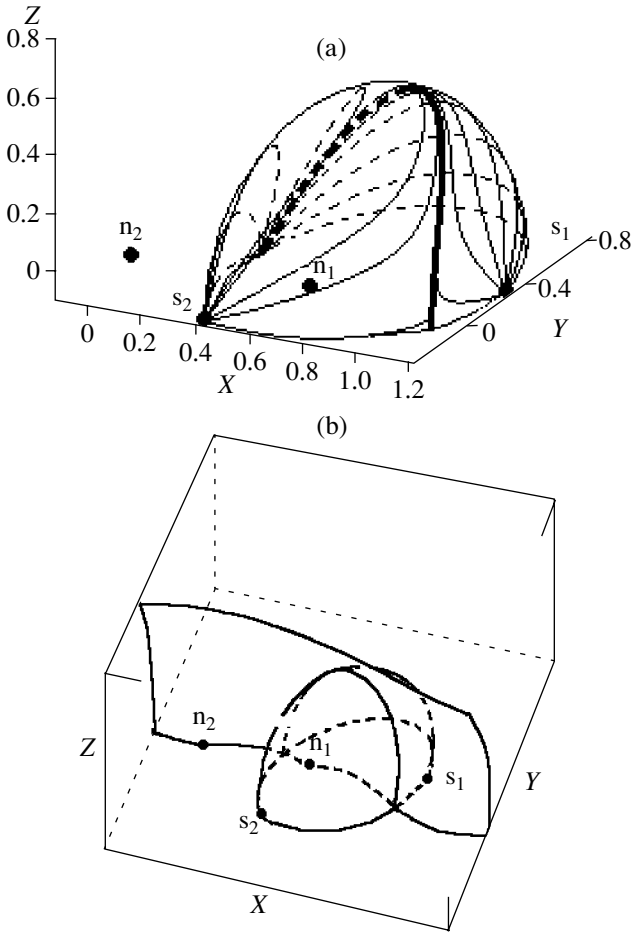

Fig. 3. (a) Magnetic-field lines forming the separatrix surface that is a dome bounding the flux from the source n_1. (b) Separatrix surfaces dividing the fluxes between magnetic-field sources of northern and southern polarities and the (separator) line of their intersection.

The topological model can also explain another interesting feature of chromospheric ribbons. Most of the field lines escaping from the circle O are gradually concentrated at the ends of the ribbon as they leave the separator. This should result in a bifurcation of the fluxes of heat and of accelerated particles flowing along the magnetic-field lines, with these fluxes being carried to the ribbon ends, where the brightest centers observed in various wavelengths are formed [7, 10, 17]. These centers are probably somewhat broadened

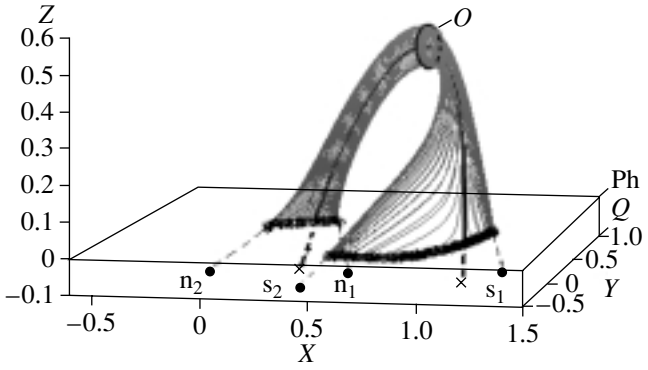

Fig. 4. The circle O as an element of the region of primary energy release at the separator and part of the flare ribbons resulting from this release at the photospheric level.

since the energy is released over the entire separator rather than only at its vertex.

Figure 5a presents similar calculations for chromospheric ribbons during the hard X-ray burst S2 [4]. The ribbons are shown by the dashed curves, with two ribbons being located between the field sources n_1 and n_2: the upper ribbon corresponds to the first stage of the impulsive phase, and the lower, to the second stage. The ribbon between the sources s_1 and s_2 corresponds to the first burst, and the ribbon between s_2 and s_3, to the second.

Figure 5b presents a TRACE image of the flare at 171 Å obtained during S2. The eastern part of the flare is somewhat brighter than the western part. A chromospheric ribbon is clearly visible between the points corresponding to the field sources s_2 and s_3 in Fig. 5a. Bright centers at the ends of the ribbon are visible. The observed ribbons are arc-shaped and are in good overall agreement with the locations and shapes of the calculated ribbons. More precisely, the calculated ribbons can reproduce large portions of the observed ribbons.

We can achieve a better agreement between the observed chromospheric ribbons and the model ribbons using additional effective magnetic charges q_i or replacing the charges with more precise distributions of the field sources [18, 19], thereby naturally increasing the number of separators [12, 20]. However, this does not seem justified. The real magnetic field and real velocities in the photosphere contain at least two components: regular, large-scale and chaotic, small-scale. The topological model takes into account only the first component, with the aim of describing the global mechanism behind large flares. Fine temporal and small-scale spatial structures of large flares must be described using other models that correspond better to these goals.

5. MAGNETIC FLUXES AND ELECTRIC FIELDS

The magnetic fields of the active region NOAA 9077 were observed during several days before and after the Bastille flare [14, 21, 22]. There were more than a hundred flares in the active region over this period, three of them accompanied by X-ray emission. The largest flare (X5.7) was on July 14 (the Bastille flare), and the next largest in magnitude (X1.9) was on July 12. It is suggested in [8] that the magnetic energy of the active region reached its minimum after this flare and that the energy released in the Bastille flare was accumulated over the following two days (July 12–14).

Figures 1a and 6a present magnetograms of the active region obtained on July 14 and 12. A comparison shows that the photospheric neutral line (shown by the thick curve in Fig. 6a) is somewhat smoother on July 12 than on July 14. Figure 6b presents the corresponding model magnetogram, for which the coordinates of the effective charges are the following:

$$\begin{aligned} \mathbf{r}_1 &= (-0.08, 0.27, -0.1), \\ \mathbf{r}_2 &= (0.3, 0.27, -0.1), \\ \mathbf{r}_3 &= (1.2, 0.3, -0.1), \\ \mathbf{r}_4 &= (0.1, -0.3, -0.1), \\ \mathbf{r}_5 &= (-1.0, 0.3, -0.1); \end{aligned} \tag{4}$$

with the charge strengths being the same as for July 14.

Let us calculate the magnetic flux beneath the separator. By definition,

$$\Psi = \int_{\Sigma} \mathbf{B} d\mathbf{s}, \tag{5}$$

where Σ is the surface through which the flux flows. The boundary of this surface is a closed contour $\mathcal{L}$. The contour $\mathcal{L}$ for the western part of the active region

consists of the separator connecting the zero points X_1 and X_2 in the half-space above the source plane Q of the topological portrait and the line (X_1X_2) connecting the same points in Q. The calculated fluxes for July 12 and 14 are $\Psi_{12} \approx 4.5 \times 10^{21}$ Mxw and $\Psi_{14} \approx -1.4 \times 10^{21}$ Mxw, respectively.

The difference of these quantities is $\delta\Psi = \Psi_{14} - \Psi_{12} \approx -6 \times 10^{21}$ Mxw. What is the physical meaning of $\delta\Psi$? If there were a vacuum without plasma above the source plane Q, the flux $\delta\Psi$ would reconnect at the separator (X_1X_2) over the evolution of the photospheric field sources and the magnetic field would remain potential. In the high-conductivity plasma, variations in the photospheric sources induce electric currents at the separator. These currents form a current sheet that prevents the reconnection of the flux $\delta\Psi$, and energy is accumulated in the magnetic field of the current sheet [6].

The energy stored for the first stage of the Bastille flare is estimated to be $\mathcal{E}_f \sim 3 \times 10^{31}$ erg, which corresponds to a total separator current of $J \sim 3 \times 10^{11}$ A. This is consistent with the level of nonpotentiality of the active region estimated from measurements of the three components of the photospheric magnetic field [23]. Before the flare of July 14, the level of nonpotentiality, including the total current along the line of sight and the stored magnetic energy, was appreciably higher (see Fig. 5 in [23]). Note that these estimates correspond to the first stage of the impulsive phase of the flare, i.e., to the hard X-ray burst S1, which was somewhat weaker than S2, which was the main burst during the impulsive phase of the flare.

The most rapid reconnection of the magnetic field $\delta\Psi$ occurs during the impulsive phase. Using the duration of this stage δt, we can estimate the electric field in the reconnecting current sheet at the separator as follows:

$$\mathbf{E} = -\frac{1}{c}\frac{\partial \mathbf{A}}{\partial t}. \qquad (6)$$

Here, $\mathbf{A}$ is the vector potential, i.e., $\mathbf{B} = \mathrm{curl}\mathbf{A}$, and c is the speed of light. The flux Ψ can be written as a function of $\mathbf{A}$ as follows:

$$\Psi = \oint_{\mathcal{L}} \mathbf{A}\mathrm{d}\mathbf{l} \sim A \cdot L, \qquad (7)$$

where L is the length of the closed contour $\mathcal{L}$ described above. In finite differences, we have the following formula enabling us to estimate the electric field:

$$E \sim -\frac{1}{c}\frac{1}{\delta t}\left(\frac{\Psi_{14}}{L_{14}} - \frac{\Psi_{12}}{L_{12}}\right). \qquad (8)$$

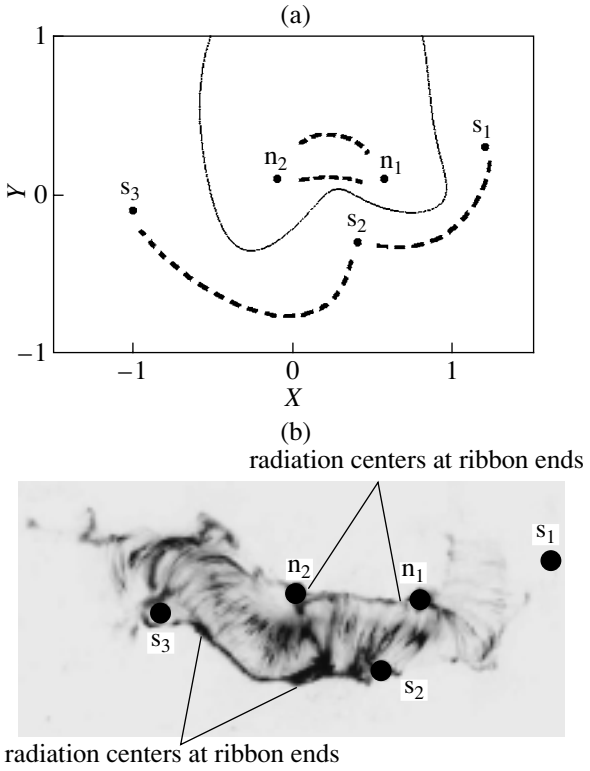

Fig. 5. (a) Five field sources projected onto the photospheric plane Ph, the photospheric neutral line (solid curve), and flare ribbons (dashed curves). (b) TRACE image of the flare at 171 Å.

Taking the duration of the impulsive stage of electron acceleration during the burst S1 of hard X rays with energies exceeding 33 keV to be $\delta t \approx 3$ min [3, 8], we obtain $E \sim 30$ V/cm, in agreement with electric-field estimates obtained for impulsive solar flares using the theory of reconnecting current sheets [6].

We can also estimate the reconnected flux in another way. Since the energy fluxes from the separator reconnection region result in the formation of chromospheric ribbons, these ribbons correspond to newly reconnected field lines (see, for example, [24]). In the so-called standard model (a two-dimensional MHD model for two-ribbon flares with vertical current sheets, see, for example, [25]), ascending regions of reconnection give rise to chromospheric ribbons moving in opposite directions from the photospheric neutral line. In the general case, a ribbon's motion with respect to the photospheric magnetic field can be used to estimate the magnetic flux reconnected during the corresponding flare.

In the case of the Bastille flare, Fletcher and Hudson [4] estimated the reconnected flux to be $\delta\Psi \approx 11.2 \pm 0.5$ Mxw by analyzing the motions of the northern and southern UV ribbons observed by the TRACE satellite at the maximum of the hard X-ray

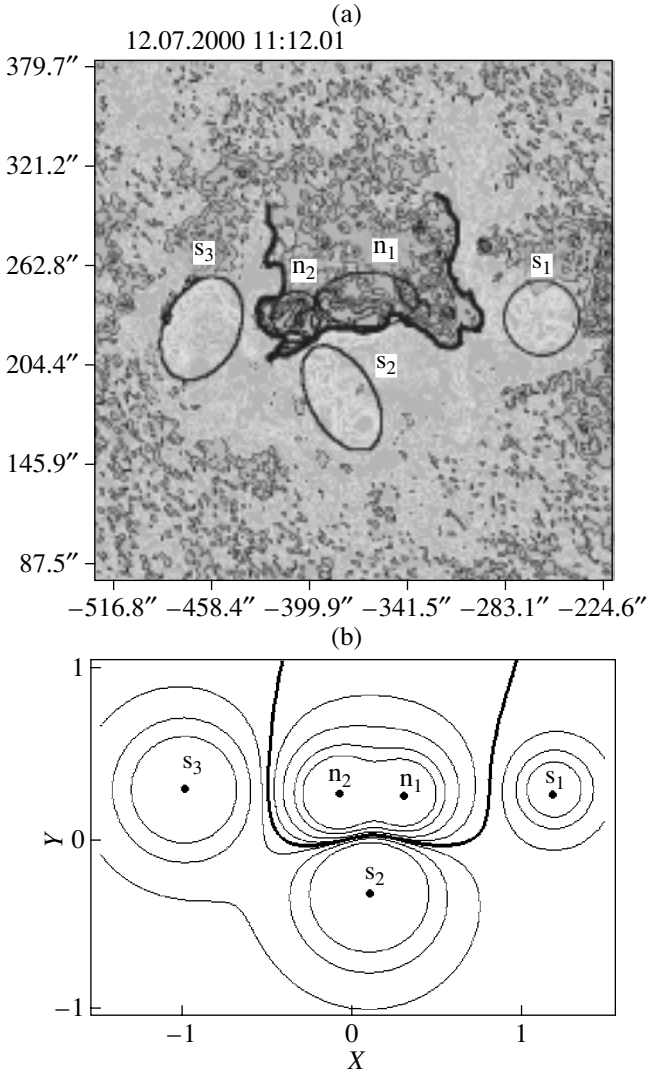

Fig. 6. (a) Observed and (b) modeled magnetograms for the active region NOAA 9077 on July 12, 2000.

burst S2. This is in good agreement with our estimate for the first stage of the flare.

Systematic motions of bright centers on chromospheric ribbons observed in the Hα line during solar flares have also been considered to be chromospheric effects of the reconnection of magnetic lines in the corona. The two types of motions relative to the magnetic field (along and across the magnetic-field lines) are a consequence of different effects and have different properties [24].

Analysis of these effects in the blue extension of the Hα line [26] shows that the electric fields in some impulsive flares can be appreciably stronger than our estimate calculated using the topological model. For example, the electric field reached 90 V/cm during the C9.0-magnitude flare observed on March 16, 2000. Such strong fields are consistent with the theory of reconnecting current sheets applied to impulsive flares [6, Fig. 17.4].

The observations of [26] also show that temporal changes in the electric fields are correlated with the intensity of hard X rays at 20–85 keV during the growth stage of the impulsive phase of a flare. This supports models in which the acceleration of electrons with energies below $\sim$100 keV occurs in reconnecting current sheets at separators in the corona [27].

6. DISCUSSION AND CONCLUSIONS

It is obvious that our topological model is only relevant for large flares, since it neglects fine temporal behavior and small-scale processes and concentrates on the general evolution of the global structure of the

flares. Note that such large flares can strongly influence interplanetary space and the near-Earth environment due to the generation of shock waves, accelerated particles, and hard electromagnetic radiation.

The topological model for large-scale magnetic fields remains simple and clear, even for the complex active region as NOAA 9077 that gave rise to the Bastille flare (a $\beta\gamma\delta$ configuration, according to [14]). At the same time, the topological model can easily explain the main observed features of this well-studied flare. First, the model predicts the location of the flare energy source in the corona and can reproduce the locations and shapes of chromospheric ribbons and bright centers on the ribbons. Second, the model can explain the observed flare dynamics as an effect of rapid magnetic reconnection in current sheets at separators and can be used to estimate the rate of magnetic reconnection and the strength of the electric fields accelerating charged particles during the flare.

ACKNOWLEDGMENTS

This work was supported by the Russian Foundation for Basic Research (project code 99-02-16344).

REFERENCES

1. Solar Phys. **204** (2001).
2. P. C. H. Martens and D. P. Cauffman, in *Yohkoh 10th Anniversary Meeting: Multi-Wavelength Observations of Coronal Structure and Dynamics* (Pergamon, Amsterdam, 2002).
3. S. Masuda, T. Kosugi, and H. S. Hudson, Solar Phys. **204**, 57 (2001).
4. L. Fletcher and H. Hudson, Solar Phys. **204**, 71 (2001).
5. M. J. Ashwanden and D. Alexander, Solar Phys. **204**, 93 (2001).
6. B. V. Somov, *Cosmic Plasma Physics* (Kluwer, Boston, 2000).
7. V. S. Gorbachev and B. V. Somov, Adv. Space Res. **10** (9), 93 (1990).
8. B. V. Somov, T. Kosugi, H. S. Hudson, *et al.,* Astrophys. J. **579**, 863 (2002).
9. V. S. Gorbachev and B. V. Somov, Solar Phys. **117**, 77 (1988).
10. V. S. Gorbachev and B. V. Somov, Astron. Zh. **66**, 105 (1989) [Sov. Astron. **33**, 57 (1989)].
11. D. W. Langcope and A. A. van Ballegooijen, Astrophys. J. **578**, 573 (2002).
12. D. W. Langcope and I. Klapper, Astrophys. J. **579**, 468 (2002).
13. B. V. Somov, T. Kosugi, H. S. Hudson, *et al.,* Adv. Space Res. (2003, in press).
14. Y. Liu and H. Zhang, Astron. Astrophys. **372**, 1019 (2001).
15. B. V. Somov, *Physical Processes in Solar Flares* (Kluwer Acad., Boston, 1992).
16. V. S. Gorbachev, S. R. Kel'ner, B. V. Somov, and A. S. Shvarts, Astron. Zh. **65**, 601 (1988) [Sov. Astron. **32**, 308 (1988)].
17. M.-J. Martes, R. Michard, and I. Soru-Escaut, Ann. Astrophys. **29**, 249 (1966).
18. C. H. Mandrini, P. Demoulin, J. C. Hénoux, and M. E. Machado, Astron. Astrophys. **250**, 541 (1991).
19. C. H. Mandrini, M. G. Rovira, P. Demoulin, *et al.,* Astron. Astrophys. **272**, 609 (1993).
20. D. W. Longcope and A. V. R. Silva, Solar Phys. **179**, 349 (1998).
21. Y. Liu and H. Zhang, Astron. Astrophys. **386**, 646 (2002).
22. H. Zhang, Mon. Not. R. Astron. Soc. **332**, 500 (2002).
23. Y. Deng, J. Wang, Y. Yang, and J. Zhang, Solar Phys. **204**, 13 (2001).
24. B. V. Somov, T. Kosugi, and T. Sakao, Astrophys. J. **497**, 943 (1998).
25. T. G. Forbes and L. W. Acton, Astrophys. J. **459**, 330 (1996).
26. J. Qiu, J. Lee, D. E. Cary, and H. Wang, Astrophys. J. **565**, 1335 (2002).
27. Y. E. Litvinenko and B. V. Somov, Solar Phys. **146**, 127 (1993).

Translated by V. Badin

Astronomy Reports, Vol. 48, No. 3, 2004, pp. 254–260. Translated from Astronomicheskiĭ Zhurnal, Vol. 81, No. 3, 2004, pp. 281–288.

Active Longitudes and North–South Asymmetry of the Activity the Sun as Manifestations of Its Relic Magnetic Field

A. V. Mordvinov and L. L. Kitchatinov

Institute for Solar–Terrestrial Physics, Siberian Division, Russian Academy of Sciences, P.O. Box 4026, Irkutsk, 664033 Russia

Received May 14, 2003; in final form, September 18, 2003

Abstract—The distributions of dominant magnetic polarities in synoptic maps of photospheric magnetic fields and their extrapolations to the corona based on Stanford Observatory data are studied. Both dipolar and quadrupolar magnetic patterns are detected in the distributions of dominant polarities in the near-equatorial region of the photosphere for activity cycles 21, 22, and 23. The field in these patterns often has opposite signs on opposite sides of the equator, with this sign changing from cycle to cycle. A longitude–time analysis of variations of the mean solar magnetic field shows that the contribution of the large-scale magnetic patterns to the total field does not exceed 20 μT. The most stable magnetic structures at a quasi-source surface in the solar corona are separated by approximately 180° in heliographic longitude and are close to dipolar. The nature and behavior of these large-scale magnetic patterns are interpreted as a superposition of cyclic dynamo modes and the nonaxially symmetric relic field of the Sun. The contribution of the relic field to the mean solar magnetic field appears as a weak but stable rotational modulation whose amplitude does not exceed 8 μT. © *2004 MAIK "Nauka/Interperiodica".*

1. INTRODUCTION

The solar magnetic fields have a multiscale hierarchical structure and are manifest as groups of spots, activity complexes, and background magnetic fields. Global magnetic patterns are observed in the solar atmosphere in the form of giant arcades and the sector structure [1, 2]. The global pattern of solar magnetic activity is also manifest in the concentration of the most powerful active phenomena within relatively narrow intervals of heliographic longitude, called active longitudes [3]. Active longitudes can persist over several 11-year cycles [4]. Antipodal active longitudes separated by approximately 180° are often observed [4, 5]. Detailed studies of the spatial and temporal behavior of solar activity have shown that the powers of active longitudes in the northern and southern hemispheres can be substantially different and that the maximum activity can be transferred from one longitude interval to another [5].

As a result of the nonuniform distribution of long-lived magnetic structures, the flux of solar radiation is not isotropic and, after averaging over a large number of revolutions, has two maxima separated by approximately 180° in longitude [6]. This demonstrates that there is a specific direction in the Sun for which the integrated radiation flux is enhanced over the mean value.

Long-lived magnetic longitudes are also observed in other solar-type stars [7]. Analysis of the brightness variations of such magnetic stars shows that the active longitudes are likewise often separated by approximately 180°. Spontaneous transfers of the maximum power from one active longitude to another are sometimes observed. This effect, discovered in stars relatively recently, has been called the "flip–flop effect" [7]. Thus, there are common features in the large-scale organization of magnetic activity of the Sun and solar-type stars, whose nature remains unknown.

A number of facts about the spatial and temporal behavior of solar cycles can be explained by the existence of a solar relic magnetic field that is frozen into the radiative core and penetrates the convection zone. Cowling [8] was the first to note the possible existence of a relic solar field. According to his estimates, the characteristic time for Ohmic dissipation of the large-scale field in the radiative zone is comparable to the age of the Sun, so that the largest-scale component of this field should survive to the present time. This concept was further developed in [8–12].

As was argued in [13], the relic magnetic field probably resulted from a primordial dynamo mechanism and was captured from the surrounding convective envelope by the radiative core in the early stages of its formation. The relic field is not axially symmetric and includes a considerable poloidal component; its intensity is a few tenths of a Gauss. This relic field is superimposed onto the magnetic field generated by the solar dynamo in the course of the 11-year activity cycle. Due to the changing polarity of the magnetic

1063-7729/04/4803-0254$26.00

field from cycle to cycle, the resulting poloidal field can be amplified or attenuated, in accordance with the Hale law. A toroidal field with corresponding magnitude is generated, and the successive 11-year cycles have alternating higher and lower amplitudes [14]. In the interests of brevity (or simplicity), we will refer to the quasi-dipolar component of the large-scale magnetic field as the relic field.

According to the well-known empirical rules of Gnevyshev and Ol' [15], the amplitudes of odd cycles exceed the amplitudes of the preceding even cycles. These regular amplitude changes are modulated by the long-term cycle. The Gnevyshev–Ol' rule is not always satisfied exactly; for example, the amplitude of the current (23rd) cycle is less than the amplitude of the previous (22nd) cycle, and similar irregularities have been noted earlier [16].

Thus, there is indirect evidence for the existence of a relic magnetic field but no direct proof due to the difficulty of detecting the weak relic field against the background of strong photospheric magnetic fields. In the present work, we analyze synoptic maps of the solar magnetic field and variations in the mean magnetic field of the Sun as a star in order to obtain direct evidence for the existence of the relic magnetic field. We also propose a qualitative explanation of the behavior of the longitudinal structure of solar activity in the 11-year cycle as an effect of the interaction between the relic magnetic field and the solar dynamo. In general terms, this effect can also explain the nature and behavior of magnetic activity in solar-type stars.

2. DOMINANT POLARITIES IN THE DISTRIBUTION OF THE PHOTOSPHERIC AND CORONAL MAGNETIC FIELDS

To study long-lived, large-scale magnetic-field structures, we analyzed synoptic maps of the photospheric magnetic fields obtained at the Wilcox Solar Observatory in 1976–2002 [17, 18]. Each map is represented by a matrix of values of the longitudinal magnetic field over one complete Carrington revolution, $B_{i,j}$, where $i = 1, 2, \ldots, 30$ corresponds to a uniform scan in the sine of the latitude from $-14.5/15$ to $+14.5/15$ and $j = 1, 2, \ldots, 73$ corresponds to a scan in heliographic longitude in steps of 5°.

We summed the synoptic maps for activity cycles 21, 22, and 23 separately. Since the structure of the global magnetic field changes after reversals of the polar magnetic field at epochs 1981.8, 1991.8, and 2001.7 [19], it is reasonable to sum the synoptic maps separately for phases of increasing and decreasing activity. To reveal the weak large-scale magnetic field against the background of stronger local magnetic fields, we must use a robust summation procedure that is stable against large point-to-point fluctuations of the magnetic field and is not substantially affected by errors in the magnetographic measurements. We summed the synoptic maps as matrices taking into account only the sign of the magnetic field in each grid cell. The resulting distributions normalized to the number of Carrington revolutions in the cycle are shown in Fig. 1. These total maps characterize the probability distribution for the occurrence of positive and negative polarities in activity cycles 21 (Figs. 1a, 1b), 22 (Figs. 1c, 1d), and 23 (Figs. 1e, 1f) before and after field reversals. The data for cycle 23 are incomplete and are restricted to Carrington revolution 1999.

The quantity presented in Fig. 1 is not precisely a frequency or probability, because it also characterizes the sign of the field and it varies from -1 to $+1$. A gray scale that numerically characterizes the sum is given at the bottom. For example, if the sum is 0.0 at some point, positive and negative polarities appear there equally often, so that the corresponding probabilities are 0.5. Structures dominated by positive polarity are shown by light areas, and those dominated by negative polarity, by dark areas. The black and white curves correspond to one standard deviation of the sum from the mean (zero) value, corresponding to a significance level of about 68%, for the positive and negative polarities, respectively.

More or less regular structures are visible in the distributions. These change from cycle to cycle, as well as during the global reconstruction of the magnetic field associated with field reversals. For example, in cycle 21 averaged from its onset to the field reversal (Fig. 1a), positive polarity dominates in the equatorial region of the northern hemisphere at longitudes of 0°–72° and 174°–360°, while negative polarity dominates in the equatorial region of the southern hemisphere at longitudes of 0°–234° and 344°–360°. This averaged distribution characterizes the rising magnetic fields. After the field reversal, the high-latitude magnetic fields change their direction and their boundaries shift to ±40°. The positions of local extrema in the distribution of dominant polarities change slightly but remain qualitatively the same as in the first part of the cycle.

In cycle 22, negative polarity dominates in the northern hemisphere at longitudes of 0°–200° and 320°–360°, while positive polarity dominates in the southern hemisphere at longitudes of 0°–200° and 345°–360°. The distribution of dominant polarities in the equatorial region usually displays opposite signs on opposite sides of the equator and changes from cycle to cycle, as is especially visible in the phase of increasing activity. The distributions of dominant

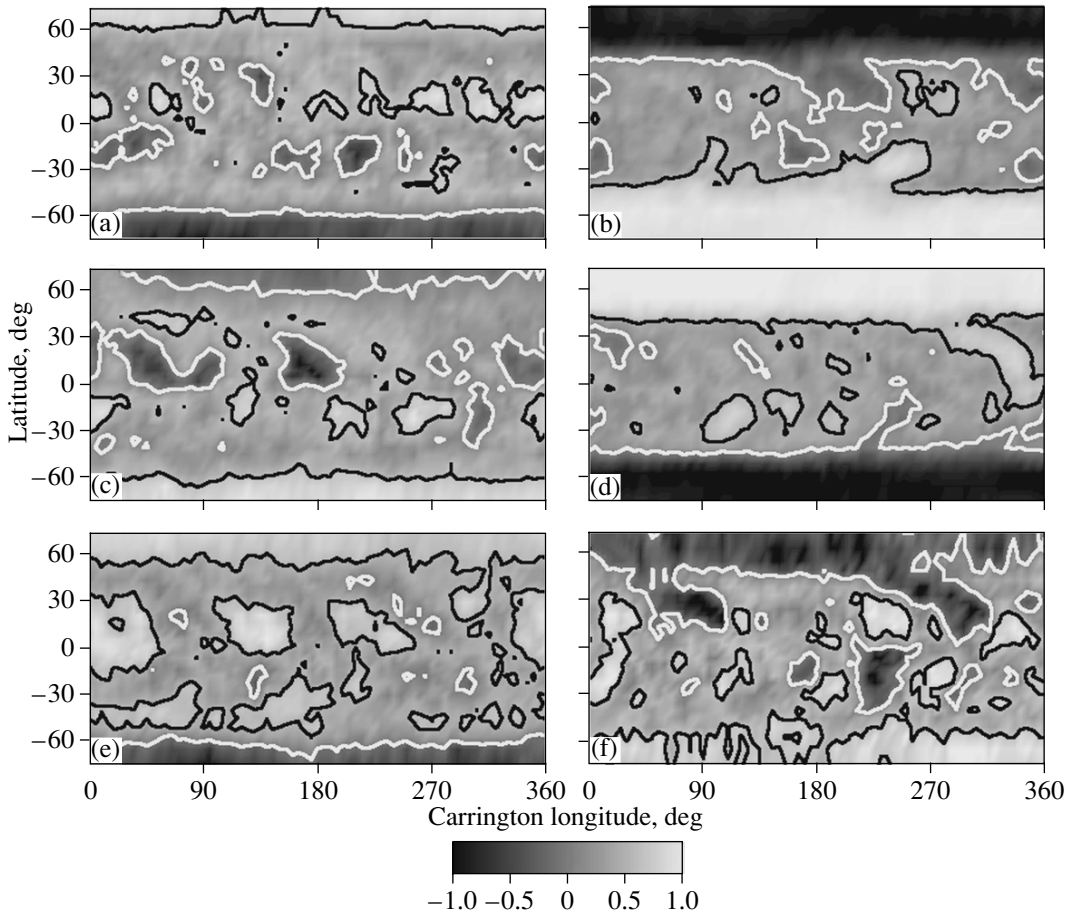

Fig. 1. Distribution of dominant polarities of the photospheric magnetic fields for activity cycles 21 (a, b), 22 (c, d), and 23 (e, f) estimated using synoptic maps for time intervals before (a, c, e) and after (b, d, f) reversals of the polar field.

polarities averaged over time intervals after field reversals (Figs. 1b, 1d) display characteristic inclined structures associated with the drift of the "tail" polarities toward high latitudes.

In cycle 23 (Fig. 1e), positive polarities dominate in the equatorial regions of the northern and southern hemispheres, while there are almost no significant stable structures with negative polarity. This appears anomalous in comparison with the previous cycles. Stable regions of negative polarity are already observed after the field reversal in the current cycle (Fig. 1f), although this pattern cannot be accurately traced since cycle 23 has not yet finished.

Thus, summing the synoptic maps of the photospheric magnetic fields has enabled us to detect stable large-scale magnetic-field structures and their variations from cycle to cycle. These variations are fairly complex and are strongly affected by the magnetic fields of individual active regions and activity complexes. To study larger spatial and temporal scales and the behavior of the global solar magnetic field, we carried out a similar analysis of synoptic maps of the coronal magnetic field calculated in a potential approximation at a distance of 2.5 solar radii [18, 20]. The magnetic field at this quasi-source surface reflects the large-scale structure of the field, with a negligible contribution from individual active regions.

The distributions of dominant polarity derived by averaging the synoptic maps of the magnetic field at the quasi-source surface in the corona are shown for cycles 21, 22, and 23 separately in Figs. 2a, 2b, and 2c. An approximately dipolar longitudinal structure is clearly visible in all the distributions. For example, in cycle 21 (Fig. 2a), the coordinates of the positive pole are $L = 263°$, $\varphi = -7°$ and the coordinates of the negative pole are $L = 100°$, $\varphi = +60°$, where L and φ are the heliographic longitude and latitude. The positions of the dipole poles are marked by "+" and "−" signs. In cycle 22 (Fig. 2b), the positive and negative poles are located at $L = 232°$, $\varphi = +34°$ and $L = 45°$, $\varphi = -10°$, respectively. Comparing the distributions of dominant polarities in cycles 21 and 22, we can see that the polarities were reversed from one cycle to another in accordance with the Hale law,

but the corresponding positions of the poles did not change substantially, remaining the same within the uncertainties. The distribution of dominant polarities derived for the incomplete current cycle 23 (Fig. 2c) differs substantially from the two previous distributions. The magnetic dipole rotated by approximately 180°. This behavior of the global magnetic field and the corresponding longitudinal organization of the magnetic activity can be interpreted as a reversal of the active longitudes, known as the flip–flop effect in solar-type stars [7].

This approach enables us to map the structure of the dominant polarities in longitude and latitude but not to estimate the magnetic-field strength. To evaluate the magnetic-field strength in the detected large-scale structures, we analyzed the longitude and time variations in a series of measurements of the mean magnetic field of the Sun (MMFS).

3. LONGITUDE–TIME ANALYSIS OF THE MMFS

The background magnetic fields observed in the synoptic maps produce the main contribution to the MMFS, measured as a convolution of the longitudinal component of the magnetic field and the weighting function of the magnetograph [17, 21, 22]. Dynamo modes with azimuthal wave numbers 1 and 2 [23, 24] and the relic solar magnetic field also contribute to the observed MMFS variations.

We used a latitude–time analysis of the MMFS series based on a wavelet deconvolution to detect large-scale magnetic structures [25, 26]. The main idea behind this approach is to separate from the initial signal a component containing information about inhomogeneity in the longitude distribution of the magnetic fields, which is manifest over the rotational time scale, and to present this component as a longitude–time diagram scanning with the Carrington time.

The numerical realization of this method and filtration were carried out using an orthogonal wavelet decomposition, which is well suited to analyzing nonstationary processes. We chose Daubechies wavelets, which display good frequency–time localization, as the analyzing functions. The time scales of the wavelet functions used for the decomposition were discrete and equal to powers of two. Only wavelet coefficients corresponding to time scales of 8, 16, and 32 days were saved from the resulting decomposition, while other coefficients were discarded. Further, the inverse wavelet transformation was performed. This enabled us to estimate the component of the signal containing the main effects of the rotational modulation of the MMFS due to spatial inhomogeneity of the large-scale magnetic field.

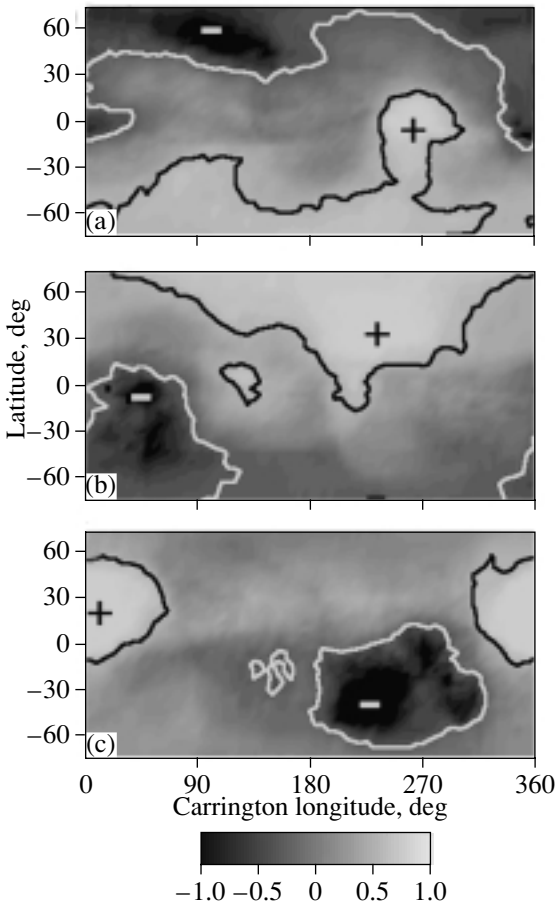

Fig. 2. Distributions of dominant polarities of the magnetic field at the quasi-source surface for activity cycles (a) 21, (b) 22, and (c) 23.

The MMFS series from Wilcox Solar Observatory [18] and the corresponding longitude–time diagram are shown in Fig. 3. This diagram contains information about the distribution of the large-scale magnetic field as a function of Carrington longitude. The wavelet deconvolution enables us to construct a complete pattern of the solar rotation from the time variations of the MMFS and to detect rigidly rotating coherent structures in the dynamics of the large-scale magnetic field [25, 26].

We analyzed the longitude–time distribution of the MMFS specifically from the viewpoint of long-lived magnetic structures. The distribution was averaged over time intervals corresponding to activity cycles 21, 22, and 23. The cycle-averaged distributions of the large-scale magnetic field as functions of longitude are shown in Fig. 4. The dotted curve represents the structure of the magnetic field in cycle 21, which was characterized by a quadrupolar polarity distribution, or a four-sector structure. The positive polarities are centered at longitudes of 86° and 263°, while negative polarities are centered at longitudes

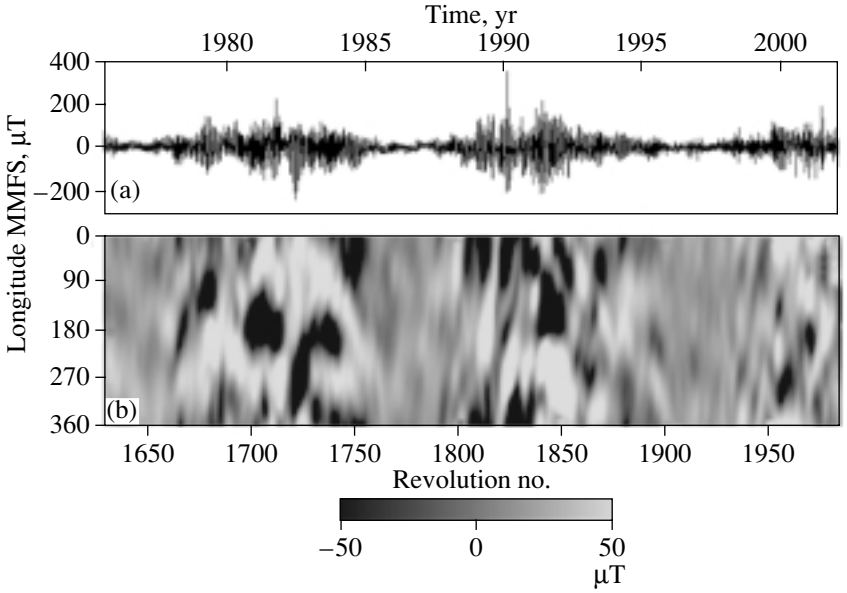

Fig. 3. Plot of (a) the MMFS and (b) a longitude–time diagram for the MMFS.

of 177° and 353°. This dependence is in qualitative agreement with the distribution of the most powerful structures in the pattern of dominant polarities presented in Fig. 2a.

The solid thick curve represents the structure of the large-scale magnetic field in cycle 22. A two-sector behavior dominates here, with the negative and positive polarities centered at longitudes of 37° and 240°. This field structure is in quantitative agreement with the pattern of dominant polarities presented in Fig. 2b. A comparison of the structures of the large-scale magnetic field in cycles 21 and 22 shows that the positions of the main maxima of positive polarity changed only slightly, although these cycles were substantially different.

In this sense, the structure of the large-scale magnetic field in cycle 23 is unexpected. In the first half of the current cycle, the field structure is almost opposite to that in the previous cycle: the negative polarity is centered at longitude 277°, and the positive polarity, at 8°. The longitude dependence in cycle 23 is also in qualitative agreement with the distribution of dominant polarities in Fig. 2c. Despite all the cycle-to-cycle differences in the distribution of the large-scale magnetic field, we can see that the most important extrema for cycles 21–23 correspond to the longitude intervals 10°–40°, 150°–180°, and 240°–280°. The magnetic-field strength in these large-scale structures reaches 20 μT.

According to helioseismological data, the rotational frequency of the solar radiative zone is 433 nHz [27], which corresponds to a sidereal period of revolution of 26.7300 d. To determine if there are stable magnetic structures on the solar surface associated with the rigidly rotating radiative zone, we analyzed a component of the MMFS filtered with a scan time of 28.8406 d, corresponding to the synodic period of revolution of the solar radiative zone. The distribution of the magnetic field as a function of an arbitrary longitude coordinate averaged over 1975–2001 is shown in Fig. 4. A zero value for this longitude corresponds to the beginning of the MMFS time series (May 16, 1975) and rotates with the sidereal period, 26.7300 d. Only the dipolar component of the magnetic field is clearly expressed in the coordinate system rotating with the solar radiative zone, with its intensity not exceeding 8 μT. The complex pattern of the large-scale structures in the Carrington coordinate system is simplified, and a component characterizing the behavior of the magnetic field on long time scales can be revealed. The nature of this stable dipolar component in the overall distribution of the MMFS and other solar magnetic indices seems to be associated with a relic magnetic field, which is frozen in the inner regions of the Sun that are not encompassed by convective motions.

4. INTERPRETATION OF THE RESULTS

Qualitatively, our results can be explained as representing a superposition of the axially symmetric, cyclic dynamo field, the nonaxially symmetric dynamo modes A1 and A2, and a constant relic field. The relic field should display close to S2 symmetry. Recall that, in the classification of types of symmetry of the global field [28], the letters S and A denote symmetric and antisymmetric states about the equatorial plane,

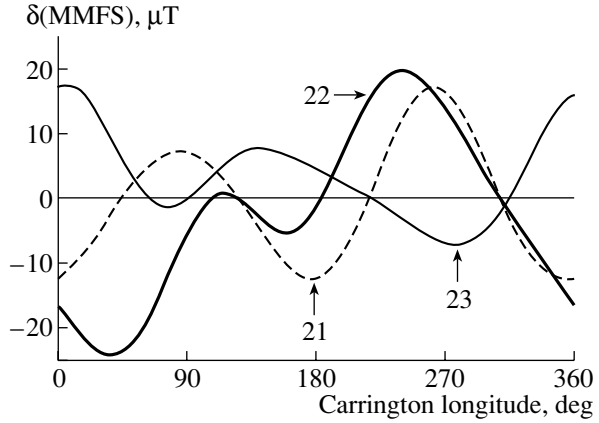

Fig. 4. Cycle-averaged distribution of the magnetic field as a function of Carrington longitude for cycles 21, 22, and 23.

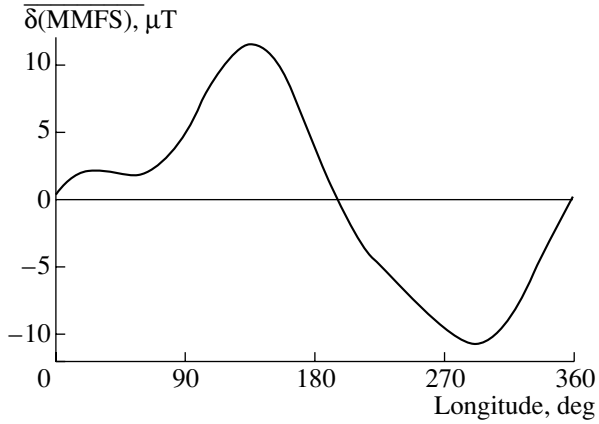

Fig. 5. Average distribution of the magnetic field as a function of an arbitrary longitude coordinate in a system rotating with the period of the solar radiative zone.

respectively, and are followed by the azimuthal wave number. The axially symmetric component of the solar poloidal field is close to A0 [29], with the radial component of the field in one hemisphere usually having opposite signs at low and high latitudes.

The dynamo field A0 and the hypothetical relic field S2 at a given latitude will have the same signs in one hemisphere and opposite signs in the other hemisphere. As a result, the total field will be amplified in one hemisphere and attenuated in the opposite hemisphere. In the next cycle, the dynamo field will reverse its sign, and the region of amplified field will be located in the opposite hemisphere. This is approximately the pattern displayed in Figs. 1a–1c.

However, one weakness of this interpretation is that the calculated relic field [13] displays symmetry type either S1 or A1, not S2. This is probably the result of reducing the data using the period of a Carrington revolution. It would be preferable to investigate the relic field frozen in the radiative zone using the period of revolution of this zone.

5. CONCLUSIONS

We have analyzed the distributions of the dominant polarities of the photospheric and coronal magnetic fields in activity cycles 21, 22, and 23. Stable structures with both dipolar and quadrupolar polarity distributions in longitude were detected in the equatorial regions of the Sun. The polarity distributions usually have opposite signs in the northern and southern hemispheres, which change from cycle to cycle. Despite the alternating polarities in cycles 21–23, the most stable and powerful structures are found at antipodal longitudes.

A wavelet deconvolution was used to study the cycle-averaged distributions of the background magnetic fields and to estimate the intensity of the magnetic field in long-lived structures, which does not exceed 20 μT. A similar analysis of the photospheric magnetic fields in a coordinate system rotating with the radiative zone of the Sun revealed a stable dipolar component with an intensity of 8 μT, which is close to the upper limit for the solar relic magnetic field. Qualitatively, such behavior can be explained as a superposition of the cyclic dynamo field generated in the convection zone and a constant relic magnetic field frozen in the rigidly rotating radiative zone.

Thus, including the relic solar magnetic field in the overall picture of the dynamo mechanism enables us to qualitatively explain the existence of active longitudes and the north–south asymmetry of the corresponding activity. The relic field can affect the convection-zone magnetic fields in two ways. First, the relic field itself produces constant perturbations in the convection zone and influences the distribution of small-scale activity. In addition, it can control the dynamo modes with azimuthal wave numbers 1 and 2, ordering them in longitude. These modes, in turn, affect the distribution of activity in the 11-year cycles. In this way, the relic field can exert a controlling and organizing action on solar magnetic activity on smaller scales. Hierarchical magnetic structures superimposed on the fluctuating magnetic fields in the convection zone are manifest in the patterns displayed by various indices of activity on the solar surface on the corresponding characteristic spatial and temporal scales.

ACKNOWLEDGMENTS

We are grateful to Profs. J.T. Hoeksema and P.H. Scherrer from Stanford Observatory for providing us with the MMFS data and the synoptic

maps of the photospheric and coronal magnetic fields (http://sun.stanford.edu). We are also grateful to D.V. Erofeev for discussions of this study and valuable comments. This work was supported by the Program of State Support for Leading Scientific Schools of the Russian Federation (project NSh-733.2003.2), the Ministry of Industry and Science of the Russian Federation (project 1105), the Russian Foundation for Basic Research (project codes 02-02-16044 and 02-02-39027), and INTAS (grant 2001-0550).

REFERENCES

1. V. N. Obridko and B. D. Shel'ting, Astron. Zh. **77**, 124 (2000) [Astron. Rep. **44**, 103 (2000)].
2. V. N. Obridko and B. D. Shelting, Astron. Zh. **77**, 303 (2000) [Astron. Rep. **44**, 262 (2000)].
3. V. Bumba and R. Howard, Solar Phys. **7**, 28 (1969).
4. Yu. I. Vitinskiĭ, M. Kopetskiĭ, and G. V. Kuklin, *Statistics of Spot-Generating Solar Activity* (Nauka, Moscow, 1986) [in Russian].
5. V. Bumba, A. Garcia, and M. Klvana, Solar Phys. **196**, 403 (2000).
6. A. V. Mordvinov and R. S. Vilson, Pis'ma Astron. Zh. **27**, 528 (2001) [Astron. Lett. **27**, 451 (2001)].
7. L. Jetsu, S. Pohjolainen, J. Pelt, and I. Tuominen, Astron. Astrophys. **318**, 293 (1997).
8. T. G. Cowling, Mon. Not. R. Astron. Soc. **105**, 166 (1945).
9. C. P. Sonett, Nature **306**, 670 (1983).
10. E. H. Levy and D. Boyer, Astrophys. J. **254**, L19 (1982).
11. E. E. Benevolenskaya, J. T. Hoeksema, A. G. Kosovichev, and P. H. Scherrer, Astrophys. J. **517**, 163 (1999).
12. K. Mursula, I. G. Usoskin, G. A. Kovaltsov, in *The Solar Cycle and Terrestrial Climate*, Ed. by A. Wilson (Proc. 1st Solar & Space Weather Euroconference, Spain, 2000), p. 387.
13. L. L. Kitchatinov, Astron. Astrophys. **374**, 250 (2001).
14. M. I. Pudovkin and E. E. Benevolenskaya, Pis'ma Astron. Zh. **8**, 506 (1982) [Sov. Astron. Lett. **8**, 273 (1982)].
15. M. N. Gnevyshev and A. I. Ol', Astron. Zh. **25**, 18 (1948).
16. A. V. Mordvinov and G. V. Kuklin, Solar Phys. **187**, 223 (1999).
17. P. H. Scherrer, J. M. Wilcox, V. A. Kotov, *et al.*, Solar Phys. **52**, 3 (1977).
18. J. T. Hoeksema and P. H. Scherrer, http://sun.stanford.edu.
19. V. I. Makarov, V. V. Makarova, A. G. Tlatov, *et al.*, in *The Solar Cycle and Terrestrial Climate*, Ed. by A. Wilson (Proc. 1st Solar & Space Weather Euroconference, Spain, 2000), p. 367.
20. J. T. Hoeksema, J. M. Wilcox, and P. H. Scherrer, J. Geophys. Res. **88**, 9910 (1983).
21. V. A. Kotov and A. B. Severnyĭ, *The Total Magnetic Field of the Sun as a Star, Catalog 1968–1976*, Ed. by E. E. Dubov (Mezhduved. Geofiz. Komitet AN SSSR, 1983) [in Russian].
22. M. L. Demidov, V. V. Zhigalov, V. S. Peshcherov, and V. M. Grigoryev, Solar Phys. **209**, 217 (2002).
23. A. Ruzmaikin, Solar Phys. **181**, 1 (1998).
24. A. Ruzmaikin, Solar Phys. **192**, 49 (2000).
25. A. V. Mordvinov and L. A. Plyusnina, Solar Phys. **197**, 1 (2000).
26. A. V. Mordvinov and L. A. Plyusnina, Astron. Zh. **78**, 753 (2001) [Astron. Rep. **45**, 652 (2001)].
27. J. Schou, H. M. Antia, S. Basu, *et al.*, Astrophys. J. **505**, 390 (1998).
28. F. Kruse and K. Radler, *Mean Field Magnetohydrodynamics and Dynamo Theory* (Akademie, Berlin, 1988; Mir, Moscow, 1984).
29. J. O. Stenflo, Astrophys. Space Sci. **144**, 321 (1988).

Translated by Yu. Dumin